University of Crete

Department of Materials Science and Technology

Rheology and dynamics of tunable soft materials: from synthetic microgels to biological hydrogels

by

Katerina J. Rementzi

Master's Thesis

Heraklion, 2018

Acknowledgments

In order to complete my scientific adventure in Crete during my master, I had an essential support from several people around me. For this reason I would like to give my special thanks to some of them but since the list is long I will try to be short.

I start with the first person in the list: my biggest support, my mentor, the person who motivated me the most. This is my supervisor and to my eyes the leader Dimitris Vlassopoulos! He gave me the opportunity to work in an awesome environment, to learn and discuss ideas, to meet renowned scientists and to travel around Europe.

The “Swiss support”, my co-supervisor professor Peter Fischer from ETH Zürich for project discussions and the great time in Zürich as well as in Crete.

Lükas Boni, the hagfish collaborator from ETH Zürich was another important person during my second year of my master. His personality and his knowledge gave me another point of you to work with hagfish, “the magic slime”, with much fun!

Daniele Parisi, from IESL-FORTH was my fist collaborator in the first year of my master. His approach and personality was always very positive, friendly and mainly helpful (huge fun in the lab under many aspects)!

The rest of the lab deserves a big thank for their immense help, ideas and support. With no specific order of importance I want to mention: Antonis Mavromanolakis (always available to help and give solutions with an awesome personality), Thanasis (very patient with me for UV-Vis measurements!-always happy to book the instrument and explain sometimes even same stuff) and Panagiota Bogri (always happy to show me again and again the viscometer and other techniques she uses!), Antje Larsen (the light scattering lady in the lab-her expertise with new ideas), Esmaeel Moghimi (the colloidal glass guy, is a rheo-friend, we had many discussion on my PNIPAM microgels), Manos Vereroudakis (his inputs on my data and exchanging ideas was very helpful), Antonio Guiliani (the programming guy in the

lab, Continizer the program I was using the most), Mohan Das (confocal guy, patient to show me imageJ) Dr. Benoit Loppinet (always happy to give inputs, ideas and explanation in his own way), professor George Petekidis (I love his explanations during group meetings and his answers to scientific discussions!).

Many friends and people who were close to me have to be in the list at least for their strong emotional involvement during my path. Their positive character and huge support made me to continue even during very tough times!!

My lovely parents deserve one of the warmest thank…first, my farther who teaches me years now, to be disciplined, to believe in myself and to encounter my life. My mother who shows me how to be responsible, patient and super positive! My brother Dimitris also educates me how to be confident and to have fun with what I do!

Abstract

Hydrogels represent a class of supramolecular networks which are ubiquitous in daily life, with applications ranging from food technology to biology. In this work, we investigated the tunable rheology of two such interacting hydrogels, which constitute the main paradigms of soft matter, colloids and polymers. First, we examined the kinetic arrest of synthetic PNIPAM microgel particles with tunable effective volume fraction by means of altering temperature and/or mass concentration. Reaching the same effective volume fraction reached by increasing concentration or by reducing temperature at lower concentration, we compared the rheology and identified differences between thermal and jammed glass regimes. Second, motivated by the defense mechanism of hagfish against predators, we obtained the main constituent protein, mucin vesicles and explored the properties of the resulting biopolymer network in different pH environments which promote its formation. We focused on the extensional response and dynamic structure in pure water, by adding salts and in artificial seawater, as functions of concentrations. We identified appropriate handling protocols and attempted at linking stiffness with macromolecular structure. Our results provide ingredients for understanding complex mechanisms associated with rheological functions and tailoring the flow properties of such systems toward the eventual molecular design of hydrogels with desired response.

Table of contents

Chapter 1: Introduction

Soft matter continuously attracts a lot of interest by the scientific community due to the ability to tune the properties of raw materials and, consequently, the final products. These materials can be synthetic or biological. Materials with new and unique properties originated from the combination of both polymers and colloids. Synthetic materials such as commercial polymers (i.e., polyethylene, the common commodity of plastic) or colloids (i.e., paints) are readily available and widely used. However, there is constant need to improve their properties and make them more functional, cheaper, ecofriendly etc. On the other hand, biological materials have very complex structures (i.e., DNA or polypeptides). To understand the structure-properties link and design composites, it is important to use of suite of state - of - the art experimental tools.

In the following paragraph, we discuss the classification of soft colloids and their phase transitions.

Classification of soft colloids:

The classification of soft colloids, is briefly discussed in terms of softness, interactions and complexity, as illustrated in figure 1.1 taken from [1].

The flexible linear chain (polymer coil) represents the soft extreme of soft matter whereas the hard particle represents the hard limit (hard sphere-HS). The gap between these limits is spanned by different polymeric-colloidal architectures. Examples include star polymers, micelles and microgels with intermediate softness, as indicated by the double horizontal arrow (soft to hard).

In the top left side of figure 1.1 there is the representation of the interactions which are characterized by a potential U(r) as function of distance r. The soft potential shows that as soon as particles come closer they interact in comparison to hard sphere particles who interact only at distance of 2R (R is the size of the particle), when they touch each other.

The system complexity is shown by the vertical arrows. The complexity is achieved via macromolecular architecture and/or mixing. Hence, chemistry allows the

synthesis of materials which share common features with polymers and/or colloids. This hybrid nature is responsible for a plethora of interesting phenomena and properties, and consequently provides a new route in soft matter research.

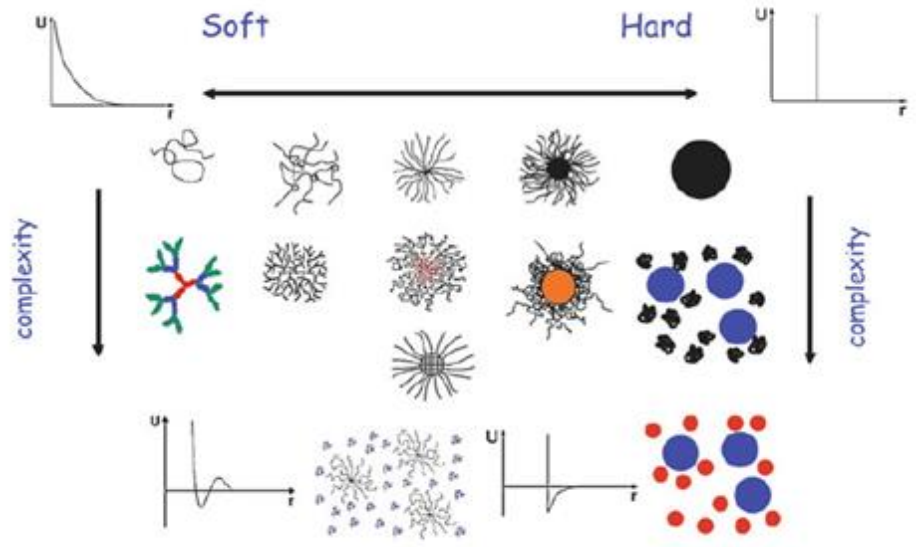

Figure 1.1. Cartoon representation of various systems. The extreme case of soft system is that of a linear flexible polymer coil and the other extreme hard case is that of a hard sphere particle. The horizontal double arrow indicates the direction of soft to hard interactions and vice versa. The vertical arrow illustrates the complexity in the system (addition of particles, polymer chains, grafted chains etc.)[1].

Soft colloids have emerged as an important class of soft materials encompassing properties of polymers and soft colloids. The softness, types of interactions, shape and size along with the internal microstructure are the keys tunability parameters[2]. Popular types in such systems are micelles, star polymers and microgels. Their properties can tune by varying particle elasticity via their microstructure [3], [4], [1].

Synthetic microgels, a prominent paradigm of soft colloids consist of an internal chemical network structure [5]. The softness of such systems can be tuned by the cross-linking density. The higher the cross-linking density the less the softness. These systems are very functional since they can swell in the presence of solvent, depending on temperature and/or pH [6],[7],[8],[9]. Biological systems offer exhibit complex composition and interactions which are not well understood. An emerging class of such systems is that of biological hydrogels, with mucus systems being a notable representative. These are materials with very complicated microstructures

(variable components, some being unknown). An additional difficulty is the presence of charged groups up to the biopolymeric chain, hence polyelectrolyte with unknown charge distribution. However, the conformation can be tuned by adding salt. In the next paragraph, we discuss the fundamental idea of mucus hydrogels.

Mucus hydrogels:

Mucus consists of a gel matrix of water (95%), high molecular weight mucin like glycoproteins (3%) and other small molecules (2%). There are many different kind of mucus and there is a classification depending on their origin (i.e. gastric, duodenal, colon mucus etc.)[10]. The mucin concentration, the functionality (possible additional interactions or degradation) and the way of acting at different environments (saline or not) vary with the protein origin.

A main use of such systems is to protect the epithelial tissues or as a defense mechanism for the animals. A unique example is the hagfish which is an eel-like fish and lives in the ocean. It is one of these animals where protect itself due to the slime formation with a specific mechanism. This special and defensive slime is one of the most excited situations in nature since it is formed in few milliseconds after the fish is attached from the predator. It entraps vast amount of water (99.996%), is very cohesive, super dilute, tough and elastic. It is consisted by two components: i) the skeins and the ii) mucin vesicles. The first in seawater undergoes unravelling and the later swelling and consequently mucin release[11]–[13]. The interplay between these two components is not well known. For this reason, isolated mucin vesicles investigated separately from the skeins in order to understand better the role of these proteins in the whole slime.

Open challenges:

This thesis is divided into two parts. A detailed investigation of suspensions of poly-N-isopropyl acrylamide (PNIPAM) thermosensitive microgels in nanopure water is the content of the first part (i). Samples were used from the dilute to dense regime in order to reach the repulsive glassy regime and further on jamming regime. In the second part (ii) we focus on mucus hydrogels with the goal to better understand their viscoelastic behavior (shear and extensional rheology) in relation to their dynamic structure(dynamic light scattering).

i) Synthetic thermosensitive microgels

PNIPAM microgels have been studied extensively during past decades by using various techniques. It is one of the most popular materials because of its thermoresponsive character and super absorbance profile. PNIPAM microgels entrap water at low temperatures and this causes a strong effect on their hydrodynamic size[6]. Based on this a pertinent question is whether one can reach the same rheological properties by using different paths to reach the same volume fraction.

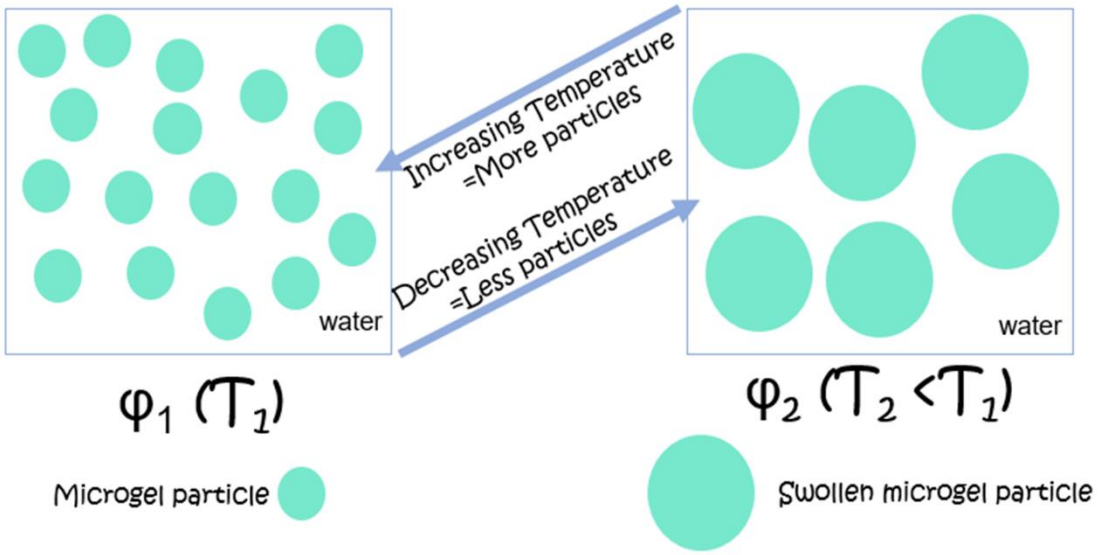

Figure 1.2. Cartoon representation of PNIPAM microgels in water at two different temperatures T_1 and T_2 at the same volume fraction φ reached by two different ways (once by increasing concentration and once by varying temperature).

In figure 1.2 above we show a simplistic cartoon which explains the motivation. We can reach the same volume fraction φ with two different paths: i) either by increasing the number of particles (mass concentration increases at a constant temperature-left box of figure 1.2) ii) or by decreasing the number of the particles (temperature decreases at a constant concentration-right box of figure 1.2).

The effective volume fraction estimated as φ_{eff} =c/c*, the ratio of the mass concentration to the overlap concentration (estimated from hydrodynamic size, R_H) [1]. More details about that calculations are given in chapter 5 where we do report

our results. In appendix I there is a discussion on the estimation of the volume fraction.

i) Biological hydrogels

Mucus systems are composed mainly of water (>90%) and are found in mammalians and non-mammalians organisms. Here, we discuss the latter and we focus on mucin-like glycoproteins which is the major component of mucus. Mucins are long biopolymers with ionizable groups (mucus: polyelectrolyte system), with undefined structure. In figure 1.3 below we show a typical simplified mucin molecule.

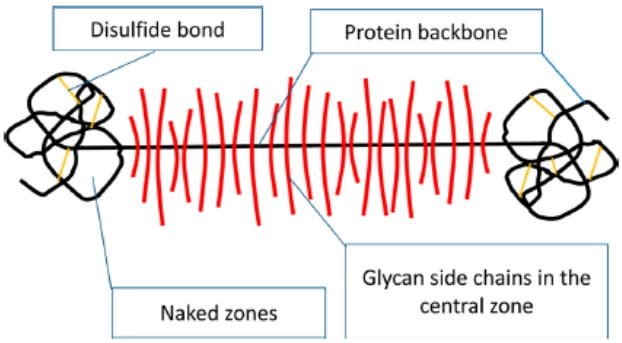

Figure 1.3. Cartoon representation of a mucin molecule, figure taken from [14].

The motivation was to characterize the hagfish mucus by dynamic light scattering in order to understand the diffusion dynamics. On the other hand, mucus is one of the softest elastic biomaterials [13], [15] with new emerging applications. For this reason, mechanical properties were tested under extension and shear, and a link to diffusion dynamics was attempted.

The system is very complex due to the presence of various uncontrollable and/or unknown parameters. Below, we list the main questions to be addressed:

1) How does hagfish slime manage to be very dilute but still a functional hydrogel?
2) How does hagfish slime and in particular the mucin - being a polyelectrolyte system - interact with its high ionic strength environment?
3) Can we compare the microscopic properties (probed by dynamic light scattering) with the macroscopic properties (probed by rheology in extension and shear) at the same conditions (e.g. at a given concentration)?

Thesis outline:

The outline of this thesis starts with chapter 2 which is a background on soft systems (synthetic and biological), include polyelectrolyte, we discuss some open questions from previews work. In chapter 3, we focus our attention on the experimental techniques used: DLS, SLS, rheology, CABER, UV-vis. Chapter 4 focused on the materials used, i.e., colloidal thermoresponsive PNIPAM microgels in water and polymeric biological glycoproteins. We discuss the sample preparation for the two systems and their characterization. Chapter 5 is dedicated to soft microgels; how we understand the glass and the jamming transition. Chapter 6 and 7 present the structure and the rheology of hagfish mucin proteins in different environments. We summarize the thesis with chapter 8. The conclusions concerning the two systems and we combine our work in progress with open question as perspectives. The last part of the thesis contains an appendix with some additional results.

Chapter 2: Background

This chapter focuses on the brief background of microgels as well as the mucus hydrogels.

2.1. Microgels

Microgels are cross-linked spherical particles with an intermediate, yet tunable softness. Their internal structure is similar to that of a typical polymeric network. The key feature is their ability to undergo a change volume in the presence of an external stimulus. The swollen/shrinkage situation is triggered by pH, temperature and solvent quality. There is a lot of literature on microgels which addresses their fundamental features [16]–[20].

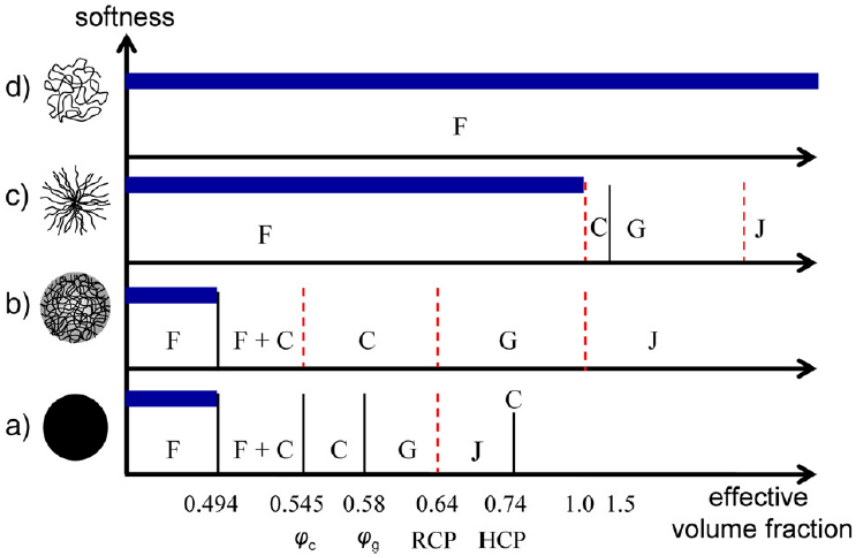

Figure 2.1. One-dimensional state diagram of monodisperse athermal soft colloids against their effective volume fraction. The vertical axis represents the softness from hard sphere limit (a) to the soft polymer coil (d). The horizontal axis represents the effective volume fraction. The black lines shows the well-known volume fractions and the red dashed lines are not yet well established. Different letter correspond to different phases: F is fluid, F+C is the coexistence of fluid and crystal phase, C is crystal, G is glass and J is jamming. Figure taken from [16].

In figure 2.1, we see that hard spheres (a) exhibit similar transitions with microgels (b). The crystal, glass and jammed state of microgels occur at larger range volume fraction regions in comparison to HS. This reflects the deformability of soft particles.

For example, the first region is that of the fluid which covers the same range of volume fraction for both microgels and HS, the second region is the coexistence of fluid and crystal, then the system yields to crystal, to glass (random close packing-RCP) and finally to a jammed state (HCP). The black solid lines are the well-established volume fractions and the red dashed lines the non-universal volume fraction transitions. Cases (c) and (d) are not discussed here.

The systematic work of Pellet and Cloitre [21] on polyelectrolyte microgels presents a protocol to define the glass and the jamming transition. It is marked by a difference in the scaling of plateau modulus with concentration, becoming linear in the jamming regime, figure 2.2.

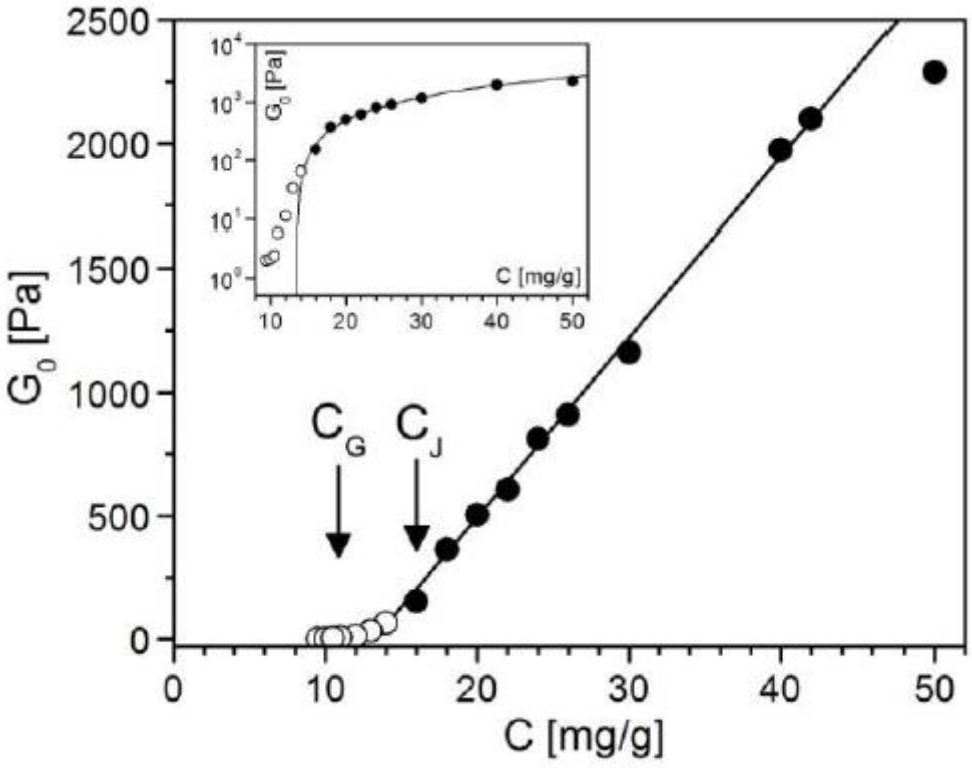

Figure 2.2. Plateau modulus against polymer concentration. The empty symbols correspond to the entropic glassy regime whereas the full symbols correspond to the jammed glass. The two vertical arrows indicate the concentrations of the glass and jamming transition consequently. The inset represents the same results in a different representation which is the lin-log form. The black line is the linear fit of the data. Figure taken from [21].

2.1.1. Glass and jamming transition

In this paragraph we note the hallmarks of the glass and jammed state. The former is characterized by caged dynamics (kinetically arrest situation) where particles are trapped in virtual cage. This occurs beyond a volume fraction of 0.58 and we call it thermal glass. For hard spheres this regime extends up to the randomly closed packed (RCP) state [22], [23]. The same holds for microgels with the only difference that particles are able to be deformed.

The jammed glass state is a very dense regime where the suspension is “frozen” (particles do not move). For hard spheres this situation represents the maximum packing fraction whereas for microgels this maximum packing fraction is also controlled by osmotic pressure. The osmotic pressure induces compression of the particles, their shape changes and the jamming transition shifts to the right in the state diagram (figure 2.1).

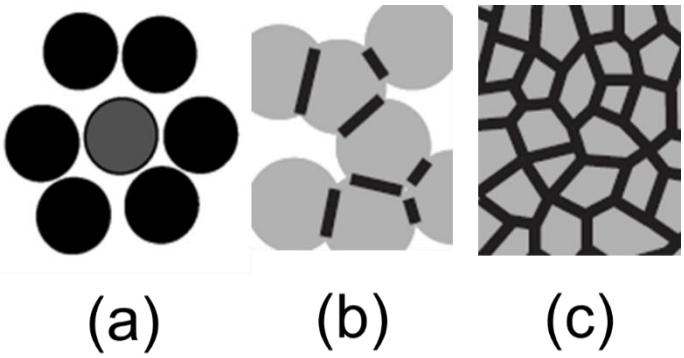

Figure 2.3. Cartoon representation of different phases above crystal phase; (a) glassy regime; (b) particles create contacts; (c) jamming regime. Figure taken from [24], [25].

In figure 2.3 above we illustrate the three distinct regions of colloidal particles. In case (a) particle is trapped in a virtual cage (grey particle) and the neighbors have a random position. This regime is the so-called thermal glass [24]. In case (b) soft particles start to create contacts once the volume fraction increases and the empty space around is less. In case (c), soft particles strongly deformed and we are deeply in the jamming regime or jammed glass [25].

2.1.2. Lower critical solution temperature (LCST) transition

The specific volume of microgels as already referred above alter size with external stimulus such as pH, temperature or electric field. Here, we focus on the effect of temperature. There are two types of temperature transitions depending of the nature of the system: i) the upper critical solution temperature (UCST) and ii) the lower solution temperature (LCST). Critical temperatures are connected to the solubility of a polymer in the solvent. Upon heating, an aqueous PNIPAM solutions becomes a two phase system [26]–[28]. This is also discussed in paragraph 5.1 where we show experimental results.

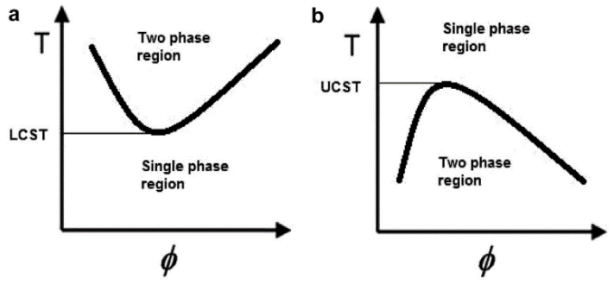

Figure 2.4. Phase diagrams of polymers as concentration and volume fraction increases. Graph (a) polymers with LCST and graph (b) polymers with UCST [26].

2.2. Polyelectrolytes

This is a huge and complex class of polymers and here we give a very brief overview in order to summarize the most important points. Figure 2.5 represents the three universal classes of polymers in dilute solutions: poor solvent conditions (chain shrinkage), θ-solvent (ideal conditions), good solvent (swollen chain) and charged polymer (polyelectrolyte) in extended configuration [29]. We focus on the latter case and below we list key features.

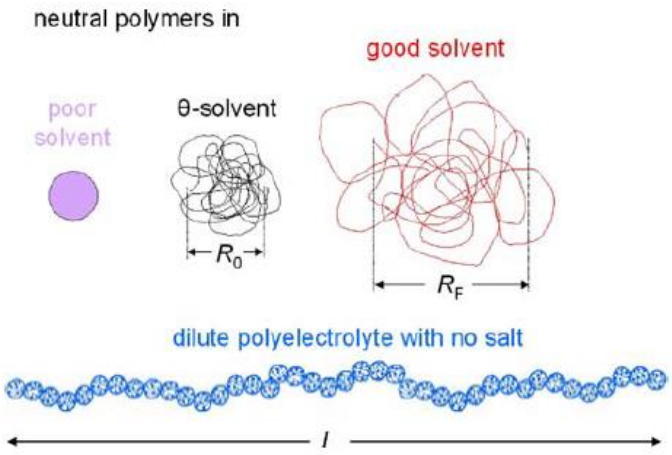

Figure 2.5. Universal classes of polymers in dilute conditions. From left to the right: polymer in a poor solvent (purple) with size $R \sim bN^{1/3}$, polymer in θ-solvent (black) with $R \sim bN^{1/2}$ and last polymer in a good solvent (red) with $R \sim bN^{5/3}$. In the bottom we have the polyelectrolyte chain in its extended configuration in salt-free environment with L to be the length of the chains, L~N. Figure taken from [29].

Polyelectrolytes (PEs) are polymers with ionizable groups. When exposed in a polar solvent, they dissolve and the dissociation of the ionic groups yields charged macroions and small counterions. The degree of dissociation depends on external stimulus like the pH of the solution, the temperature and the ionic strength. PEs are ubiquitous in nature (DNA, proteins) but also there are synthetic PEs such as for example the poly (styrene sulfonate). In the figure 2.6 we show a biological example (RNA molecule) with the different contributions (e.g. charges, counterions, hydrogen bonds etc.) in aqueous solution [30].

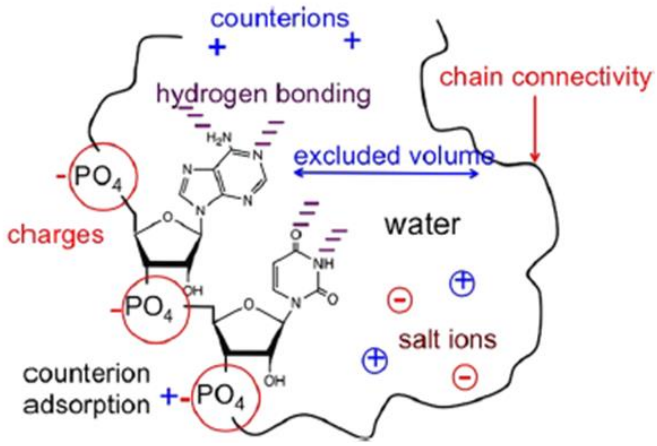

Figure 2.6. Example of a natural polyelectrolyte, RNA. All written quantities: counterions, hydrogen bonding, chain connectivity, salt ions and the charged groups on the polymer chain contribute to the final structure and properties of the polyelectrolyte solution. Figure taken from [30].

Despite numerous advances in theoretical understanding, the structure and dynamics of PEs are not fully understood. Their complexity is mainly due to the presence of electrostatic interactions. It is important to notice that there are two main categories of polyelectrolytes, besides natural and synthetic, that of weak and strong PEs:

Weak: they are similar to that of neutral polymers because their charge density is small and consequently, so is their dissociation.

Strong: in this case the charged groups contribute to a large extend on dynamic properties since the structure and the interactions controlled by the strong electrostatic coupling.

Hydrophobic interactions and hydrogen bonding play major role in the PE conformation. However, their dynamics depends on many factors. They include the mechanical properties though rheology (e.g. viscosity, relaxation time and modulus) which depends on structural details as probed by X-ray, neutron scattering, light scattering (e.g. diffusion, structure and conformation).

The properties of PEs are also reflected in the concentration range with respect to topological interactions (e.g. determination of semidilute, c*, and entanglement concentration, c_e). Neutral polymers exhibit very different scaling laws in comparison to charged systems. A summary of concentration dependence of the main static and dynamic properties is shown in table 2.1., taken from [29]. In the next paragraph 2.2.1., we discuss only the latter case that of the diffusion coefficient on PEs.

Table 2.1. Summary table of scaling predictions for neutral (ideal and good solvent conditions) and charged polymers. De Gennes and Rouse predictions are about solution structure and terminal polymer dynamics in the semidilute unentangled solutions. Table taken from [29].

	General equation	Neutral in θ-solvent	Neutral in good solvent	Polyelectrolyte with no salt
Scaling exponent	$\upsilon \equiv \partial(\log R_{\text{dilute}})/\partial(\log N)$	$\upsilon = 1/2$	$\upsilon = 0.588$	$\upsilon = 1$
Correlation blob size	$\xi \sim N^0 c^{-\upsilon/(3\upsilon-1)}$	$\xi \sim N^0 c^{-1}$	$\xi \sim N^0 c^{-0.76}$	$\xi \sim N^0 c^{-1/2}$
Polymer size	$R \sim N^{1/2} c^{-(\upsilon-1/2)/(3\upsilon-1)}$	$R \sim N^{1/2} c^0$	$R \sim N^{1/2} c^{-0.12}$	$R \sim N^{1/2} c^{-1/4}$
Chain relaxation time	$\tau_{\text{chain}} \sim N^2 c^{(2-3\upsilon)/(3\upsilon-1)}$	$\tau_{\text{chain}} \sim N^2 c$	$\tau_{\text{chain}} \sim N^2 c^{0.31}$	$\tau_{\text{chain}} \sim N^2 c^{-1/2}$
Terminal modulus	$G = N^{-1} c_n kT$	$G = N^{-1} c_n kT$	$G = N^{-1} c_n kT$	$G = N^{-1} c_n kT$
Polymer contribution to viscosity	$\eta - \eta_s \approx G\tau_{\text{chain}} \sim Nc^{1/(3\upsilon-1)}$	$\eta - \eta_s \sim Nc^2$	$\eta - \eta_s \sim Nc^{1.3}$	$\eta - \eta_s \sim Nc^{1/2}$
Diffusion coefficient	$D \approx R^2/\tau_{\text{chain}} \sim N^{-1} c^{-(1-\upsilon)/(3\upsilon-1)}$	$D \sim N^{-1} c^{-1}$	$D \sim N^{-1} c^{-0.54}$	$D \sim N^{-1} c^0$

In this work: we deal with strong polyelectrolytes and their diffusion. Mucins included in the category of proteins and especially to glycoproteins. This type of proteins have

dense charges of sulfonate groups (SO^{3-}) and carbohydrates. These two characteristics make them strong PEs. Mucin-like glycoproteins discussed in detail on materials, in paragraph 4.2.2.

2.2.1. Diffusion dynamics

PEs are characterized by a big variety of length scales (monomer, Kuhn length, chain length etc.) one of the most important being the correlation length, ξ. This average mesh size shown in figure 2.7 and 2.8 as the distance between the two charged chains. However, inside this blob ξ, there is another blob, called electrostatic blob where the chain behaves ideally. In polyelectrolyte solutions the screening of the interactions is discussed in terms of the mean field of Debye-Hückel theory. The size ξ is the so-called Debye electrostatic screening length. The interactions are screened at length scales larger than $\xi=r_D$ where r_D is the Debye screening length. The Debye screening length is the corresponding length scale in which the chains feels an extra charge in the system and is given by the following formula[31]:

$$r_D = \left(4\pi l_B \sum_i c_i z_i^2\right)^{1/2} \qquad \text{Eq. 2.1}$$

Where l_B is the Bjerrum length, c_i is the number density of ions and z_i is the carrying charge of the ion.

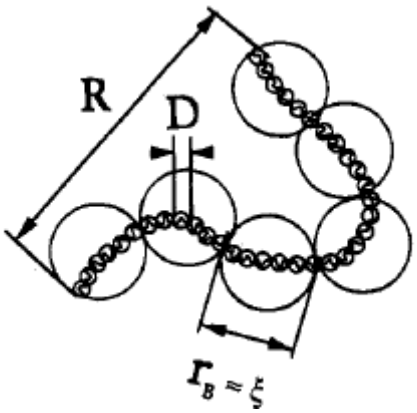

Figure 2.7.Cartoon illustration of a polyelectrolyte chain in the semidilute regime in a salt free environment. The chain constituted from electrostatic blobs in an extended configuration. Figure taken from [31].

One of our goals is to determine an overlap concentration for mucins, in order to define the point beyond which mucins start to interact topologically. We show next what it is already established for other PE systems. In figure 2.8., we depict a synthetic polymer, poly (styrene sulfonate) in terms of its diffusion behavior at different molecular weights. In comparison to neutral polymers, the unentangled semidilute regime in salt-free conditions covers many decades. This is due to the topological constrains between the chains (e.g. charge repulsion). To this end, the dilute and the semidilute regime are concentration independent, $D \sim c^0$. When data start to deviate from the linearity, $D \sim c^{-1/2}$ entanglement region is reached.

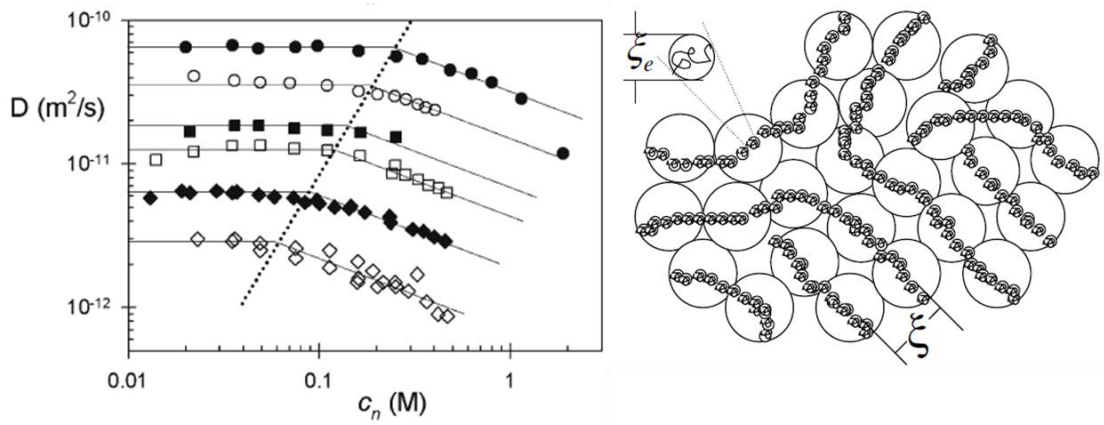

Figure 2.8. Diffusion coefficient against number density of monomer for poly (styrene sulfonate) in water for different molecular weights. From top to the bottom the molecular weight increases. Slopes: $D \sim c^0$ and $D \sim c^{-1/2}$. The cartoon illustrates polyelectrolyte chains in the semidilute regime, ξ is the correlation length. Both figures taken from [29].

The same observation has been made by Sedlák and Amis [32]. We denote this diffusion coefficient as fast diffusion because of the presence of a slow mode is a PE effect. This slow mode is a consequence of the large multichain domains in solution. A complete theoretical understanding of this behavior is lacking [32], [33].

Here we wish to highlight that hagfish mucins investigated via dynamic light scattering shows both the independence of diffusion on concentration in the semidilute unentangled region and the slow dynamics. Results discussed in chapter 6.

2.3. Hydrogels

Hydrogels represent an important class of soft materials as macromolecular polymers in the form of a three dimensional (3D) network which immersed in water. They have enjoyed significant research interest over the past decades due to their sensitivity on external stimulus. Flexible, linear, neutral polymers can be converted into crosslinked hydrogel networks by using chemical agents (synthetic hydrogels). PEs can form physical or chemical networks in water due to the swelling of the charged chains (retain water) [34].

In the case of physical networks (e.g. biological systems) the gel is solvated in water (e.g. hydrophilic proteins). The biocompatibility of microgels is very challenging for applications. For instance, medicines based on biopolymers (tissue engineering), biosensors, food industry and water purification are some common examples for the use of such structures [34]. Physical gels may not remain stable and intact for long time, whereas synthetic gels remain stable even over years.

2.3.1. Mucus systems

Mucus is a thick substance with interesting viscoelastic properties provided by the structure formed from biopolymers. The main components of mucus are water (>95%), mucin glycoproteins (3%), lipids, ions, cells and cellular debris (1-2%); other molecules [35]. There are two main actions of mucus in general: i) to wet epithelial surfaces in the body (organs) and ii) to provide a defense mechanism in most animals. We provide some examples below:

i) In our body, we have plenty of mucus in different organs with different roles. One of its purpose is to give a barrier against bacteria, toxins and pathogens (e.g. lungs and respiratory). Additionally, it protects the epithelial lining (e.g. the stomach against the acidic gastric juice). It also provides lubrication and hydration (e.g. thin film in the eye). A thorough review on mucus systems presented in humans provided by Demouveaux [10].

ii) In nature, there are animals which secrete mucus as a defense mechanism. Characteristic example is the Atlantic hagfish *(Myxine glutinosa)* which produces a vast amount of slime (with mucus to be the

main component-discuss in paragraph 2.3.2) within milliseconds [11]. Another example is the freshwater fish *(Misgurnus anguillicaudatus)* which has a loach skin mucus. Its main functionality is to maintain clean and lubricate its skin even if it goes to the sludge[36].

All mucus systems are characterized by very rich viscoelastic properties originated from the presence of mucins. Here, we present typical rheological data for mucus of various origins: gastropod pedal mucus [37], porcine gastric mucin [38]–[40] and mammalian lung mucus [41]. The pioneering work of Phillipe et al. [14] discusses the structure of pig gastric mucin proteins and the corresponding aging profile[14].

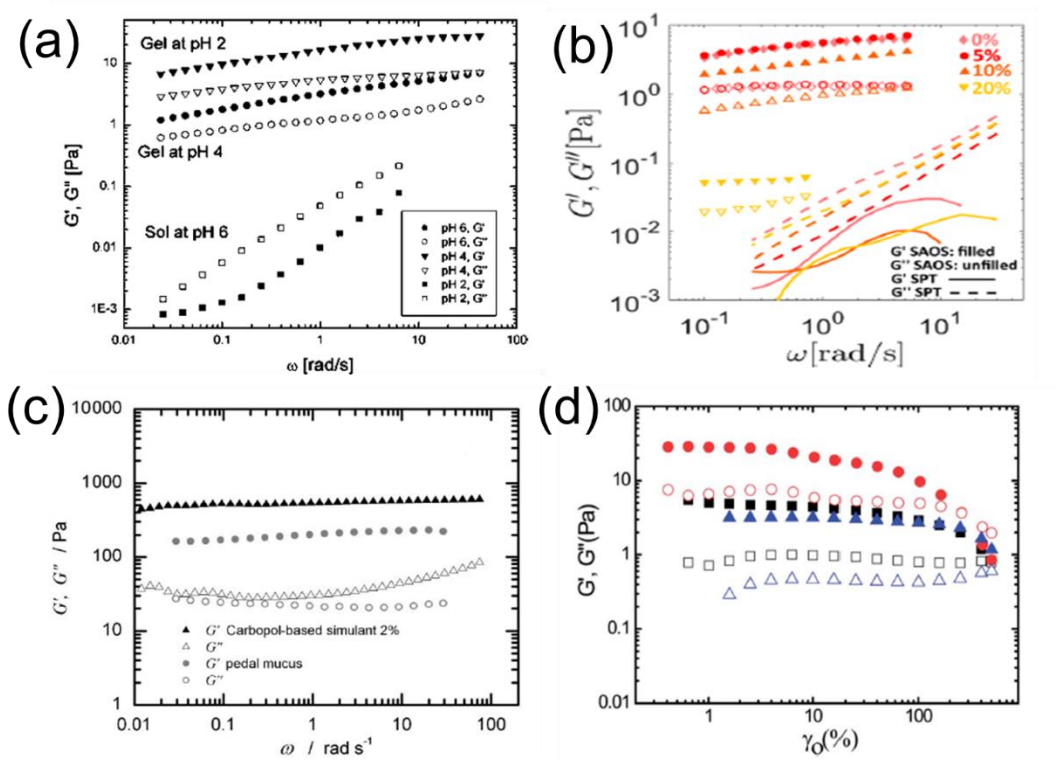

Figure 2.9. Collection of rheological data for different mucus systems. Dynamic frequency sweep in the linear regime: (a) pig gastric mucus at different pH (with pH=4 being the natural environment)[38]; (b) simulation (MSD) and experiments on pig gastric mucus at pH=2 and c=10mg/ml at different concentrations of hexanediol (surfactant)-different symbols[39]; (c) native pedal mucus in comparison to carbopol[37]. Dynamic strain sweep: (d) mammalian (horse) lung mucus at different frequencies[41].

We can observe in figure 2.9 that all mucus systems exhibit similar rheological behavior. In particular, G' exhibits a plateau in the range 0.1<G'<100 Pa [35]. The fact that G'>G'' is of course expected for viscoelastic solid-like gels. The soft elastic

nature of mucus is attributed to the unique and useful functionalities within different organs. In figure 2.9a, b it is shown how the pH and the surfactant can affect the functionality of gastric mucus in respect to its natural stomach environment. In figure 2.9c the pedal mucus viscoelastic behavior is mimicking the mechanism of the adhesive locomotion of gastropods. In the last figure of 2.9d it is shown how the linear and the nonlinear behavior of lung mammalian mucus affected from different strain deformations.

Another important fingerprint of mucus (pig gastric) is depicted in figure 2.10 below, where the effects of waiting time are investigated. Aging leads to a decrease in moduli as the waiting time increases. This weakening is likely due to the onset of gel fluctuations at large scales and to the locally compact configuration[14].

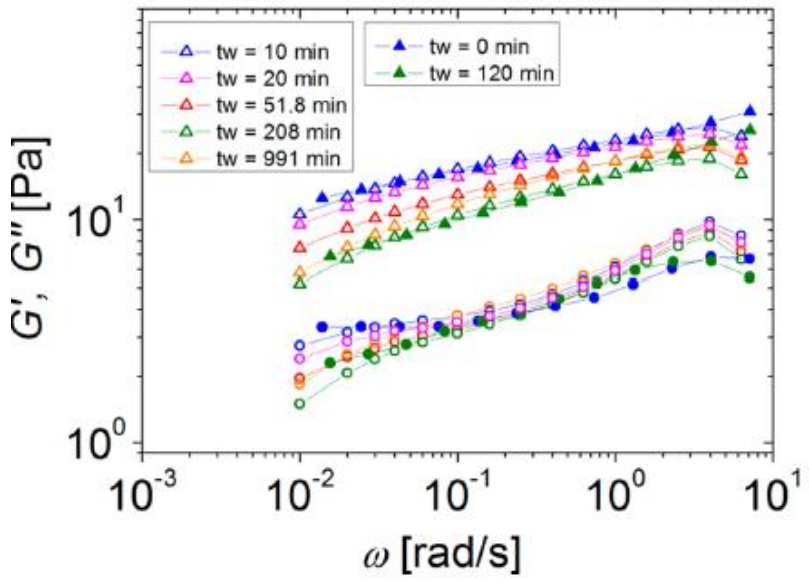

Figure 2.10. Dynamic frequency sweep test for different sample ages. Empty symbols: triangles=G' and circles=G'' from multiwave tests and full symbols from data conversion of the stress relaxation experiments. Figure taken from [14].

2.3.2. Hagfish mucus

Hagfish slime is the product of their (hagfishes) defense mechanism. Despite the fact that there are various types of hagfishes all appear with the same functionality and role. Here, we investigate the Atlantic hagfish *(Myxine glutinosa)*. Focusing on the work of Fudge et. al [13], we start the discussion with the following sentence: *"Hagfish slime is 1000 x more dilute than other mucus secretions".* By observing the first and the second column on table 2.2 we can notice that hagfish slime has the

lowest mucin composition (c=0.02mg/ml). As already referred to, mucin is highly viscoelastic (forms the hydrogel) due to disulfide bonding. Mucins have the ability to create the network (vast amount) within few milliseconds.

Table 2.2. Concentration of mucins for various origin secretion, table taken from [13].

Source	[Mucin] (mg ml^{-1})	Reference
Hagfish slime	0.02	This study
Gastric mucus	47	Sellers and Allen, 1989
Duodenal mucus	38	Sellers and Allen, 1989
Colon mucus	20	Sellers and Allen, 1989
Slug pedal mucus	1–32	Denny, 1979
Human salivary mucus	14	Veerman et al., 1989
Human gastric mucus	30	Pain, 1980

Hagfish, after the attack from a bigger fish (e.g., shark) and because of fear, produces an exudate (white liquid in its ventrolateral place, figure 2.11b) [11], [13], [42]. The exudate has two components: i) skeins and ii) vesicles. Skeins are very long proteins (1-30cm) which are coiled-up, while vesicles (1-3μm) have a lipid bilayer which keeps the mucins packed. When the exudate is in contact with seawater (effect of ions in the structure and final properties [12], [43]) skein unravels in very precise way and vesicles swell and release the mucin-like glycoproteins.

Both components act synergistically and form the slime. Skein provides the cohesiveness in the system and mucins the elastic soft nature. The gelation is a natural “magic” fast process within ~400ms. The network expands 10000 times its initial volume [13], [44]. In figure 2.11 below, taken from [11], we illustrate the mechanism discussed for slime formation. More details and the exact mechanism are discussed extensively in chapter 4.

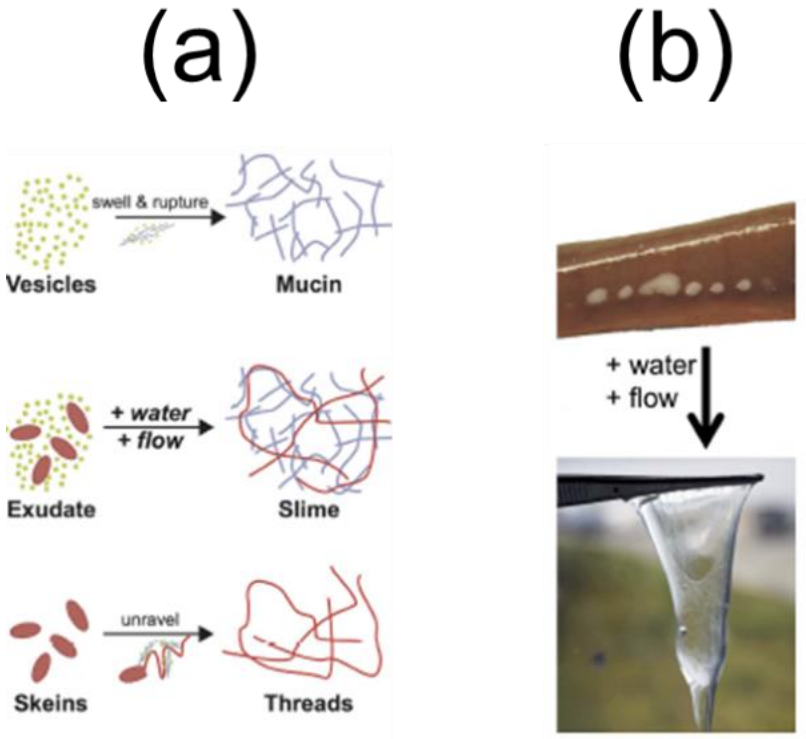

Figure 2.11. Cartoon representation of hagfish slime formation on the left and real slime from hagfish exudate on the right. (a) The two components vesicles and skein included in the exudate (white dots) and in contact with water release their proteins (mucins and threads respectively); (b) Shortcut of the fish with the exudate upon contact with water and the formation of hagfish slime. Figure taken from [11].

The main motivation for the present work relates to the question: How does hagfish slime manage to be very dilute but still a functional hydrogel? The term “very dilute” is due to the vast amount of water trapped into the network (99,996%) and the term “functional” is referred to the strong ability to provide a proper defense mechanism.

2.4. Open questions concerning hagfish mucus

There are three main topics of interest: i) the structure of mucins; the viscoelasticity i) under shear and iii) under extension.

2.4.1. Mucins structure

The structure of hagfish mucins investigated via light scattering and the size can be determined. However, the molecular weight and the interactions range of such

mucins remain unresolved. The persistence length and the exact shape of mucins is also not unambiguously determined. For example:

-How can we determine the molecular weight of mucins via light scattering or other techniques? Can we use static light scattering and through the second virial coefficient and refractive index increment estimate a value? If we do so, could we compare with another technique and with other mucins originated from other organisms?

-How can the structure be qualified besides image microscopy? Light scattering is used in the present work but is not able to detect very small and very large length scales. Small angle light scattering and X-rays are two most common techniques available to collect information for small length scales, i.e. its internal structure (SAXS). However, estimation of the persistence length of the polyelectrolyte chain remains a challenge.

2.4.2. Shear rheology

The shear rheology performed mainly in the linear regime and modulus was defined at 20^{o}C. Some additional tests, were performed at 5^{o}C but was not further discussed and analyzed in depth. The understanding of the interactions and the polymer conformation are of great scientific interest in such natural temperatures at 5^{o}C. For example: How is the mucin structure influenced at 20^{o}C in comparison to its physical environment at 5^{o}C in the cold seawater? On the other hand, measurements done in the linear viscoelastic regime and the pertinent question is how do large shear deformations (e.g. large amplitude oscillatory shear, LAOS) break and/or reform (or not) the mucin network. Nonlinear rheology has been performed by Ewold and co-workers in the whole hagfish slime [45] and in order to mimic the adhesive locomotion of gastropods [37].

Finally, artificial seawater conditions were tested under shear and electrostatic screening is pronounced (chapter 7). However, the effect of each salt separately was not investigated. Hence, we do not know how the monovalent and the divalent ions contribute to mucus viscoelasticity. We also wish to understand whether the divalent ion of Ca^{2+} at different concentrations provides internal bridges on the network [12] and what is the special role of Ca^{2+} in comparison to Mg^{2+}[43].

2.4.3. Extensional rheology

Extensional rheological measurements have been performed at different concentrations of mucins and at different saline environments at room temperature. The sample preparation under shear and under extension differs. For this reason, is crucial to understand how the dialyzed mucus (measured in shear) behaves under elongation. The opposite cannot be done (non-dialyzed in shear) since the signal is too weak to be detected by the rheometer. Here, we wish to understand how the stretching profile on dialyzed mucus is and compare/correlate results from extensional and shear rheology?

Chapter 3: Methods

In this chapter we discuss the experimental techniques and methodologies used in the present thesis. We introduce the basic theoretical background behind of these techniques. Details about sample preparation, measurement protocols and experimental setups are discussed. The main techniques used are dynamic and static light scattering (DLS and SLS), shear and extensional rheology. Additional techniques have been utilized for material characterization, such as the turbidimetric analysis (UV-VIS).

3.1. Dynamic and Static light scattering

Dynamic and static light scattering provide important information pertinent to the system's characterization. In the case of a single particle, the total field E is the superposition of the scattered fields from all particles (e.g. N particles) in the scattering volume tested in light scattering[46]. Figure 3.1 depicts the electromagnetic wave propagation in space and time, where E is the strength of the electric field, E_o is the amplitude of the electric field, λ is the wavelength of the incident light and c is the speed of light ($c=3*10^8$ m/s).

$$E(t) = \sum_{i=1}^{N} E_o \exp[i\vec{q}\vec{r_i}(t)] \qquad \text{Eq.3.1}$$

where E_o is the scattered field at the detector from a single particle in the field, $\vec{q}$ is the scattering wavevector ($\vec{q} = \overrightarrow{k_s} - \overrightarrow{k_o}$) with $\overrightarrow{k_o}$ the incident wavevector and $\overrightarrow{k_s}$ the one detected in the far field, $\vec{r_i}(t)$ is the position of the i^{th} particle.

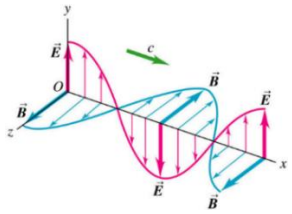

Figure 3.1. Electromagnetic wave propagation in space and time (vertical we note the electric strength field-pink and horizontal is the magnetic strength field-blue), the green vector indicates the velocity and the direction of both propagated waves.

3.1.1. Dynamic light scattering (DLS)

DLS is a powerful tool for probing spatio-temporal correlations and is used widely in soft condensed matter. We focus here on quasi-elastic light scattering (QELS), also known as photon correlation spectroscopy (PCS). The former name reflects the mobility of the particles which scatter the light and the process is quasi-elastic and the latter is the one used the most historically. There are comprehensive and new reviews on the tale of light scattering pioneers by J. Stetefeld and K. Fischer [47]–[49]. The main principle of the technique is illustrated in the following picture which is a cartoon representation of the experimental setup. The instrument used is ALV-5000 (from ALV, Germany). There is a polarized monochromatic laser beam at a wavelength of λ=532nm passing through an optical train, mainly lens and polarizers. The vertically polarized light goes through the measured solution. The sample's temperature is controlled by means of a recirculating fluid bath (blue-red) (temperature ranges from 15ºC to 50ºC). The solution scatters since there are particles (scatterers) fluctuating over time due to Brownian motion. The photomultiplier records the fluctuations of the scattered light at a given angle which defines the scattering wave vector q, with lens and pinhole setup to ensure a well-defined q and an effective collection of scattered light. The scattering of the light arrives to the detector which is adapted to a goniometer. The variation of different angles (ranging from 25º to 150º) allows us to have access at different length scales. Finally, the correlator transforms the recorded signal of the scattering intensity fluctuations of the solution into a digital signal, which is then auto-correlated for dynamic light scattering measurements (correlation function).

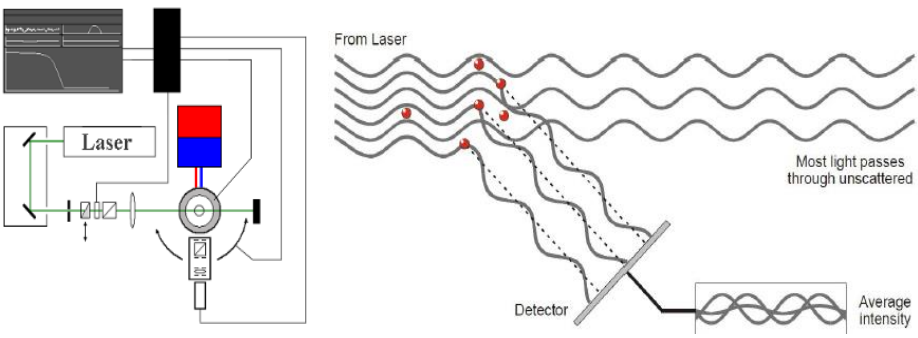

Figure 3.2. Cartoon representation of the experimental setup (ALV-5000) of the light scattering technique (left). A monochromatic laser light with a wavelength of 532nm passes through an optical train with lens and polarizers and it arrives to the solutions which scatters. The solution is connected to the bath for temperature control and there is a detector which is adapter to a goniometer in order to collect the intensity fluctuations over time at different length scales (q-variation). The signal arrives to a correlator card which shows the final correlation function. In the plot on the right there is the zoom in on a laser beam which arrives to the scattered particles, their signals is the intensity of the scattered light and they averaged in the detector (right) [47].

In figure 3.2 (top right) a schematic illustration of the laser light wave passing through the sample and scattered is shown. The detector collects all these signals and does the average which is our final intensity fluctuations plot over time. Figure 3.3 below depicts the different ways by which small and large particles scatter. The higher the size the slower the diffusion in the medium (slower intensity fluctuations) and vice versa (faster intensity fluctuations).

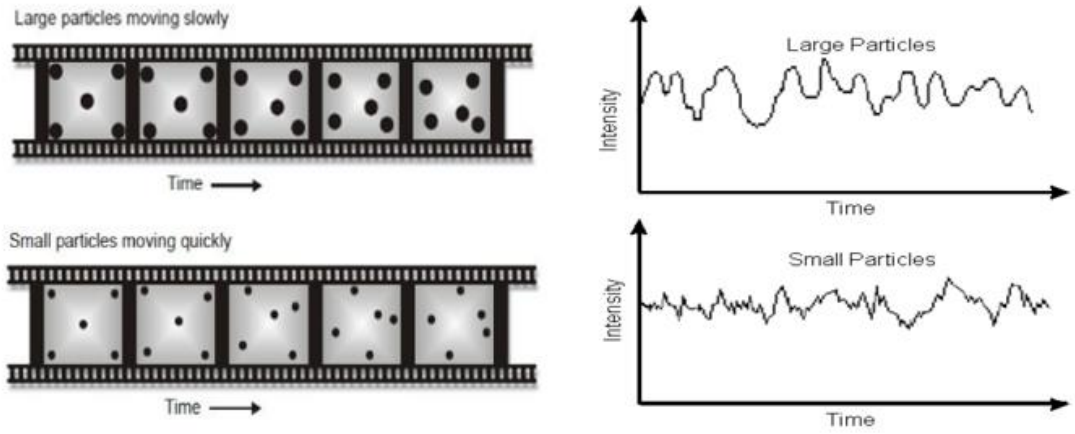

Figure 3.3. Movement of large and small particles in the suspension for large and small particles consequently on the left and the corresponding intensities over time on the right. Based on the Stokes-Einstein-Sutherland equation, ($D \sim 1/R^3$), the bigger the size the slower the diffusion in the medium and consequently the bigger the fluctuations (more scattering from big particles). On the other hand the smaller the size the larger the diffusion in the medium and the faster the intensity fluctuations (less scattering from small particles)[47].

The intensity autocorrelation function contains information about the motion of the probed particles. The following equation is the product of the normalized intensity fluctuations. This quantity calculated internally in the software with some algorithms for some of the setups.

$$g_2(\tau) = \frac{< I(t)I(t+\tau) >}{< I(t) >^2} \quad \text{Eq.3.2}$$

The intensity autocorrelation function is in fact the square of the electric field autocorrelation function –as expressed in the Siegert relation:

$$g_2(\tau) = B + \beta|g_1(\tau)|^2 \quad \text{Eq.3.3}$$

Where B is the baseline, usually taking values up to 1, and β is a coherent factor which depends on parameters such the optical alignment and the properties of the measured sample. $g_1(\tau)$ is the electric field autocorrelation function and defined as the time-correlated average scattered electric field:

$$g_1(\tau) = \frac{< E(t)E(t+\tau) >}{< E(t)^2 >} \quad \text{Eq.3.4}$$

For monodisperse systems, the electric field autocorrelation function exhibits a single exponential decay and is written as follows:

$$g_{1(\tau)} = e^{-\Gamma\tau} \quad \text{Eq.3.5}$$

Where Γ is a decay constant and τ is the lag (delay) time, defined as:

$$\Gamma = -Dq^2 \quad \text{Eq.3.6}$$

where the scattering wavevector q provides access to different length scales (figure 3.4 below) [50].

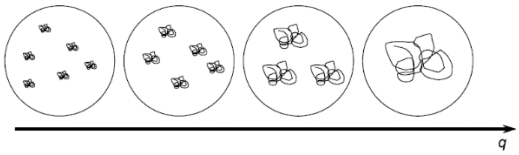

Figure 3.4. A random polymer coil observed at different length scales, from low q (whole object-zoom out) to large q (inside the object-zoom in) [50].

By using the Siegert relation and the decay constant (equation 3.3 and 3.6) we are able to extract the final relation which is the most important for having information about the diffusion dynamics. The combination of these two expressions is shown below in equation 3.7 [47]:

$$g_2(\tau) = 1 + \beta(e^{-2Dq^2\tau}) \quad \text{Eq.3.7}$$

However, the representation of equation 3.7 can be shown below as a typical representation of a correlation function [48], [50].

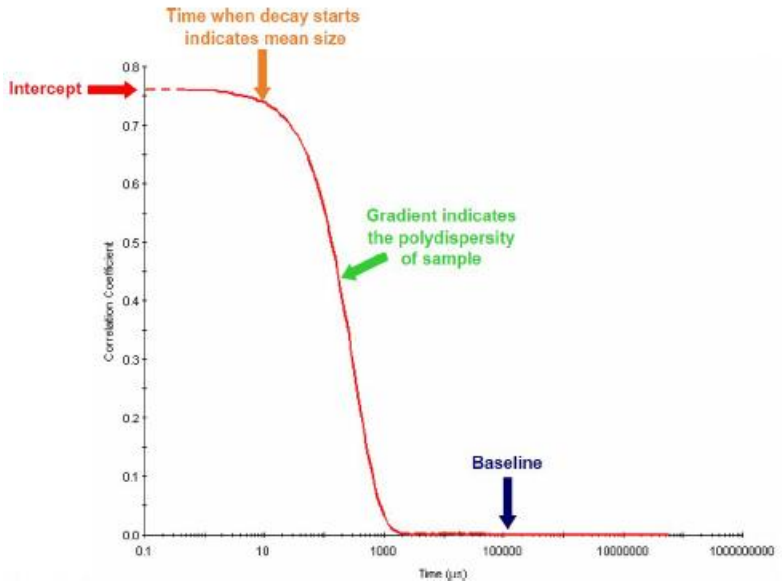

Figure 3.5. A typical result of a correlation function with vectors to indicate the main points. The red curve is the correlation function which constitute from mainly three parts: i) the first initial slope (which correspond to an intercept in the y axis) where the correlation starts to decrease exponentially, ii) the central region which indicates the sample polydispersity and iii) the baseline where the system has completely relaxed and approaches zero correlation.

In figure 3.5, the intercept which corresponds to the red color shows the values of the correlation function with the maximum to be 1 and this corresponds to the perfect correlation. Orange color is showing the initial decay of the measuring sample and the green as it is written shows the polydispersity on the sample. Finally, the blue vector indicated the baseline, which is about the end of the correlation where the system has been completely relaxed.

A correlation function can be analyzed with different algorithms starting from a simple to a more complicated ones depending on the system conditions. More details on the data fit algorithms provided in chapter 6 in the first paragraph 6.1. There we discuss in more detail all the pitfalls for these three (CONTIN, Cumulant, nonlinear cumulant analysis, NLCA) available and common tools by using core mathematical principles, examples and comparisons.

The measured diffusion coefficient D provides the value of the hydrodynamic radius of the measured object. This can be done by using the Stokes-Einstein-Sutherland

equation. Using the following relation we calculate a hydrodynamic size which corresponds to a hypothetical compact hard sphere which diffuses in a continuous medium [47], [49], [51], [52].

$$D = \frac{k_B T}{6\pi\eta N_A R_H} \qquad \text{Eq.3.8}$$

Where k_B is the Boltzmann constant (k_B=1.380*10^{-23} J/K), T is the absolute temperature, η is the viscosity of the solvent, N_A is the Avogadro number (N_A=6.023*10^{23}mol^{-1}) and R_H is the hydrodynamic radius of the scattered object.

3.1.2. Static light scattering (SLS)

After the brief introduction on DLS, is of a great importance to introduce also the second tool of light scattering, named static light scattering. In order to do this, we use the same apparatus with DLS. In figure 3.6 below, we show the difference between the two kinds of measurements. Figure 3.6, depicts the static averaged intensity from the scattered polymer/particle system, which contains information about the molecular weight of the measured object, whereas the dynamic intensity fluctuations against time reflect the diffusion dynamics of the polymer/particle. To measure static properties (time-independent) we collect the overall scattering intensity at different scattering wave vectors q (different angles, from 25^o to 150^o with 5^o angle step). Molecular weight Mw, radius of gyration Rg, and interactions in the system measured with SLS.

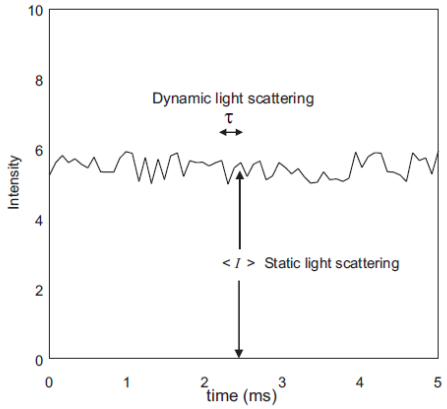

Figure 3.6. Intensity fluctuations over time and the indications for both static and dynamic light scattering. DLS and the dependency on time and SLS with the average intensity at certain time.

A combination of DLS and SLS results yields both R_H and Rg, which reflect information about the conformation of the measured object. In the following table we show some examples for some common topologies [50].

Table 3.1. Values of the ratio Rg/R_H for common morphologies [50].

Topology	ρ-ratio
Homogeneous sphere	0.775
Hollow sphere	1
Ellipsoid	0.775 - 4
Random polymer coil	1.505
Cylinder of length l, diameter D	$\frac{1}{\sqrt{3}} \cdot \ln\left(\frac{l}{D} - 0.5\right)$

A more complete assessment of the probed sample's conformation comes from the scattering function, i.e., the q-dependent intensity. As shown in figure 3.7 there are three distinct regions. The first is the intermolecular regime at which there is constant scattering intensity, the second which is the so-called Guinier regime in which we define Rg and the third one which contains the clue for the topological details [51]. Each region involved in a range of q, corresponding to different length scales. Values of that fractal dimension d_f appear in table 3.2 [50]. The calculation of that dimensionless parameter d_f can be done with the following equation:

$$I(q) \approx q^{d_f} \leftrightarrow \log\big(I(q)\big) = -d_f \log(q) \qquad \text{Eq.3.9}$$

Usually the scattering intensity I_{sc} against q represented in a log-log plot.

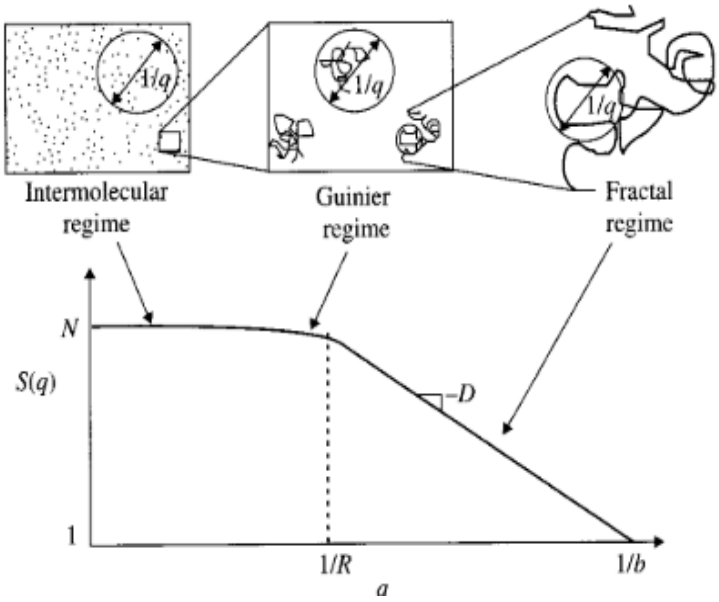

Figure 3.7. Scattering intensity as a function of the scattering wavevector for a dilute polymer solution, taken from [51].

Table 3.2. Fractal dimensions for different topologies calculated from the scattering function, taken from [50].

Topology	Fractal dimension d_f
Cylinders, rods	1
Ideal Gaussian coil	2
Gaussian coil with excluded volume	5/3
Branched Gaussian chain	16/7
Swollen branched chain	2
2D-objects with smooth surfaces	2
2D-objects with fractal surfaces	1–2
3D-objects with smooth surfaces	3
3D-objects with fractal surfaces	2–3

The low-q section of the above plot concerns the weight-average molar mass (M_w) and the second virial coefficient (A_2) determination. In a polydisperse system of a dilute polymer solution, the scattering intensity provides information about M_w [51]. This is actually the most precious result of such measurements. The calculation due to the Zimm equation is the following:

$$\frac{Kc}{R(\theta)} = \frac{1}{M_w P(\theta)} + 2A_2 c \qquad \text{Eq.3.10}$$

Where K is the optical constant defined as: $K = \frac{(2\pi n_o)^2}{N_A \lambda^4}\left(\frac{dn}{dc}\right)^2$ and especially n_o is the

refractive index of the solvent, and dn/dc is the refractive index increment between the solute molecules and the solvent; this is the measure of the optical contrast between the solute molecules and the solvent.

R (θ) is the Rayleigh ratio defined as: $R(\theta) = \frac{I_{sc} - I_{solvent}}{I_{solvent}} R(\theta)_{solv}$ with I_{sc} to be the solution scattering intensity, $I_{solvent}$ the solvent scattering intensity, and $R(\theta)_{solv}$ is the solvent Rayleigh ratio which is interpreted as $R(\theta)_{solv} = R(\theta)_{solv}(n_{solv}/n_{toluene})$. Values of $R(\theta)_{solv}$ are shown in the literature for varying solvents and consequently their refractive index n. However, the refractive index of toluene is needed since the used bath is filled with this solvent. M_w is the weight-average molar mass, P (θ) is the form factor which contains the information about the structural conformation, the extrapolation to $\theta \to 0$ gives P (θ) =1 but we do not discuss further the term form factor since in the present thesis is not examined. A_2 is the second virial coefficient and c is the polymer concentration.

For obtaining a reliable value of the molecular weight, more than three measured concentrations are required. The intercept of the Zimm equation with $c \to 0$ and $\theta \to 0$ indicates the molecular weight value and the slope the interactions in between the particles. An example of the Zimm plot is demonstrated below:

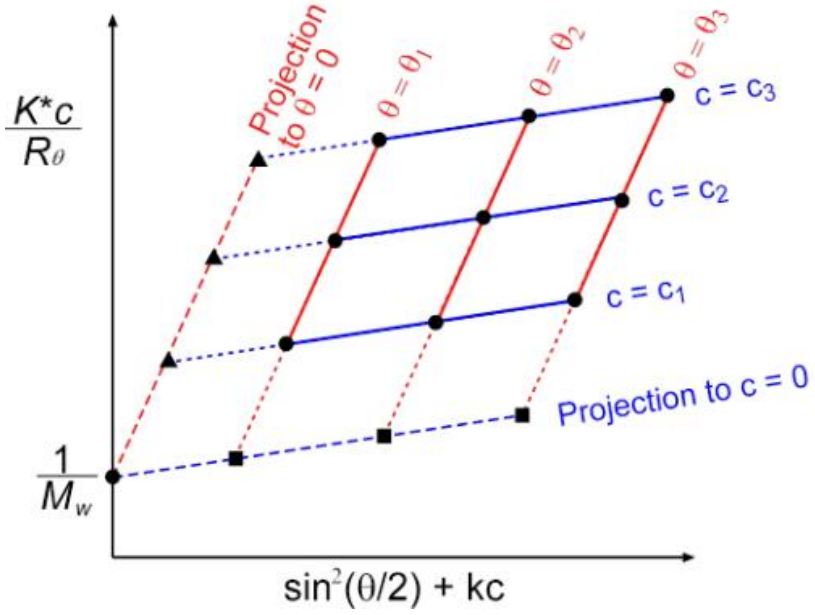

Figure 3.8. Example of Zimm plot with two projections: angle and concentration; the extrapolation to zero for both the angle and the concentration present a well-defined molecular weight and second virial coefficient.

In case of a positive slope for A_2, interactions are repulsive and contrary for a negative slope interactions are attractive in the system. For a zero slope system is ideal and there is absence of interactions.

Finally, we note some practical issues associated with light scattering. To reliably determine the parameters which can be extracted from both DLS (R_H) and SLS (Rg, Mw, A_2) we have to be careful with sample preparation. Samples which are not transparent cannot (or should not) be measured. We need also relatively large volume (~0.5ml), the sample should not absorb the light at the studied wavelength and has to be properly filtered to eliminate dust. Last but not least, we need to know the exact measured concentration which at some cases is very tricky [50].

3.2. Shear rheology

In nature there are two major categories of materials, solids (e.g. rubber) and liquids (e.g. water). The former is a purely elastic and the latter is purely viscous. The majority of our daily products are semi-solids and named as viscoelastic materials (i.e. toothpastes, creams, paints, honey). They combine properties of a solids (elastic-response) and of liquids (viscous-response) at the same time.

Rheology, is the science of deformation and flow of matter. It bridges molecular structure and product performance in applications by measuring the flow properties of viscoelastic materials (polymers and colloids) [53].

There are two types of rheometric flows, i) shear flow (with the velocity gradient perpendicular to the flow direction) and ii) uniaxial extensional flow (with the velocity gradient along the flow direction).The classic constitutive equations for elastic materials (Hookean solids) characterized by Hooke's law: $\sigma = G\gamma$ and viscous materials (Newtonian fluids) characterized by Newton's law: $\sigma = \eta\dot{\gamma}$ where σ is the shear stress, γ is the shear deformation, G is the shear modulus (indication for stiffness), $\dot{\gamma}$ is the deformation rate and η is the shear viscosity (indication of resistance to flow). However, the greater number of such materials are non-Newtonian and they are challenging for rheological investigations.

There are two types of commercially available rotational rheometers, strain-controlled and stress-controlled (figure 3.9), both measure rheological data but they differ in a way of measuring. In the present work, measurements were performed

with both a strain-controlled rheometer (ARES from TA instruments, USA), equipped with a force balance transducer (2KFRTN1) and a stress-controlled rheometer (MCR 501 from Anton Paar, Austria). More details on the experimental part, geometries used and technical issues are written in chapter 7. The main tests typically performed are: i) steady shear and ii) oscillatory experiments.

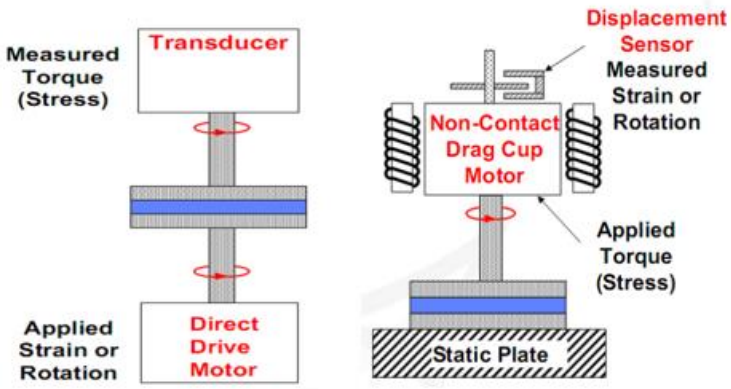

Figure 3.9. Cartoon representation of a strain-control rheometer (left) with a separate motor and transducer and a stress-control rheometer (right) with a combined motor and transducer.

In rheometry, we use different measuring fixtures depending on material functions. In figure 3.10, we represent three of the most widely used tools in rheometers for testing samples. The volume of the sample depends on the geometry [54]. Depending on the sample and desired properties, there is a host of different geometries, such as double wall couette, cone and plate and cone-particionate plate[55].Here, we used only cone and plate geometry with different plate diameters and different cone angles (especially 25mm, 50mm with cone angles 0.02 rad and 0.0175 rad concequently).

In particular, we discuss in a very simple way how a rheometer works and we present different experimental tests. There are linear and nonlinear measurements. Thee former probe the equilibrium viscoelastic character of the material whereas the latter reflect the induced conformational/structural changes upon application of a large (deformation or stress) field.

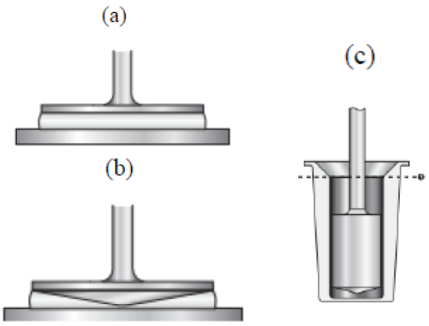

Figure 3.10. Different geometries correspond to different measurement classification. For example in a general rule, very dilute solutions measured with couette geometry (c) since it provides trustable torque. Cone and plate (CP) geometry (b) is for more viscous samples and plate and plate (PP) is for even more viscous conditions, solid-like response.

3.2.1. Steady shear rheology

For a comprehensive description we use the so-called two-plate model; a simple model to understand the flow behavior. Figure 3.11 represents an immobile bottom plate (blue) and a mobile top plate (blue). Between the two plates, sample is placed (brown) with a specific height, the gap y which is the distance between the plates. Force is applied to the plate vertically within the area A and the resulting stress is defined as the force applied to that surface per unit area:$\sigma = \frac{F}{A}\left[\frac{N}{m^2} = Pa\right]$. Although, the shear rate determinates the viscosity of the system due to Newton's law; and can be extracted as follows:

$$\dot{\gamma} = \frac{d\gamma}{dt} = \frac{d}{dt}\left(\frac{dx}{dy}\right) = \frac{du}{dy} = \frac{v}{y}\left[\frac{1}{s}\right]$$

the velocity of the upper plate, v and the thickness of the sample y.

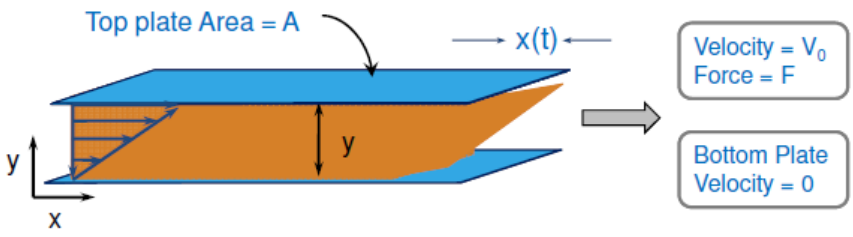

Figure 3.11. The two-plate model for a simple steady shear flow, sample is sandwiched between the plates and stress is applied, the measuring parameters are the strain, γ and the strain rate, $\dot{\gamma}$.

Shear experiments included in a rotation mode of a rheometer and the main information is about the dynamic viscosity, η and the modulus, G. Flow behavior is

tested under parameter of time, temperature and shear rate in most of the cases.

3.2.2. Oscillatory rheology

Oscillatory rheology probes the dynamics of the system under time-periodic excitation. This technique is standard for the behavior of the viscoelastic materials. In this way we can visualize the elastic and the viscous contribution and in order to do that we use sinusoidal deformations and not simple shear. In the following picture, we can visualize these deformations with the corresponding response:

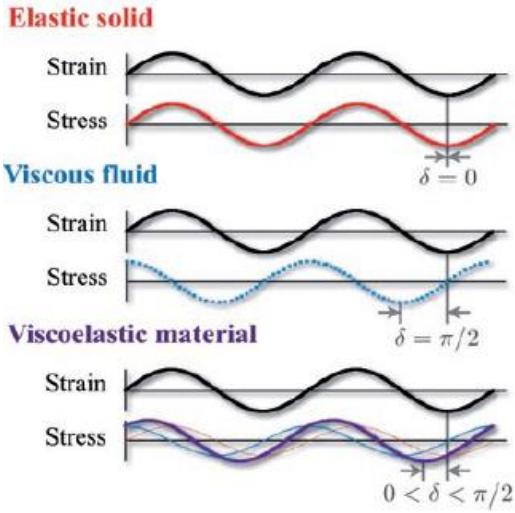

Figure 3.12. Comparison of an ideally elastic, viscous and viscoelastic behavior under oscillatory shear strain and its response in stress with the corresponding angle shift.

In a purely elastic solid the applied sinusoidal deformation provides a stress which has no phase shift, δ=0.

In a purely viscous liquid the applied sinusoidal deformation shows an angle shift of δ=90º.

Viscoelastic materials are challenging since their response appear somewhere among elastic and viscous behavior, their angle shift is from 0º to 90º. The elastic contribution coded as G' (ω) and the viscous as G'' (ω).

The time dependent strain applied is: $\gamma(t) = \gamma_o \sin(\omega t)$ and the corresponding measured stress is: $\sigma(t) = \sigma_o \sin(\omega t + \delta)$.

Where ω is the angular frequency, γ_o is the strain amplitude and consequently σ_o is the stress amplitude. The phase shift is δ and t is the experimental time. For viscoelastic materials by using the Hooke's law we can define the final stress calculation, which is the following[56]:

$$\sigma(t) = G'(\omega)\gamma_o \sin(\omega t) + G''(\omega)\gamma_o cos(\omega t)$$

$$G^* = G' + iG'' \qquad \text{Eq.3.11}$$

Where the first term in the right hand side of equation 3.11 signals the elastic contribution (real part) and the second one the viscous contribution (imaginary part). G* represents the so-called complex material modulus. In case at which the material is solid-like the G' is greater than G'' and vice versa. To understand this there is a dimensionless parameter called loss tangent. It is the ratio of G'' and G': tanδ=G''/G' (>1 liquid-like and <1 solid-like). Next, we cite very briefly the fluid flow behavior and a short list of such experiments.

<table>
<tr><th colspan="2">Steady Shear Rheology</th></tr>
<tr><td> 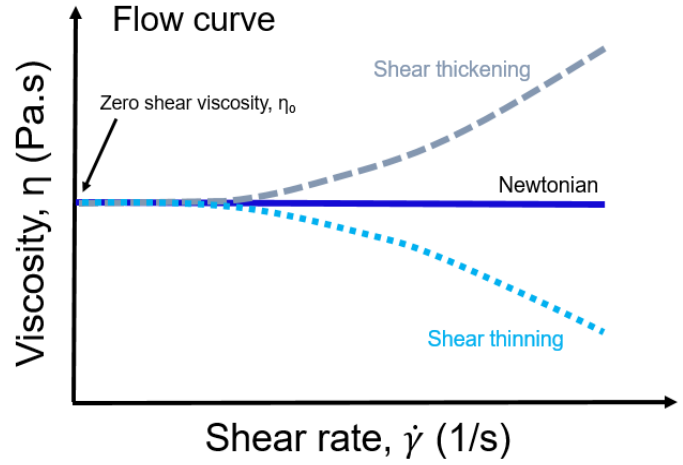
</td><td>We control the shear rate and we extract information about the flow behavior of the tested fluid. Newtonian fluid is independent of the applied shear rate.</td></tr>
<tr><td> 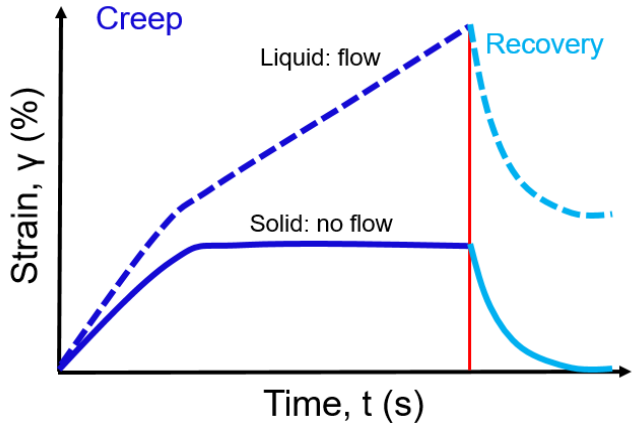
</td><td>We control the stress applied (σ) and we extract information about the flow behavior at very long times which are not detectable from a frequency sweep test (DFS shown below)</td></tr>
<tr><th colspan="2">Oscillatory Rheology</th></tr>
</table>

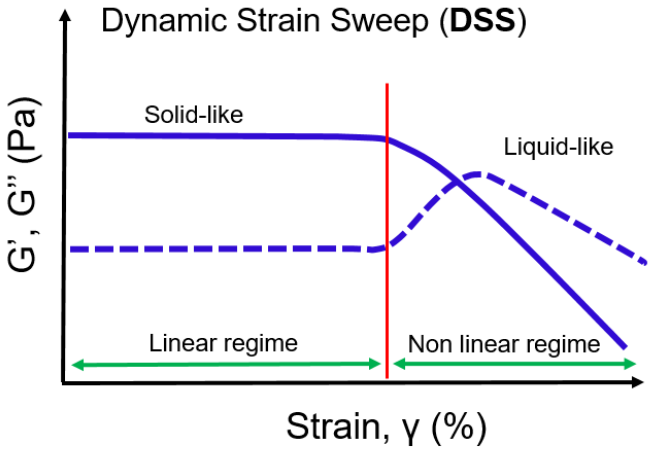	We control the frequency applied (ω) and we extract the viscoelastic behavior in the linear regime as well as in the nonlinear regime.
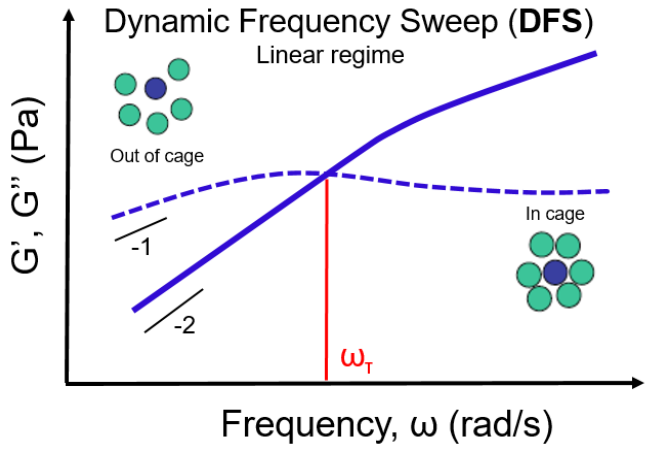	We control the strain applied (γ) and we extract the relaxation times in the system.

- Elastic part (storage modulus)**, --** Viscous part (loss modulus)

3.3. Capillary break-up extensional rheology (CABER)

In this section we discuss the elongational stretching. One of the popular methods to measure the extensional properties of viscoelastic materials which undergo a uniaxial deformation is the capillary break-up extensional rheometer. However, another rheometer which is popular and commercially available except CABER is the filament stretching rheometer (FSR) and it is also attractive. It measures the force in the bottom plate whereas CABER does not, but it lacks in the measuring range of viscosity in comparison to CABER [57].

The main principle of CABER is illustrated in the picture below. The investigated sample is placed in between two cylindrical plates with a diameter D_o and a stretch is applied to the system uniaxially. The filament starts to thin and after a certain amount of time it breaks [58]. The main parameter measured via CABER- with a laser

micrometer- is the diameter of the filament over time. By having this value we can extract further information for the system and especially the relaxation time and the extensional viscosity.

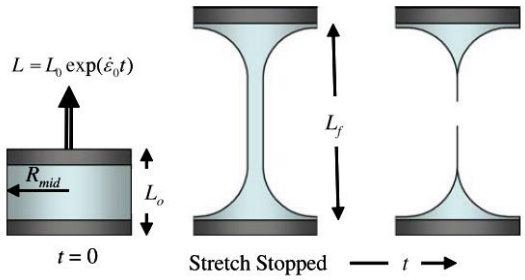

Figure 3.13. Cartoon representation of the CABER setup. Left: sample is in equilibrium, middle: sample is stretched, right: breakup of the sample , taken from [59].

The liquid remains into the cylindrical plates because of the adhesive forces. Sample creates the so-called elastocapillary bridge due to the balance of the capillary and elastic stresses within the viscoelastic solution. Viscous forces overwhelmed from elastic forces and the filament breaks.

A cartoon representation of the HAAKE-CaBER (Thermo scientific) instrument shown below (figure 3.14). Two plates with a diameter of 6 mm (grey), one in the top (moving plate) and one in the bottom (stationary plate) keep the sample droplet (yellow) in between due to the surface tension, σ. A linear drive force is applied to the upper plate and instantaneously the plates are separated. Once the fluid filament is stretched the diameter reduces its value and it is recorded via a laser micrometer which collects the signal in the detector. The signal provides information about the diameter of the filament against time.

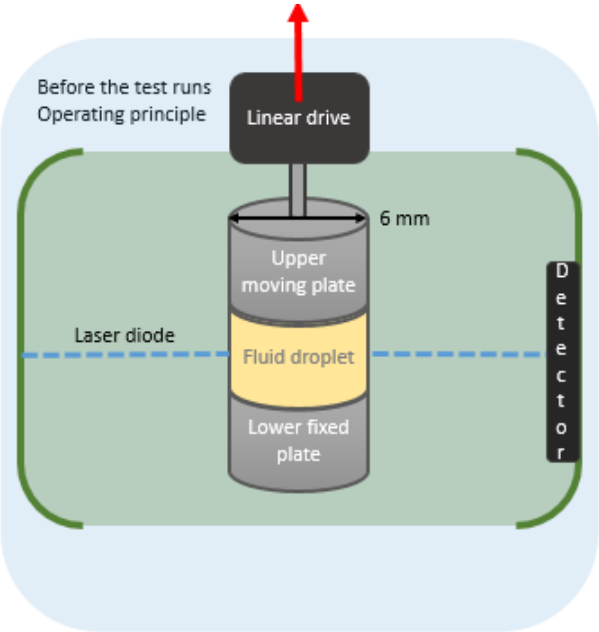

Figure 3.14. Cartoon representation of the experimental setup (HAAKE-CABER).

The relaxation time of the material can be subtracted from the following empirical equation derived from the Maxwell model (with one characteristic relaxation time). The diameter of the filament decreases exponentially over time [58]–[60].

$$\frac{D(t)}{D_o} = \left(\frac{GD_o}{4\sigma}\right)^{1/3} \exp\left(-\frac{t}{3\lambda}\right) \qquad \text{Eq.3.12}$$

Where D (t) is the time-dependent diameter of the filament, D_o is the diameter of the measuring plate, G is an apparent modulus, σ is the surface tension of the measuring system, t is the experimental time and λ is the relaxation time of the material. It is referred as relaxation time since it is the same time in comparison to steady shear experiment and its stress relaxation afterwards.

The graphs below (figure 3.15) show typical experimental results. In the left plot, the diameter of the PEO solution decreases exponentially with time as expected and the viscoelastic plateau fitted with the empirical equation. The next plot shows the different regions during the experiment (i. Plate separation, ii. Filament thinning and iii. Breakup filament). At this point is important to notice the meaning of BOAS (Beads-on-a-string) effect. These are some instabilities in the system (shown also in the picture in the inset of figure 3.15, right) before it breaks. This phenomenon has received a lot of interest since people trying to understand the physics of this mechanism [60]–[63].

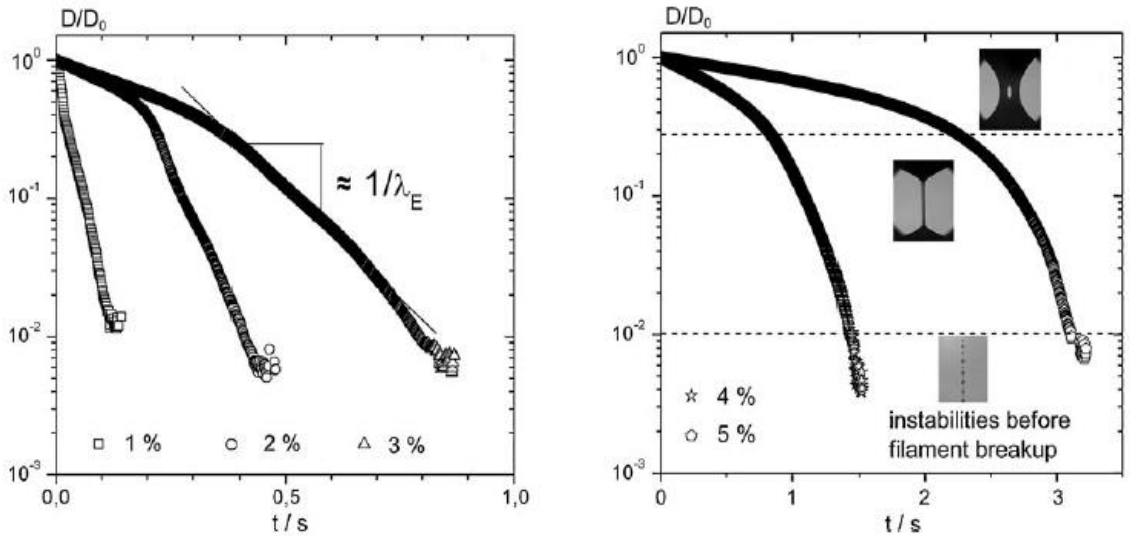

Figure 3.15. Left plot: High molecular weigh of PEO (Mw=10^6 (g/mol) at three different concentrations (1%, 2% and 3%). The line represents the exponential fitting (eq. 3.12) of the so-called viscoelastic plateau. The fitting applied in the linear regime of the semilog-plot in order to extract the relaxation time λ of the elastocapillary thinning. Right plot: High molecular weigh of PEO (Mw=10^6 (g/mol) at two different concentrations (4% and 5%).

Equation 3.12, applied for a viscous solutions since we observe a plateau which highlights this property of viscoelasticity. In figure 3.16, there is the representation for a Newtonian fluid, the thinning of the filament is linear with time and has different shape, is shown in figure 3.16 below; equation 3.12 cannot be applied since there is absence of that viscoelastic plateau. However, besides thinning another main difference between viscoelastic and Newtonian fluids is the time frame at which the filament breaks. In the case of a viscous solution (extensional viscosity increases) the time needed for the bridge to break is much longer than in a perfect liquid (constant extensional viscosity). The extensional viscosity of the system is given by the following equation.

$$\eta_E = \frac{\sigma}{\frac{R_{mid}}{\dot{\varepsilon}(t)}} = -\frac{\sigma}{\frac{dD_{min}}{dt}} \qquad \text{Eq.3.13}$$

Where σ is the surface tension of the tested solution, η_E is the extensional viscosity, R_{mid} is the radius of the stretched filament and $\dot{\varepsilon}(t)$ is the strain rate. The strain rate defined as: $\dot{\varepsilon}(t) = \frac{\varepsilon(t)}{t}$ where ε is the strain and t is the experimental time. The parameter ε is the system Hencky strain and it depends on the viscoelasticity of the

sample since it is defined as: $\varepsilon = -2\ln(\frac{D(t)}{D_1})$ where D (t) is the time dependent filament diameter and D_1 is the diameter of the filament after 50ms which is the strike time (time needed for the plates to be separated).

A characteristic example of such experiments is demonstrated in figure 3.16 below, where two different materials thin against time. In the top image is a Newtonian fluid (glycerol) and in the bottom a viscoelastic solution (mucin proteins in water). The way of thinning and the shape of the capillary in a parallel comparison of time provide the signature for the presence of elastic stresses in the viscoelastic solution. The break-up time is much greater (roughly three times) in case of the non-Newtonian fluid.

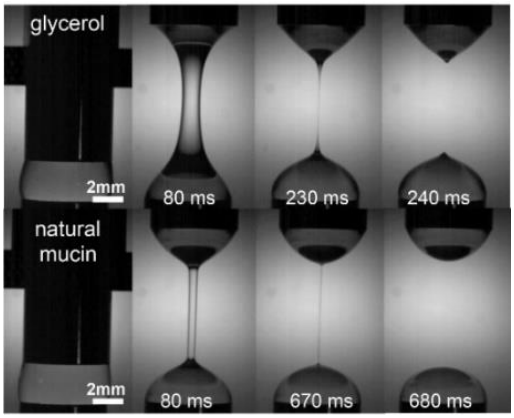

Figure 3.16. Example of capillary thinning for two different materials. On the top a Newtonian fluid (glycerol) and on the bottom a viscoelastic solution (here mucin proteins in water). The viscoelastic solution needs 3x more the time needed for the Newtonian fluid to break.

3.4. Ultra-violet visible spectroscopy (UV-VIS)

This technique is useful for the compounds characterization in a solution and the determination of its concentration. It measures the light which absorbed or transmitted from the solute substances. In the picture below we illustrate the fundamental instrumentation. The main principle is the following:

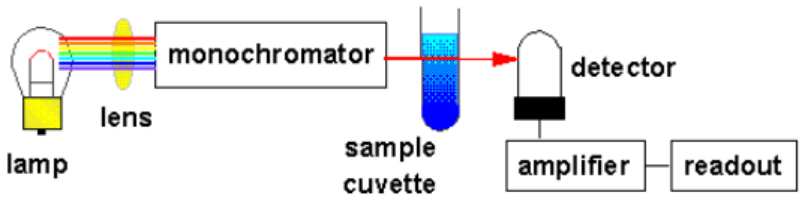

Figure 3.17. Simplistic cartoon representation of the UV-vis spectrometer.

The light from the source passes through lens and it arrives to a monochromator

where the light analyzed to different colors. In continues analyzed light arrives to the solution and each substance which absorbs gives a specific intensity. The intensity collected from the detector and finally we extract the absorption against wavelength, λ.

The range of the visible light starts at 400nm and reaches 800nm, from violet to red. However a UV-visible spectrometer (LAMDA 950, Perkin Elmer) - which is the case here- has a range of wavelengths from 200nm to 800nm. The Beer-Lamberts law is the basis of spectrometry. The following equation shows the analogous between the absorption, A of the substances, the pathlength of the measured cuvette, l and the intensities detected I (where I_o is the incident intensity and I is the transmitted intensity)[64] :

$$A = \log(\frac{I_O}{I}) = \varepsilon l C \qquad \text{Eq.3.14}$$

One of the most important consequences of the use of this technique is, as mentioned above, c the concentration determination of the substances. The way to do so, is by means of calibration curves when measuring many concentrations and their absorption. In order to build it, we begin from very dilute solutions and we increase further the concentration or vice versa till to extract a trustable linear region. We do not use concentrated solutions (the concentration should not exceed the threshold of 0.001-0.01 mol/L) since interactions in the solution dominate between the solvent molecules and the absorbing species (hydrogen bonding) [65].

.

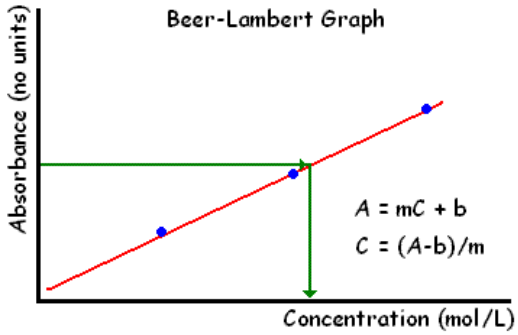

Figure 3.18. Beer-Lambert graph, concentration determination in the linear regime.

Chapter 4: Materials

This chapter discusses the materials used in this thesis. They are i) a synthetic colloidal suspension of a poly-N-isopropyl acrylamide microgel particles (PNIPAM) in water and ii) a biological hydrogel of mucin-like glycoproteins originating from hagfish slime. In the first part, we present the sample preparation protocol and the particles characterization via dynamic light scattering. In the second part, we refer the biology of hagfish slime with a special emphasis on mucin-like glycoproteins. Finally, we address the issue of concentration determination in such proteins.

4.1. Synthetic thermosensitive microgel

4.1.1. Poly-N-isopropyl acrylamide suspensions as model tunable colloids

As referred in chapter 2, microgels, i.e., chemically cross-linked particles, represent a promising and tunable soft colloidal system. In addition, PNIPAM is thermosensitive, hence possess an extra degree of freedom. The size of these particles decreases reversibly as the temperature increases. There exists extensive literature on the topic [66]. On the left graph captured from H. Senff et al.[27], we depict the typical size transition of such a system. The transition happens at 32-33ºC, which is the theta point for (homopolymer) PNIPAM [67]. Upon increasing the temperature, water becomes a bad solvent for this polymer and its size decreases because the interactions between monomers are favorable (hydrophobic) whereas by decreasing temperature hydrophilic interactions dominate and the polymer swells. The variability in size strongly affects the rheological properties of the suspension through the change in volume fraction. For high temperatures (above ~30ºC) the interactions become predominantly attractive whereas for low temperatures they are repulsive [28].

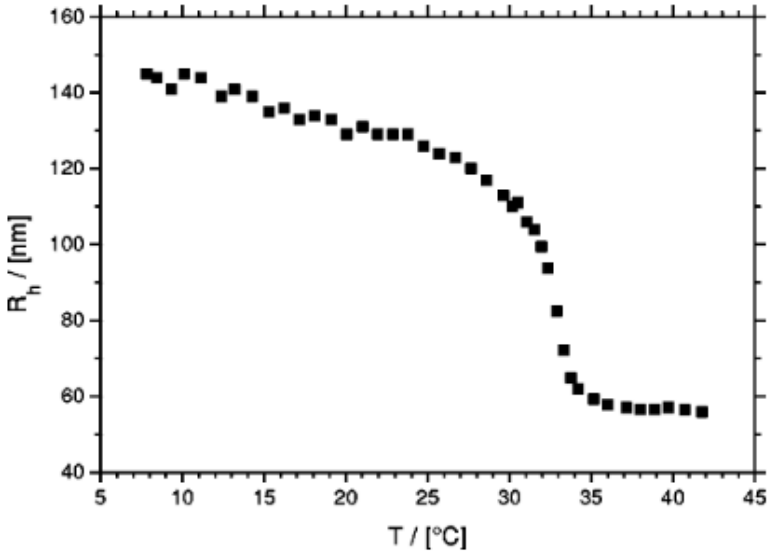

Figure 4.1. Reduction of the hydrodynamic radius over a wide range of temperatures for PNIPAM microgel particles, taken from [27].

4.1.2. Synthesis of PNIPAM microgel particles

Microgel particles are relatively easy to synthesize. Their key characteristics such as, the softness, the size, the swelling capacity and the optical properties strongly depend on the sample preparation. The size usually controls the optical properties due to the refractive index (large particles yield turbid suspensions) and the cross-linking density controls the softness via the particle modulus, and the resulting morphology and dynamic properties, especially at high concentrations.

The most common way to prepare these kind of particles is by means of free radical polymerization. The main components are: i) the NIPAm monomer (N-isopropylacrylamide), ii) the initiator and the iii) the cross-linker BIS (N,N-methylene bisacrylamide). In our case, the cross-linking density corresponds to 2.5 % by weight of NIPAM monomer [68]. Figure 4.2a[68], illustrates the chemical structure of the cross-linker used (BIS) along the amide groups. The final structure of the polymer is shown below, figure 4.2b[68].

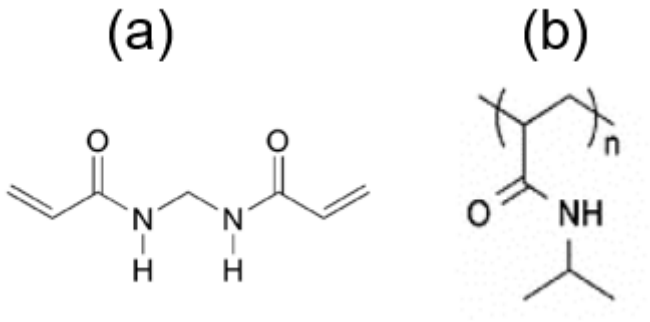

Figure 4.2.(a)The cross-linker named N,N –methylene bisacrylamide (BIS); (b) Poly-N-isopropylacrylamide (PNIPAM) chemical structure, figure taken from [68].

As mentioned, PNIPAM microgels are sensitive to temperature. In general, there are two types of thermodynamic transitions depending of the nature of the system. These are: i) the upper critical solution temperature (UCST) and ii) the lower solution temperature (LCST)[28]. Thermoresponsive PNIPAM microgels such as the present ones, are shown in figure 4.3 and belongs to the LCST type of systems transition temperature (theta) in the range 32ºC-33ºC as already mentioned above.

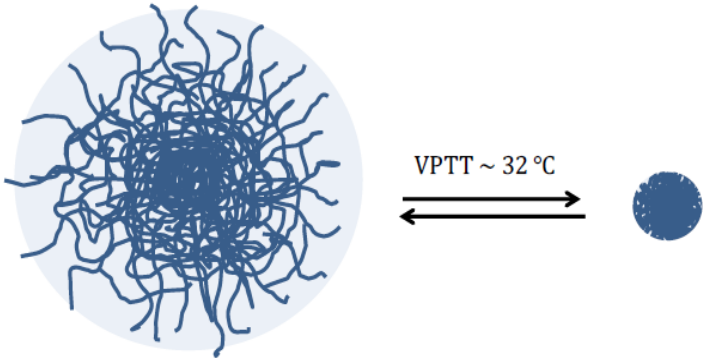

Figure 4.3. Cartoon representation of a PNIPAM microgel particle with reversible volume transition. The swollen state (left) is below the LCST and the collapsed state (right) is above the LCST[68].

As one may observe from figure 4.3, the cross-links are not uniformly distributed throughout the particle. In the core, the structure is denser (many cross-links) and in the shell is less dense (less cross-links). The outer part provides also a steric stabilization in the system and the segments with a free end are usually called dangling ends. These side chains in combination with the charges in the particle surface coming from the initiator reduce the risk of aggregation.

4.1.3. Sample preparation for light scattering experiments

The sample preparation process before light scattering (LS) is crucial in order to extract sound quantitative LS information from a well-characterized system. Parameters such as size, molecular weight and shape can be trustable if the sample is properly prepared. Since we deal with (laser) light, an important parameter is the dust. The presence of dust (which scatters a lot) can be detrimental for the measurement.

Dilute solution was prepared by using PNIPAM powder and nanopure water. The estimated concentration was about 0.0096 wt. %. The solution was prepared in a vial and kept in the fridge. Once the powder was completely dissolved in water, the sample was ready to be measured. In order to perform a light scattering experiment, we need to use appropriate light scattering cells and this is discussed in the next paragraph.

There are different kind of cells in terms of size (nmr tubes with diameter of 5mm, quarz or pyrex glass tubes with diameter of 10mm and 20mm). The larger the diameter the larger the scattering volume. For example, assuming that we have very small particles of diameter 10nm, nmr tube is the right choice; however this is not the case for particles with size exceeding 500nm[50].

The cleaning procedure involves using acetone with a filter of 0.45μm and repeating this procedure three times. Subsequently, we use aluminium foil in order to cover the cap and the cell and we place the glassy cells in the vacuum oven for roughly 20 minutes for drying. After 20 minutes, we add the sample into the cell by using a syringe with a hydrophilic filter having 5μm pore size.

The sample was kept in the fridge (4^{o}C) overnight in order to equilibrate and be measured the next day (even if we work in the very dilute regime). The next day, the sample was placed in the light scattering setup for 60 minutes in order to achieve a temperature equilibration at 15^{o}C. The bath temperature was controlled to within $\pm$0.1 ^{o}C.

4.1.4. DLS characterization

The goal of these DLS measurements was to characterize our system in terms of size and especially how does it vary if the temperature varies. We measured five different scattering angles (30º, 45º, 60º, 90º, 150º) and each angle for more than 1000s. Several temperatures were measured from 15ºC to 40ºC, which correspond to its completely swollen state at low temperatures and fully collapsed state at high temperatures (due to LCST behavior). The waiting time between the temperatures was more than 30 minutes for appropriate equilibration.

In Figure 4.4 we show typical results of the intermediate scattering (time autocorrelation) functions for four different temperatures. The system seems to relax at long times and the contrast in the correlation function is very close to one. Only at 20ºC, we observe some long-time processes at small scattering angles (30º and 45º), which possibly originate from small aggregates in the system. For 20ºC and 40ºC at low angles (30º and 45º) we could also consider a double exponential decay process but for simplicity (since we care about the main mode here for characterization) we do not. The data were fitted with Kohlrausch-Williams-Watts (KWW) equation by using single exponential decay process:

$$C(q,t) = g_1(t) = b + \exp\left(-\frac{t}{\tau}\right)^{\beta} \qquad \text{Eq.4.1}$$

where $g_1(t)$ is the field correlation function, b is the baseline, τ is the relaxation time of the particles and β is the so-called stretched exponent. The latter takes values between 0 and 1. In case where β<0.8 there is a subdiffusive motion, 0.8<β<1 is a diffusive motion and β>1 is a superdiffusive motion (ballistic).

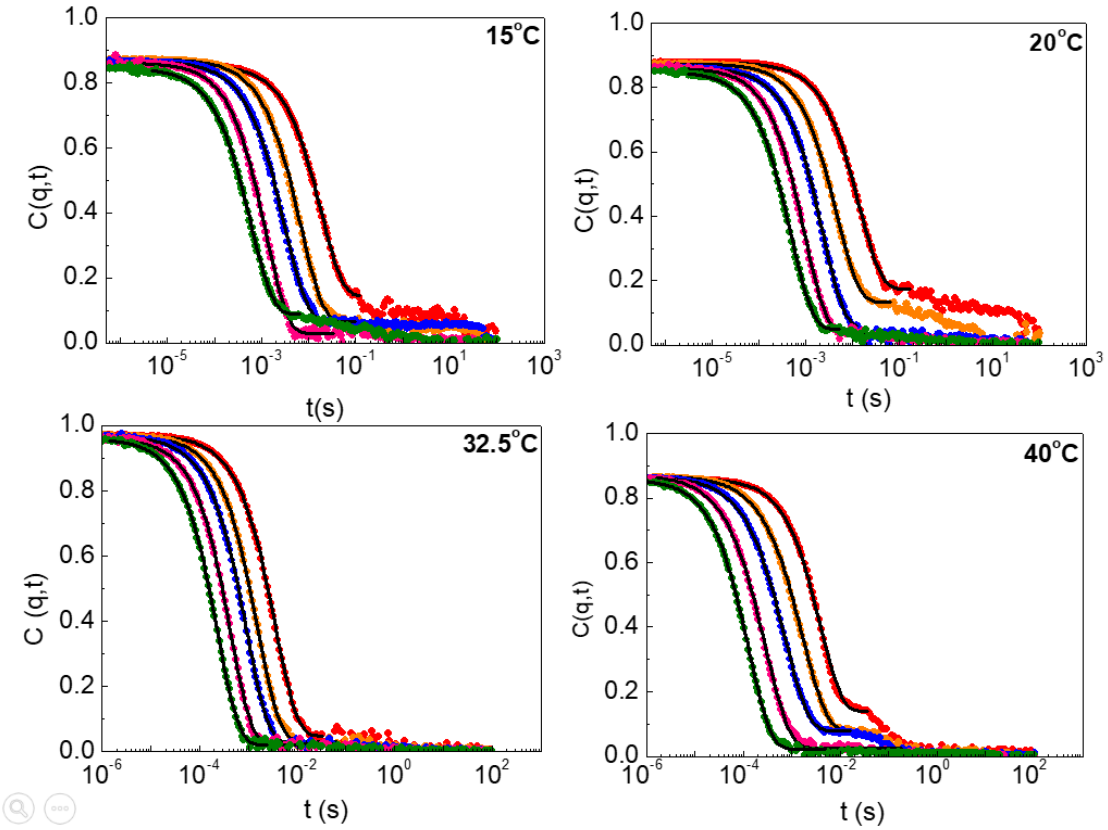

Figure 4.4. Normalized correlation functions (intermediate scattering functions, ISF) of B25 PNIPAM suspension in water for four characteristic temperatures (15°C, 20°C, 32.5°C, 40°C). Different colors correspond to different scattering angles, red: 30°, orange: 45°, blue: 60°, pink: 90° and green: 150°. Data fitted with KWW equation with a single exponential decay process.

The KWW fitting procedure yielded a single exponential decay of the ISF for the whole range of angles and the whole range of temperatures. For the calculation of the diffusion coefficient, D we used the plot of figure 4.5. The hydrodynamic radius, R_H of the microgel particles was then determined by means of the Stokes-Einstein-Sutherland equation. The viscosity values of the solvent (water) for the different temperatures provided by Anton-Paar. Results are depicted in figure 4.6.

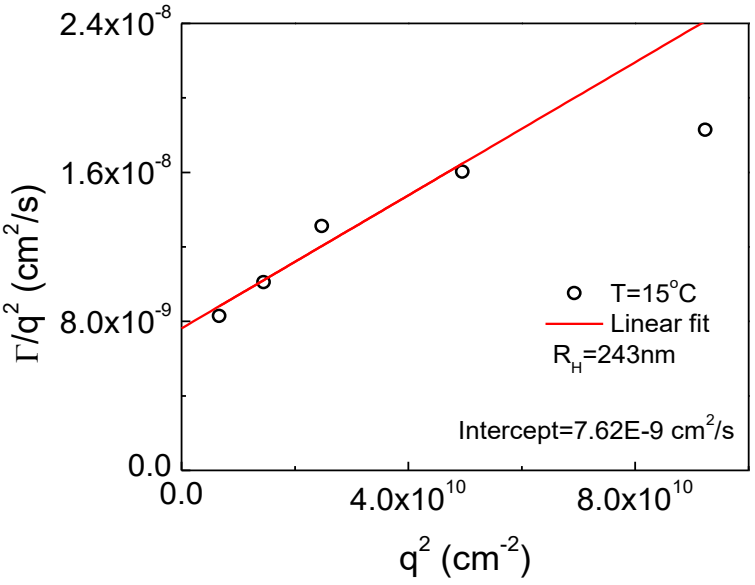

Figure 4.5. Calculation of the apparent diffusion coefficient by using the relaxation time, τ extracted from the KWW fitting process. The plot shows the decay time over the scattering wavevector against the scattering wavevector and the intercept of the linear fit indicates the diffusion coefficient through the relation $D=\Gamma/q^2$.

The value of the hydrodynamic radius at 15ºC was 243nm in its most swollen state. By increase the temperature the size was decreasing. In the blue region interactions are repulsive and beyond the theta temperature they become attractive and the particle collapses. Table 4.1 lists the results.

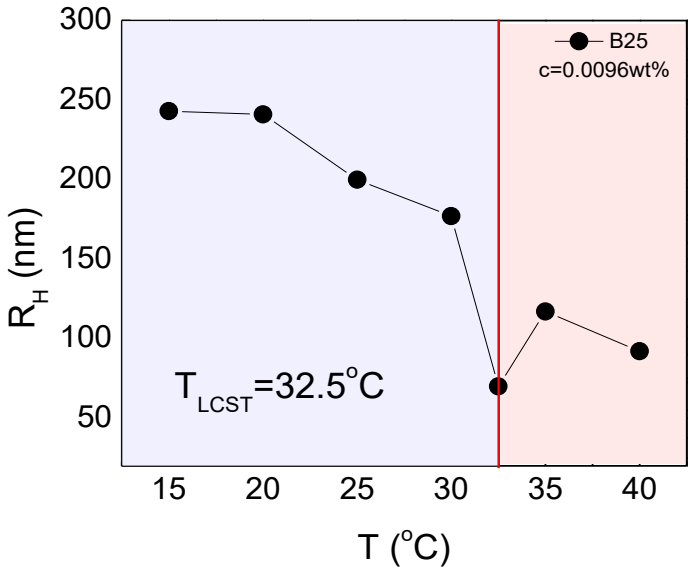

Figure 4.6. Hydrodynamic radius against temperature for a dilute PNIPAM microgel suspension. Sample coded as B25 and the measured concentration is about 0.0096wt. %. The LCST temperature of this system is 32.5°C which correspond to a radius of 70nm. The blue color is for the temperatures below LCST and the red color is for the temperatures above LCST.

Table 4.1. Viscosity and hydrodynamic radius at different temperatures for sample B25 with concentration of 0.0096wt. %.

Temperature (°C)	Dynamic viscosity (mPas)	Hydrodynamic radius (nm)
15	1.1375	243
20	1.0016	241
25	0.8900	200
30	0.7972	177
32.5	0.7566	70
35	0.7191	117
40	0.6527	92

Another representation of the reflection of changing temperature on the diffusion (and size) is shown in figure 4.7. By increasing the temperature, attractions dominate and the decay time decreases, in the dilute regime.

At higher concentrations, in the dense regime the higher temperature does not only affect the interactions within one particle (intra-particle interactions) but also between particles (inter-particle interactions). This is investigated with rheological measurements for concentrated suspensions and it is discussed in chapter 5.

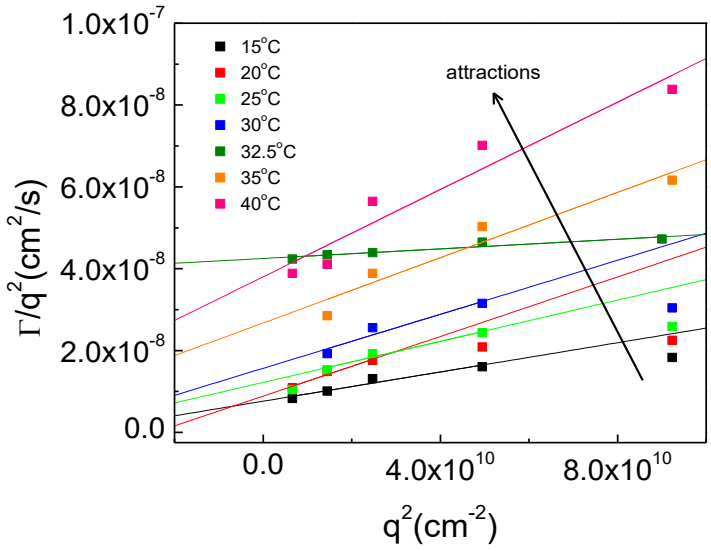

Figure 4.7. Characteristic relaxation rate over the square of the scattering wavevector against the square of the scattering wavevector for different temperatures. Different colors correspond to different temperatures and the higher the temperature the more the attractions in the system. The relaxation time decreases since the size due to the attractive interactions within the polymer increase.

4.2. Biological hydrogel

The hydrogel based on hagfish slime is a natural polyelectrolyte system. To put the work into perspective, we first introduce the biology of a jawless fish named hagfish. Then we focus on mucin-like proteins and discuss the importance of sample preparation under two aspects: i) the slime collection and the stabilization of mucin vesicles and ii) the network formation. We end-up with the procedure followed in order to estimate the concentration of mucin vesicles in a given sample.

4.2.1. Hagfish slime and its biology

A marine invertebrate animal named ‘‘hagfish’’ is shown in figure 4.8 below. Hagfishes leave very deeply into the ocean (typical depth being larger than 100 meters) and are known to exist since more than 300 years. They are usually fed by dead animals in the seafloor. There are many different hagfishes in the oceans but the ones most studied are: i) the Myxine glutinosa L. (from the Atlantic ocean, Norway) and ii) the Eptatretus Stoutii (from the Pacific Ocean). In the present work we investigate the former, which was obtained in Norway[69], [70].

Figure 4.8. Atlantic hagfish, the myxine glutinosa (Norway)

Hagfishes are very famous for their ability to defend themselves by using their body. As you can see in Figure 4.8, there are little “white dots” in the ventrolateral place of the animal and the so-called exudate. These are slime gland pores (with a diameter of roughly 2mm) and they are located symmetrically in both sides of the fish. These appear when hagfish is attacked or stressed[11], [42]. When it comes in contact with seawater, the exudate produces the slime in a few milliseconds in order to defend itself against predators. Indeed, the large volume of slime is produced after an attack as a defense mechanism[71].

Figure 4.9. Hagfish slime

When the slime is released from the hagfish it causes gill suffocation and clog mouth of other fishes (predators) in the ocean. In this way, the hagfish is protected from bigger animals (e.g. a shark). The slime has the ability to reduce the water flow in the gills and this causes the suffocation. At this point is important to note that, there is the possibility that hagfish can suffocate itself in his own slime, but Mother Nature has already foreseen this and given a smart solution. By doing a knot, as nicely shown in work of L. Böni [11] in Figure 4.10 below, hagfish can escape its slime.

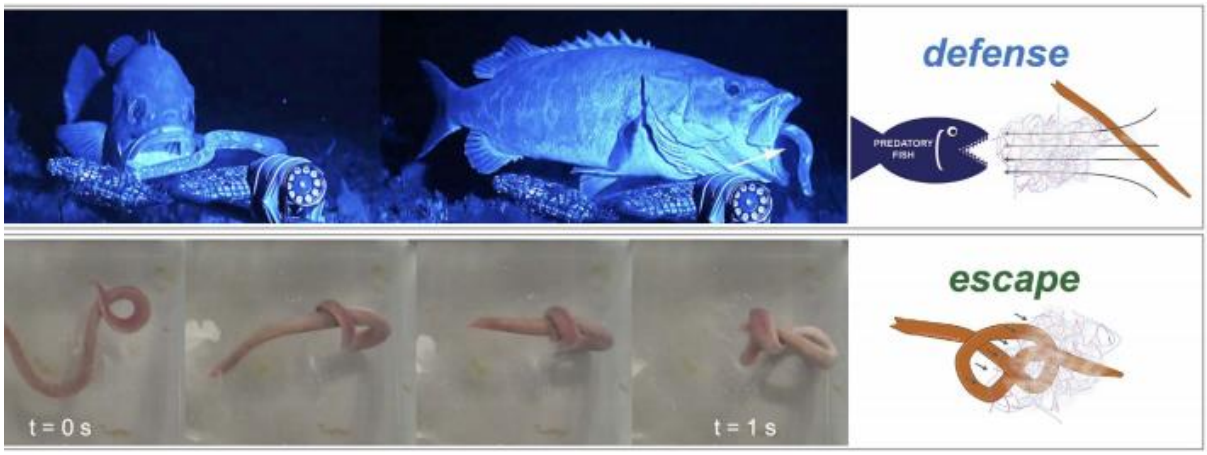

Figure 4.10. Defense and escape mechanism with hagfish slime. In the top of the figure there is the defense mechanism from the hagfish to the bigger fish, in its mouth suffocation and in the bottom there is the escape mechanism at which hagfish by knotting itself escapes the slime. For both mechanisms there is a cartoon representation on the right side of the image [11].

The composition of the slime involves two main components (protein skeins and mucin vesicles), as explained in Figure 4.11 below. Inside the gland slime pores there are two secretory large cells. These are: i) gland thread cells (GTCs) and ii) gland mucus cells (GMCs) [43], [71], [72]. Both act synergistically in order to release their components via interactions to create the slimy network.

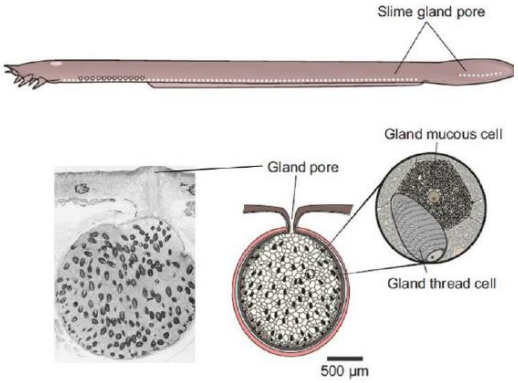

Figure 4.11. Cartoon representation of hagfish in the top of the picture, with the 'white dots' its body from both sides respectively to be the slime gland pores. The microscope image is a SEM image which represents the gland pore and as shown next to this is the cartoon illustration of the gland pore. Inside the pore there are: i) gland mucus cells and the ii) gland thread cells. Picture captured from Herr et al. 2014[43].

The GTCs contain the single protein thread skein, consisting of intermediate filament proteins which are coiled-up in an elliptical shape (150μm long and 50μm wide). On the other hand, the GMCs contain mucin vesicles (1-3μm length), which contain packed mucin-like glycoproteins. Mucin vesicles are surrounded from a single bilayer membrane. Below, we describe the mechanism of the slime formation.

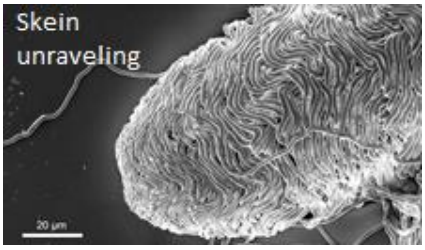

The skeins unravel in seawater (figure 4.12) and they provide a protein thread rich in intermediate filaments with a length of roughly 15-30cm and diameter of 1-3µm[13].

Figure 4.12. Skein unravelling of the intermediate filaments (protein threads) in water.

In Figure 4.13 we show a microscope image of a non-unraveled skein and the corresponding cartoon illustration of skein which unravels when in contact with water [11].

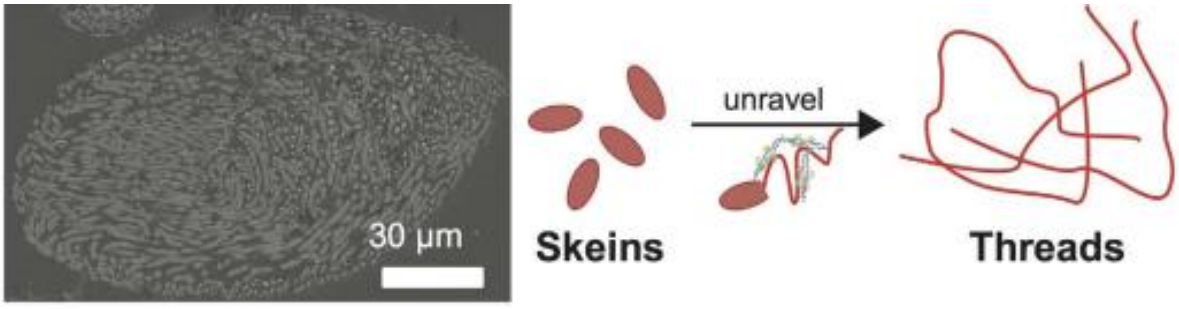

Figure 4.13. Microscope image of skein protein (left) and the cartoon representation of the skein which unravel upon contact with seawater in order to release the protein thread (right)[11]

The same holds for the mucin vesicles. We show in figure 4.14 a microscope image of many vesicles which are stabilized in a buffer solution (stabilization procedure to be explained in section 4.2.2) and the corresponding cartoon which illustrates the swelling of the vesicles and rupture of the mucins outside the vesicle. In the single bilayer membrane there are ion transporters which may allow not only water to enter the vesicle but also ions such as Ca^{2+} [43], [73] . It turns out that these specific ions play a crucial role in the rupture of the vesicles. When ions from seawater enter the membrane they reduce the concentration gradients and they rupture[74].

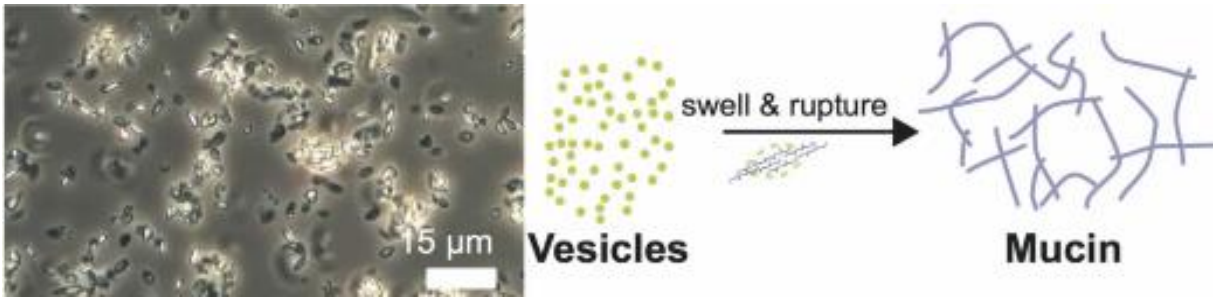

Figure 4.14. Microscope image of mucin vesicles in buffer solution (left) and the cartoon representation of these vesicles where in contact with water they swell and they release the mucin-like glycoproteins in water (right) [11].

Hagfish slime is one of the most promising materials for varying applications and especially in the pharmaceutical sector, as a smart, superelastic, economic and water-absorbing materials. It is characterized as superelastic due to the mucus composition and its cohesiveness due to the long fibers. The rupture of the vesicles and the unravelling of the skeins take place simultaneously in seawater[12]. Figure 4.15 shows the components before interacting with water on the left and after interacting with water on the right.

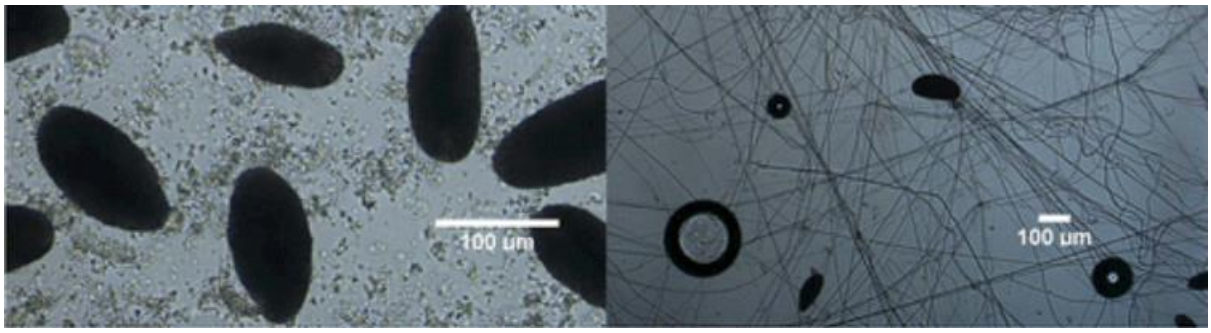

Figure 4.15. Hagfish slime exudate on the left with the two components (skeins and mucin vesicles) and the slimy network (threads and mucins) on the right.

In this work we focus exclusively on isolated mucin vesicles and their composition, i.e., the mucin-like glycoproteins. In the next paragraph we discuss the composition of mucin proteins and some of their unique characteristics with the relevant challenges.

4.2.2. Mucin proteins

Mucin proteins is the major component of hagfish slime. Its own main component of this mucus hydrogel is water which constitutes more that 90-95% of the total mucus

mass[10], [14], [75]. The functional properties of this physical hydrogel originate from the biomacromolecules (mucin proteins) which are responsible for its viscoelasticity [11], [45]. The composition of mucins in the mucus secretion is about 2-5% of the total mass. However, lipids, salts and other proteins are also in presence but with a very small contribution.

The viscoelasticity of this complex system is based on the interactions which are hydrophobic, electrostatic and calcium-mediated [12]. The following schematic (Figure 4.16) illustrates an example of a mucin. There are many types of mucins and the one presented below is named as MUC5AC and found in many living organisms (e.g. nasal cavity)[39].

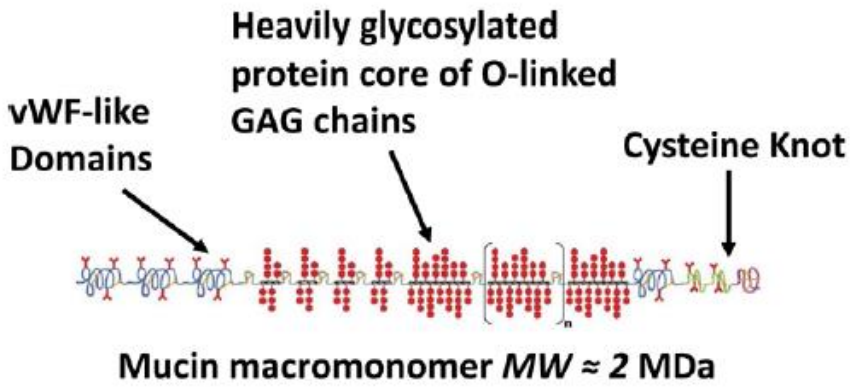

Figure 4.16. Cartoon representation of a mucin macromolecule, coded as MUC5AC, taken from [39].

The main part is the protein backbone which is a polypeptide with oligosaccharides known as glycan side-chains. This central zone is anionic due to the terminal groups which are mainly carboxyl-groups and they provide repulsive electrostatic interactions. The peptide residues (e.g. proline, glycine) provide the hydrophobic interactions in the system. The cysteine-rich domains provide disulfide bonding which provides the linking between the mucin monomers [69], [76]–[78]. In order to present a better understanding of the interactions in the system we show the cartoon below which is taken from [39].

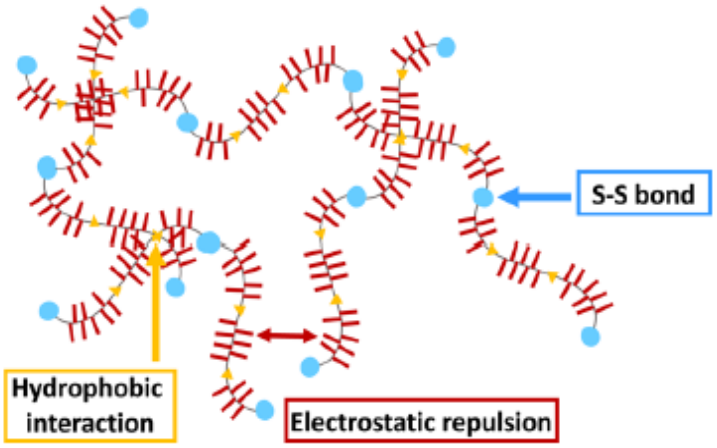

Figure 4.17. Cartoon representation of the interaction for mucin proteins. Hydrophobic interactions dominate between the non-glycosylated groups and electrostatic repulsive between the mucin macromolecules due to the negatively charged backbone. The disulfide bonds are the linkage between the mucin monomers, taken from [39].

When mucins appear at high concentrations they form this highly viscous shear thinning gel due to the combination of entanglements and hydrophobic interactions. The hydrophilic nature of the oligosaccharides and the electrostatic repulsions between the oligomers are the reasons why the gel is in a completely hydrated state and of course explain why mucins exhibit super-absorbance.

The biological nature of mucus with a special interest on mucins is very challenging to understand since the molecular weight of such proteins is very high and unknown; the polydispersity is much larger than synthetic systems and the degree of glycosylation is difficult to determine[77]. All these parameters which strongly affect the final material properties are not easily controlled.

4.2.3. Sample preparation

This paragraph is divided in two parts: i) slime collection and stabilization of mucin vesicles and ii) network formation. In the first part we discuss very briefly the slime collection and the sample stabilization at which mucin vesicles are stabilized in a buffer solution in appropriate conditions. In the second part we discuss the hydrogel formation. The technical issues and handling of such system are briefly reviewed.

i) Slime collection and stabilization of mucin vesicles

Marine hagfish (Myxine glutinosa) was provided by the Atlanterhavsparken in Ålesund, Norway. The procedure performed according to the ethical application by the Forsøksdyrutvalget (FOTS ID 6912), under the supervision of Møreforsking Nyhetsarkiv. In 10L of fresh seawater, a mixture of 1:9 of clove bud oil (Sigma-Aldrich) and ethanol was used for the hagfish anesthetization at a concentration of 1ml/L. After hagfish was anesthetized, it was placed in a dissection board and plotted dry. Once it was dried an electrical stimulation was performed with a stimulation device (HPG1, Velleman Instruments, 80 Hz, 8 -18 V) in order to make the fish to release the exudate. The exudate produced from the hagfish when the stimulus procedure starts.

The exudate comes out of the pores because the electrical stimulus, stimulates the muscles around them. After this, a spatula is used in order to remove the secreted exudate from the ventrolateral place and stabilize in a buffer solution. In particular, the exudate was stabilized in a MCT oil (Medium Chain Triglyceride) or in a high-osmolarity CP buffer consisting of 0.9M sodium citrate and 0.1M PIPES at pH 6.7, 0.02% NaN_3 and a protease inhibitor. Although we refer below to ions from seawater which have the ability to enter the vesicle membrane and it is important to highlight that the high osmolarity buffer (CP) which contains polyvalent ions does not rupture the vesicles. Studies on vesicle membrane were shown that it is impermeable to polyvalent ions [43].

Exudate has to be stabilized in order to retain its functionality over time and its natural composition. Samples were kept in the fridge at 4^{o}C. Finally, hagfish can be recovered in a fresh seawater after sampling. There is a well presented literature work by [11], [12], [43], [79]–[81] about the detailed analysis of the exudate and its stabilization.

ii) Network formation

Fast network formation in few seconds is very exciting in comparison to other gels, usually synthetic, which may take days to fully develop (e.g. gelation of colloidal suspensions). As already mentioned, vesicles are stabilized in a citrate-pipes buffer (CP) and samples care coded as ‘’mucin stock vesicles/stock solution’’. This stock solution is our initial starting point for further sample preparation and analysis. All

samples were prepared in Eppendorf tubes of 2ml volume. The homogenization of the system is critical on every sample preparation. With the micropipette we suspended the vesicles in the buffer and added small amount of this solution (e.g. 5μl) in nanopure water (e.g. 995μl) until the desired concentration (e.g. 0.5vol. %) was reached. Water goes into the vesicles and swells them. In this way the mucin proteins leave the vesicle and create the polyelectrolyte network structure.

The mixing procedure (vesicles and water) is illustrated in the cartoon of figure 4.18 [69]. In the first vial (1) there are vesicles and buffer solution, in the second vial (2) water with the buffer and the vesicles, and in order to create the slimy network (3) we slosh the vial by 8 times. The number 8 is an empirical albeit effective protocol for this kind of sample preparation.

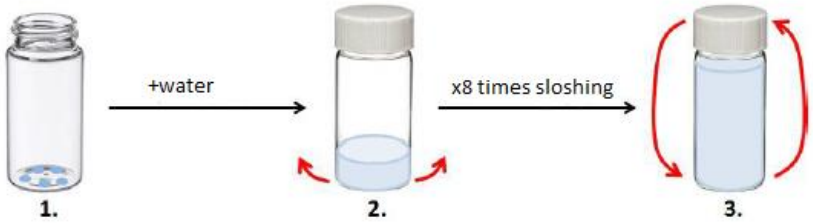

Figure 4.18. Cartoon representation of the mucin network formation. Each number correspond to a single step needed for final hydrogel formation. Especially, #1 vesicles with buffer in a vial, #2 vesicles and buffer with the addition of water and in last but most important step #3 is the mixing of the sample by sloshing the vial up and down for 8 times. The final product is the super elastic network-mucus [69].

Failure of network formation: It is important to highlight this point since it is strongly connected with the health and consequently the functionality of mucus. The single bilayer membrane has the key role on the rupture of the mucin vesicles. When the membrane is fresh, water can enter in and swell the vesicle, but if it is broken or has some damage vesicles cannot swell and consequently they do not release the mucin proteins but they remain packed instead. This is a technical issue since if the vesicles do not swell a heterogeneous structure results, which is not gelly and its properties are ill-defined. In other words, a gelly sample is a healthy sample and vice versa.

It is important to note that salts influence strongly the formation of mucin network and we discuss this in chapters 6 and 7 in the context of dynamic light scattering and

rheology (extensional and shear) experiments. We also discuss examples with different salts such as monovalent (Na^+) and divalent (Ca^{2+}) and present our hypothesis about heterogeneity and the role of ions in electrostatic screening as well as the opening of the vesicles.

4.2.4. Concentration determination of mucins

The concentration of the vesicles is a particularly crucial parameter in such biological systems. The concentration determination was firstly introduced many years ago by [74]. We have firstly to understand what makes this parameter so important but also hard to define. As already mentioned above, when the sample is taken from the fish with the spatula and stabilized in a buffer solution, the quantity taken is unknown because the procedure is random. We do not control the amount of the collected exudate. For this reason, the turbidimetric measurements (UV-Vis) were very useful because they provide the concentration of the solution.

By using calibration curves, we can easily calculate the vesicles concentration for a given stock solution. However, a stock solution can be very dilute if it contains large volume of CP buffer but also very concentrated if it contains low volume of CP buffer. Vesicles are relatively heavy and they sediment after a certain amount of time and in this way we can remove as much buffer as we want from the supernatant and consequently concentrate the stock solution. In figure 4.19, we show a calibration curve from the pioneering work of Salo [74] which allows determining the absolute concentration of mucin vesicles in the buffer solution by measuring their UV absorption.

After each turbidimetric measurement, the solution was dried out in a vacuum oven and the dry mass measured. In this way the calibration curve was built. The calibration curve represents the absorption values in the vertical axis which correspond to the measured solution concentration in the horizontal axis.

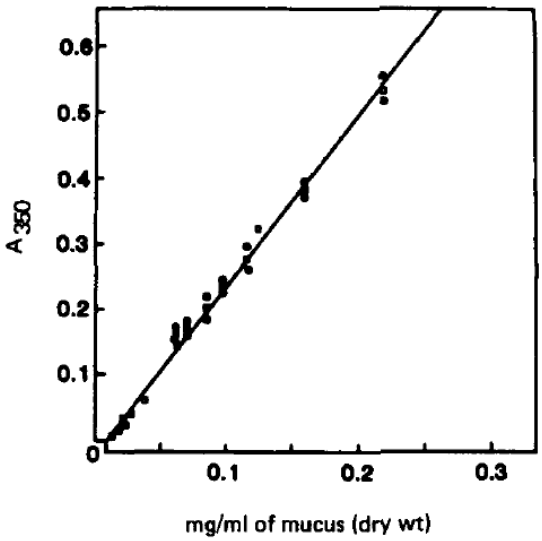

Figure 4.19. Calibration curve from Salo et al. 1983, absorption against mucus dry weight concentration. The 100% of the stock solution corresponds to a concentration of 2mg/ml [74].

The exact protocol was subsequently used from R. Zurflüh [69] in order to build a calibration curve for the same system. In figure 4.20, the vertical axis represents the concentration in volume percent (vol. %) which is the volume of the stabilized vesicles in the buffer solution over the total volume in nanopure water; the horizontal axis is the absorption of the corresponding concentrations. The linear fit gives y=21.238x-0.1528.

The initial starting point was the stock solution, coded as the 100% stock. By measuring the absorption of this sample and its dry mass the vesicles concentration was found to be 2.6 mg/ml.

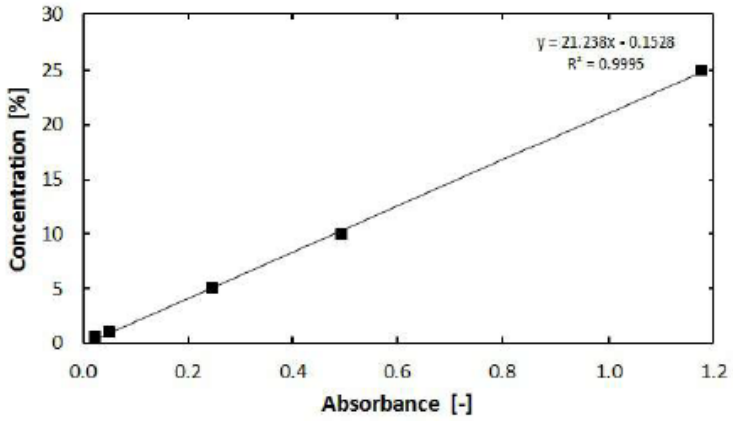

Figure 4.20. Calibration curve of concentration against absorption for mucin stock solution. The 100% (dried) of this mucin proteins correspond to a concentration of 2.6mg/ml. Picture captured from R. Zurflüh [69].

In chapter 3, where we report the methods used, we explain how we calculate via a calibration curve the concentration. Here, we analyze in more detail how this can be done in a simple way by following series of steps.

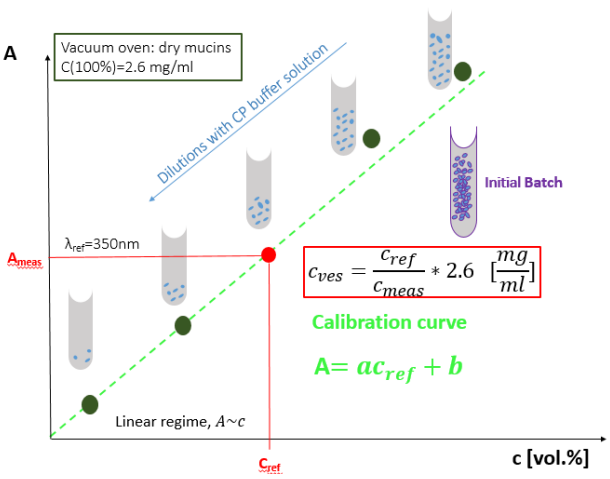

Figure 4.21. Cartoon illustration of the protocol used for the concentration determination of the mucin-like proteins. The vertical axis shows the absorption and the horizontal axis shows the sample concentration in the CP buffer solution. There is the indication of the linear regime and in continues the deviation from the linearity at higher concentrations. In the red box we show the calculation used in order to define the desired concentration (discussed in the text in detail).

For our system three different stock solutions were used. They were stock solutions which contained the same material (mucin vesicles), stabilized in the same buffer but they differed in vesicles concentration. One was dilute, the second more concentrated and the third in an intermediate concentration.

Simplistic protocol:

1) Stock solution mixed properly with the micropipette for system homogenization.
2) In an eppendorf tube small amount of the stock solution was added and the rest of the volume was filled with pure buffer solution (dilution).
3) Three solutions with the same concentration (c_{meas}) were prepared.
4) The absorption was measured for each sample and the standard deviation was calculated.
5) Using the equation given in figure 4.20 for our measured absorptions, we calculated the respective concentrations in vol. % (c_{ref}).
6) The last step was to extract the concentration of the vesicles:

$$c_{vesicles} = \frac{c_{ref}}{c_{meas}} * 2.6 \ (\frac{mg}{ml})$$

Where $c_{vesicles}$ is the concentration on the vesicles in the stock solution which is unknown, c_{ref} is the concentration determined from the calibration curve by using our absorption values, c_{meas} is the concentration which corresponds to the solution

prepared for the turbidimetric measurements and the value of 2.6 mg/ml corresponds to the concentration of the vesicles of the 100% stock solution based on the calibration curve. In the following table we note the final concentration of the mucin stock solutions.

Table 4.2. Coding of mucin stock solutions and the corresponding vesicles concentration determined from UV-Vis measurements for the 100% of the stock solution. Samples B, C and D are estimations based on the first calibration curve of stock solution A.

Stock solutions	$C_{vesicles}$ (mg/ml)
A	2.6
B	11.3
C	40
D	27

Chapter 5: Glass and jamming transition in soft microgels

This chapter focuses on the linear viscoelastic properties of thermoresponsive PNIPAM suspensions. Samples were properly characterized by DLS as described in chapter 4, and their dynamics explored by means of linear and nonlinear viscoelastic measurements.

One important open question: “Can we reach the same mechanical properties in metastable systems by using different paths?” also mentioned in the introduction. Based on the following cartoon (figure 5.1) we can easily understand that the control parameters here are: i) the concentration and ii) the temperature. We address this question by studying liquid-solid transitions at high enough concentrations. This type of transition is the main topic of this chapter, from glass to jam metastable state.

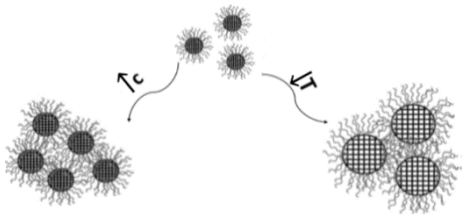

Figure 5.1. Cartoon representation of core-shell particles (core: microgel and shell: linear chains attached to the surface of the particles). Left arrow: concentrated suspension at room temperature and right arrow: less concentrated suspension with swollen particles at temperature lower than the room temperature.

By increasing the concentration at a constant temperature, the system becomes denser and by decreasing the temperature at a constant concentration, system becomes denser as well. While reaching the same effective volume fraction, φ_{eff}, how do we understand about system’s dynamics?

5.1. Sample preparation

Samples were prepared by dissolving a few grams of PNIPAM microgel in nanopure water. The initial concentration was in the dilute regime and by increasing the

amount of PNIPAM we reached the dense regime. In order to prepare highly concentrated solutions it was important to follow a specific protocol. For a well homogenized polymer suspensions, the starting point was a dilute solution (which was kept in the fridge at 4^{o}C, the lower the temperature the larger the swelling capacity of the particles). Once it was properly dissolved, the sample was placed in a hot plate for a couple of days for water evaporation. In the top of the glass vial we put as a cover an aluminium foil with little holes in order to speed up the procedure.

5.2. Rheological measurements

Measurements performed in the strain-controlled rheometer ARES (TA instruments, USA) equipped with a force balance transducer (2KFRTN1). Two different geometries were used for low and high concentrations, respectively. For low concentrations: a stainless steel cone-plate geometry with a diameter of 25mm and cone angle of 0.166rad was used with truncation of 0.21mm. For high concentrations, a stainless steel cone-plate geometry was used with diameter of 8mm and cone-angle of 0.02rad truncation of 0.023mm. The temperature range varied from 15^{o}C to 35^{o}C (from repulsive to attractive region, above the system LCST) and well achieved by means of Peltier element. The thermal expansion coefficient of the plates was 0.3 μm/^{o} C for the smaller geometry and 1.06 μm/^{o} C for the larger one.

The rheological protocol in short was the following: i) first we rejuvenated the system (erase the sample history) with strain sweep experiments at high strain amplitudes, ii) second, we applied a relatively short time sweep (roughly 1000-3000s) in order to reach the steady state regime (system in “equilibrium’) after the rejuvenation, iii) third, we performed a frequency sweep experiment in order to explore the linear viscoelastic spectrum of the suspensions. Step-rate and steady shear experiment were also performed in order to determine the viscosities.

The measuring system investigated in water, which actually evaporates easily and even more at temperatures above 25^{o}C. This is a crucial issue for long-time measurements. For this reason, we developed setups, which are shown below, figure 5.2 is the first approach (a) and figure 5.3 is the second approach (b).

Figure 5.2. Photo of the solvent trap setup (first approach), where in the peltier sample is placed and it is sandwiched with the upper cone-plate. A metal ring is attached to the peltier and in the top of the ring there is a plastic cover. The outer part is a big plastic cover which isolates the sample from the external environment. Cottons in the top (dry) placed in order to improve the isolation and in the bottom (wet) in order to keep the concentration constant.

Figure 5.3. Photo of the solvent trap setup (second approach), where sample is placed in the peltier and the top plate sandwiches the sample. Silicon oil with a medium viscosity (~10mPa.s) filled the surrounding empty space. The goal was to fill until the silicon oil reaches the level of the top plate (not to overfill it).

Both setups were tested and successfully used. The silicon oil procedure is superior since it is much easier to implement, it is rapid in terms of preparation and the sample remains unaffected over long times. In the following two plots (figure 5.4a and 5.4b) we show a frequency sweep example for both procedures after 7h.

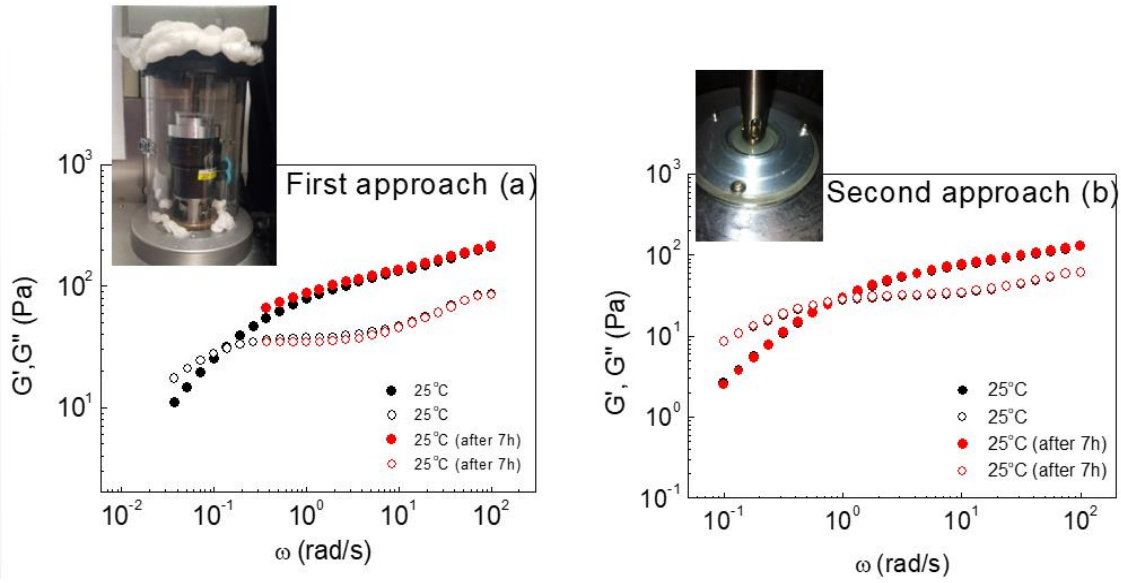

Figure 5.4. Dynamic frequency sweep tests with the two solvent trap setups used. Full symbols correspond to G' and empty symbols to G''. Black data shows the response of the material at 25°C and the red data appear at the same temperature but after all the measurements ~ 7h. The complete match of the data confirms that the protocol approach works. The left graph (a) shows the first procedure and the right graph (b) shows the second setup.

5.3. Nonlinear viscoelasticity of PNIPAM microgels

Dynamic strain sweep experiments were performed at different frequencies in order to probe the linear and the nonlinear viscoelastic regime of the system. The concentrations measured: 4wt. %, 6wt. %, 6.8wt. %, 8.2wt. %, 9wt. %, 10wt. %, 12.3wt. %, 17wt. %. Figure 5.5 depicts four concentrations, which were selected to be shown starting from the dilute to the concentrated regime.

The linear viscoelastic (LVE) region extends up to 10%, whereas for the lowest concentrations is slightly smaller. At low strain amplitudes (SAOS), both the elastic (G') and the viscous (G'') moduli are independent of the applied deformation. At large strain amplitudes (LAOS), deviate from the linearity and the G'' exhibits a non-monotonic behavior, a peak. The apparent elastic modulus decreases and when the viscous part shows the peak system yields to flow and liquid-like behavior dominates. At the crossover G'=G'' the microstructure undergoes a breakdown.

In figure 5.5 system is rejuvenated at ω=1 rad/s, T=20°C in order to melt completely the suspension, hence erase its history. As we can note in the dense regime, figure 5.5 d (17wt. %) the maximum strain applied (300%) is not sufficient to rejuvenate

(G''>G') the system. For some concentrations, different frequencies (0.1rad/s and 10rad/s) were applied. These frequencies correspond to different time scales of the system. At high frequencies the modulus increases and for low applied frequencies it decreases.

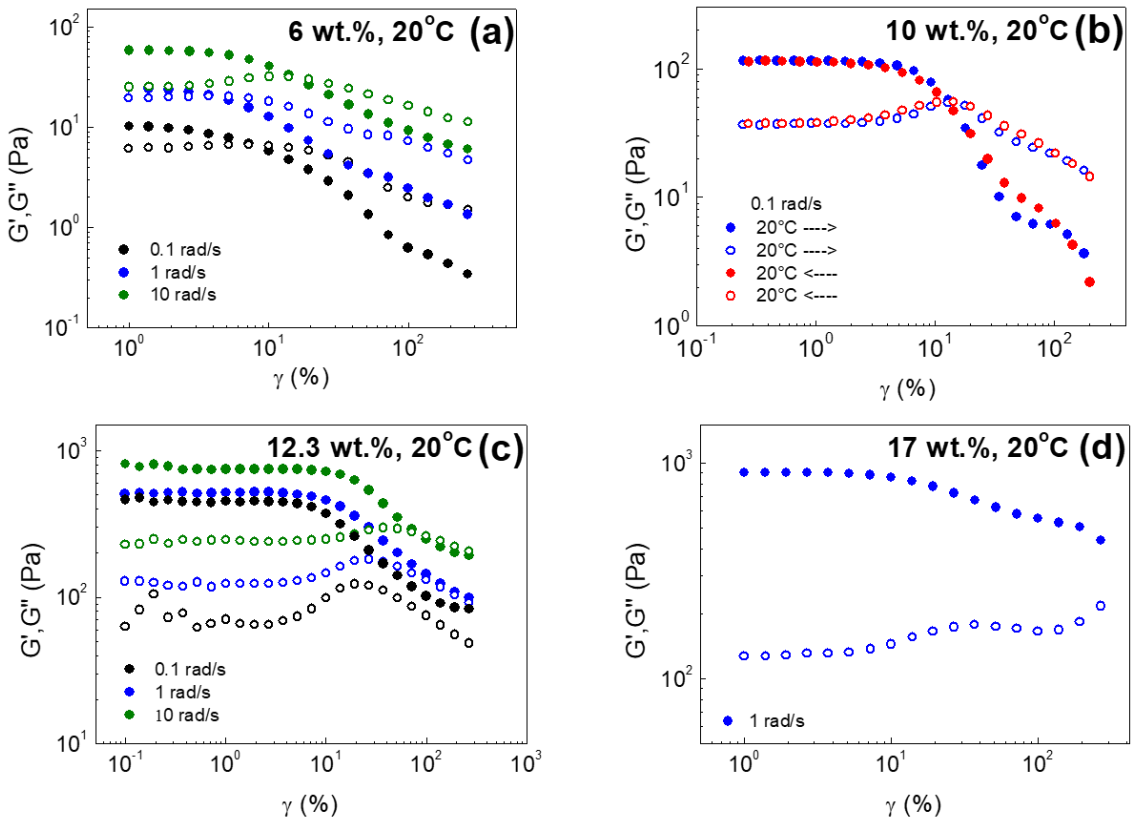

Figure 5.5. Rejuvenation via dynamic strain sweep experiments, elastic (G') and viscous (G'') modulus as a function of strain (γ) on four different concentrations at ω=1rad/s and at T=20°C. Graphs: (a) 6 wt. % at 0.1rad/s, 1rad/s, 10rad/s; (b) 10wt. % at frequency 0.1rad/s; (c) 12.3wt. % at 0.1rad/s, 1rad/s and 10rad/s and (d) 17wt. % at 1rad/s.

Figure 5.6 depicts a dynamic time sweep test for the 6wt. % at 20°C. The strain was chosen in the linear regime, 1% and after a few seconds system was at steady state. Here, after roughly at 1000s we proceeded with measuring the relaxation time spectrum via frequency sweep experiments.

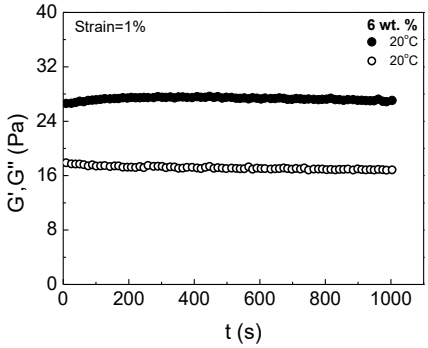

Figure 5.6. System equilibration protocol via dynamic time sweep experiment, elastic (G') and viscous (G'') modulus as a function of time (t) for 6 wt. % at 1% of strain for 20°C.

5.4. Linear viscoelasticity of PNIPAM microgels

A strain amplitude in the LVE regime was chosen, γ_o=1% and frequency sweeps at different temperatures were performed. In the following plots we show the same concentrations as in figure 5.5, at 20ºC. The material is predominantly elastic since G'>G'' (full symbols).

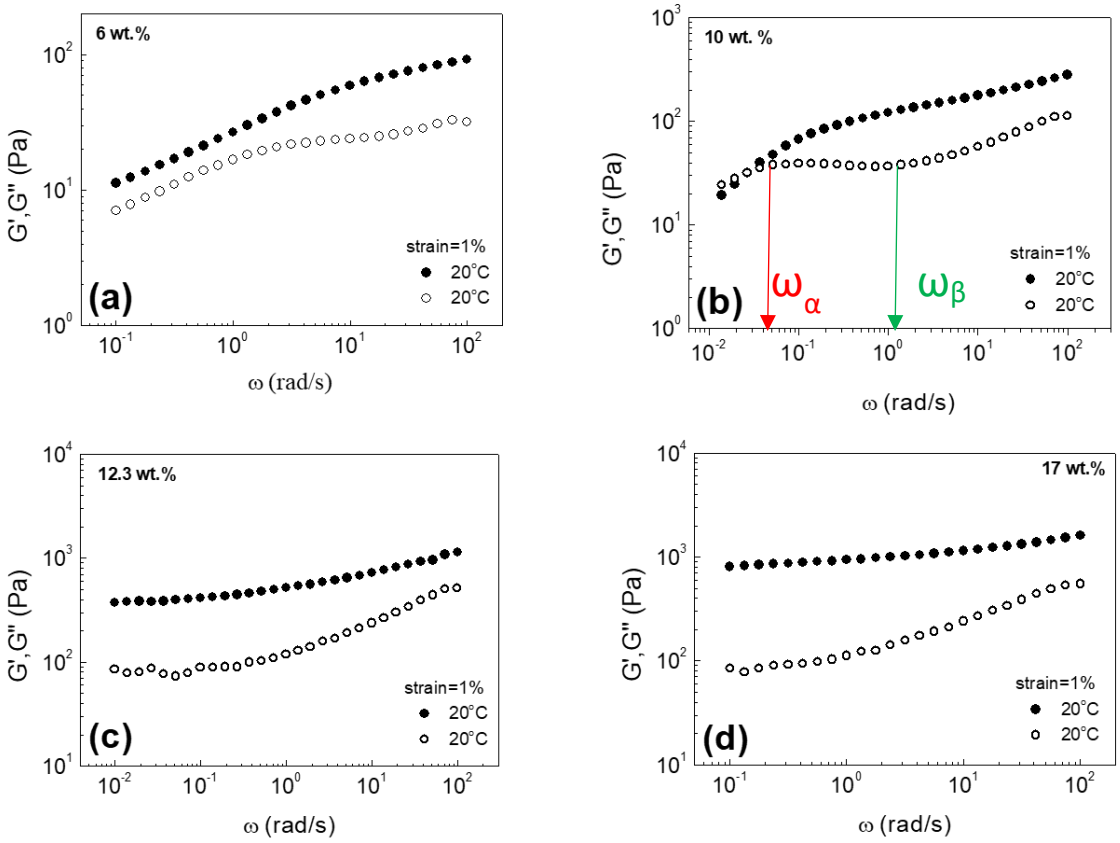

Figure 5.7. Dynamic frequency sweep experiments, (G') and (G") against (ω) for different concentrations at 20ºC at a constant strain of 1%. Graphs: (a) 6wt. %; (b) 10wt. % ;(c) 12.3wt. % and (d) 17wt. %

As already mentioned in the introduction, concentrated soft colloidal suspensions undergo kinetic arrest (glass transition) and particles are caged due to the neighboring particles [82]. Caging is characterized by two different time scales: i) the slow relaxation time, τ_α (α-relaxation) which corresponds to frequency ω_α (or ω_c, the crossover frequency) and indicates the out of cage motion (cage escape) and ii) the fast relaxation time, τ_β (β-relaxation) which corresponds to frequency ω_β and

indicates the in-cage motion. In figure 5.6b, ω_α is the cross-over frequency and ω_β is the frequency at which the G'' exhibits a minimum.

As the concentration increases the size of the cage becomes smaller and the out-of-cage time slower, see figure 5.7d. At lower concentrations, there is a small upturn of the G'' at low frequencies which denotes a terminal possible crossover of G' and G'' (particle escape). At larger strains (in the nonlinear regime) the cage structure is strongly affected from the applied strain and the induced out-of-cage motion becomes faster[83].

In figure 5.8 we show the LVE spectra of the microgel suspensions at a concentration of 10wt. % at different temperatures. At low temperatures 10^{o}C and 15^{o}C moduli are the same due to similar particle sizes. By increasing the temperature, the moduli decrease due to reduction of particle size. Further increase of the temperature, still below the system LCST, weakens the material. Once the suspension reaches T=35^{o}C>T_{LCST} the moduli strongly increase due to particle aggregation and the formed gel's heterogeneities.

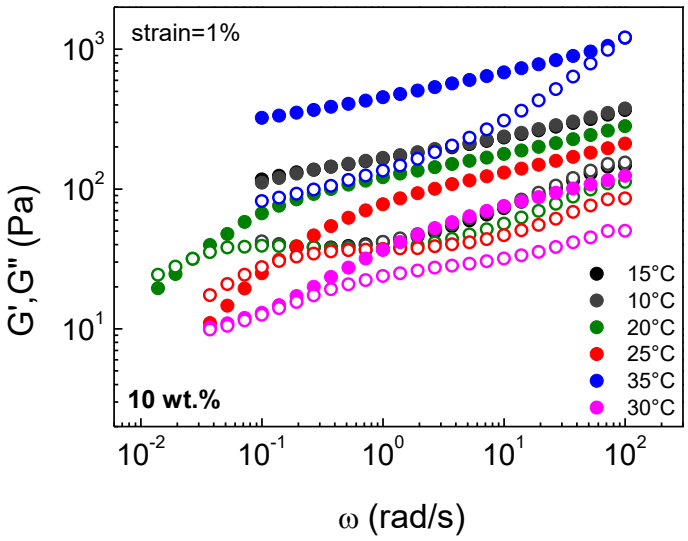

Figure 5.8. Dynamic frequency sweep tests for 10wt. % at different temperatures at strain of 1%. As the temperature increases modulus reduces its value and above the LCST, the moduli strongly increase due particles aggregation.

5.5. Glass and jamming transitions

We can now detect the same mechanical properties by using different mass concentrations at different temperatures but at the effective same volume fraction. In this way, we compare the LVE response with two different paths. The governing expression is: linking concentration and temperature.

$$c_1(T_1)R^3(T_1) = c_2(T_2)R^3(T_2) \qquad \text{Eq.5.1}$$

and it originates from the volume fraction calculation $\varphi = \frac{c}{c^*}$ where $c^* = \frac{3Mw}{4\pi R^3 N_A}$ is the overlap concentration, R is the particle's hydrodynamic radius, M_w is the average molecular weight and N_A is the Avogadro's number ($6.023*10^{23}mol^{-1}$). For our microgels R_H (15°C) = 243nm and R_H (20°C) = 241nm.

In the following graph 5.9a, we show two concentrations at two different temperatures. The higher concentration, 8.2wt. % is measured at 20°C and the lower concentration, 6.8wt. % at 15°C. The higher former exhibits higher moduli and smaller out-of-cage relaxation time. The system at small times appears as weak gel and as time passes it flows. By using a simple normalization factor for both vertical and horizontal axe we reach the same mechanical response. In the y axis of figure 5.9b, the moduli, normalized with the thermal energy per particle which is k_BT/R^3 and the x axis with the a-relaxation time as shown with the arrow in the left plot 5.9a below. This is the: glassy regime[21].

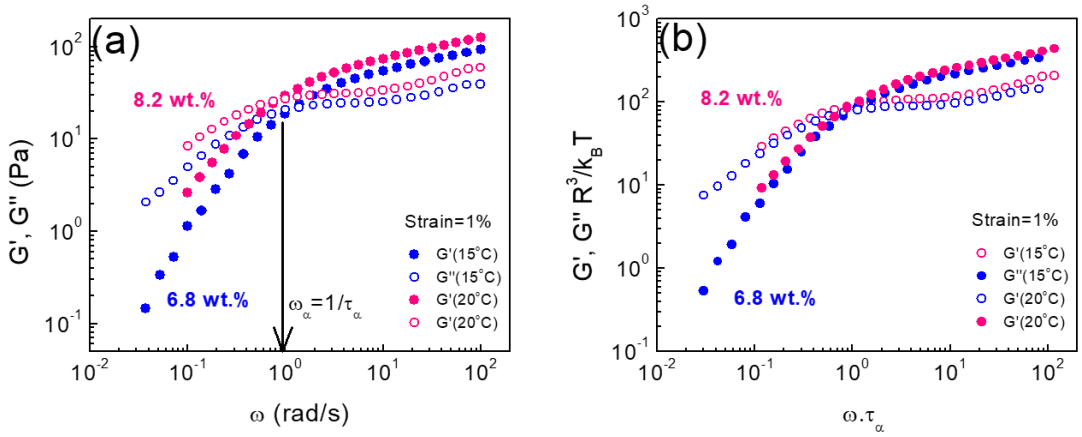

Figure 5.9. (G') and (G'') modulus as a function of (ω) for two different concentrations: 6.8 wt.% at 15°C and 8.2 wt.% at 20°C for strain of 1%. (a) The higher the concentration the higher the moduli; (b) the vertical axis normalized with the thermal energy per particle (R^3/k_BT) and the horizontal axis normalized with the out of cage relaxation time, τ_α. Data after normalization superimpose well.

The same procedure was followed at two higher concentrations for 10wt. % at 15°C and for 12.3wt. % at 20°C. Figure 5.10a shows the solid-like behavior. The characteristic minimum in G'' is the β-relaxation process. Figure 5.10b, the vertical axis normalized in the same way as before and the horizontal axis with the in-cage relaxation time τ_β. In the accessible experimental window, ω_α is not detectable and for this reason we did not use it. This frequency could be reached with theoretical predictions which could provide values of G' and G'' at much longer times, or by means of long-time creep measurements. It is remarkable that the elastic and the viscous moduli which correspond to different concentrations do not collapse as before.

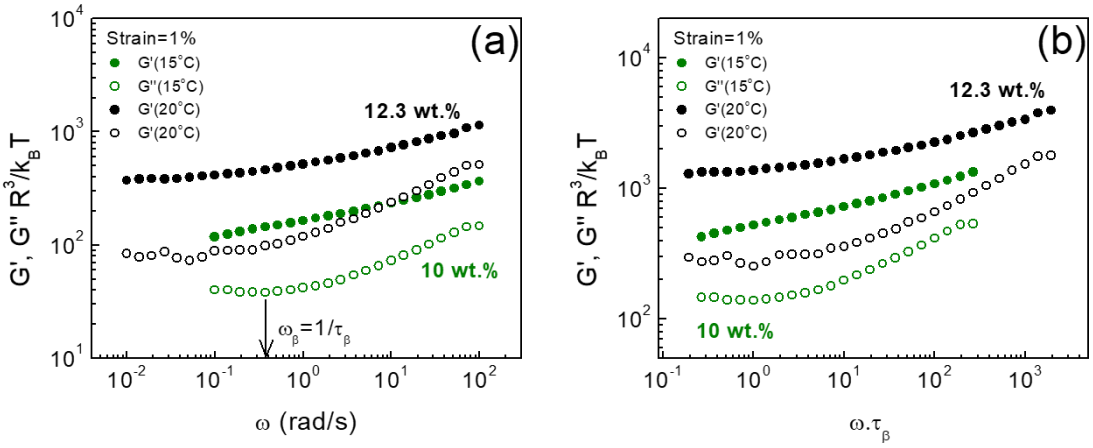

Figure 5.10. (G') and (G'') modulus as a function of (ω) for two different concentrations: 10 wt. % at 15°C and 12.3 wt. % at 20°C for strain of 1%.(a) The higher the concentration the much stronger the material; (b) The vertical axis normalized with the thermal energy per particle (R^3/k_BT) and the horizontal axis normalized with the out of cage relaxation time, τ_β. Data after normalization shifted but they do not match.

In the jamming regime [21], [84], [85] the normalization factor fails because here the particles are deformed and squeezed. Hence it is particle contact rather than thermal motion that dictates their dynamics. It is very challenging at this point to define a shrinkage parameter in order to remove the effect of the reduced size and the particle deformability.

In figure 5.11 we show the concentration at which the transition from glass to jamming state occurs. We compare the elastic plateau modulus and the viscosity as concentration increases. The left vertical axis (G_p) is the plateau modulus from the frequency sweep experiments. This value extracted from G' when the corresponding

G'' exhibits a minimum (values presented in table 5.1). The right vertical axis is the zero-shear viscosity and the horizontal axis shows the range of measured concentrations. It is unambiguous that a transition from low to high concentration regimes take place at 9wt. %.

Table 5.1 Different concentrations with the corresponding plateau modulus estimated from the dynamic frequency sweep tests, G_p=G' when the G'' shows its minimum. Bold concentration marks the jamming transition.

Concentration (wt. %)	ω (G''_{min}) (rad/s)	G_p (Pa)
6.0	0.100	11
6.8	51.00	56
8.2	10.00	74
9.0	**10.00**	**96**
10.0	1.00	121
12.3	0.05	395
17.0	0.30	865

In the glassy regime the particles repel each other and are trapped within a virtual metastable cage as referred above. In this region, the plateau modulus remains relatively constant. As the concentration, increases the modulus starts to deviate and the particles interact with the neighbors by creating contacts (shown in the inset – figure 5.11). Further increase of concentration strongly increases the modulus and this is due to the increase of both the number of contacts and the compression of the particles via osmotic pressure[21]. The linear dependence of G_p with concentration seems to characterize this regime for microgel pastes[21].

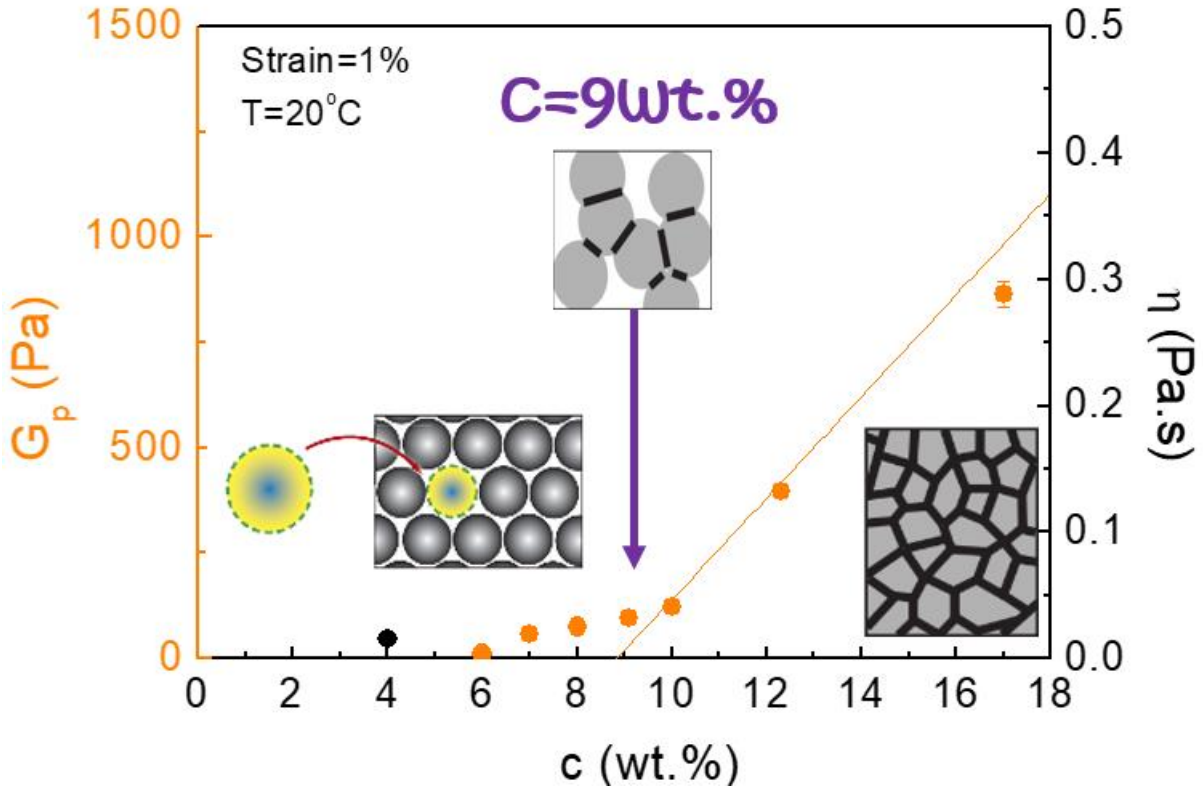

Figure 5.11. Elastic plateau modulus (left axis), blue and viscosity (right axis), black against concentration. Data shown at 20°C and strain 1%. The transition from glass to jamming region occurs at 9wt. %. The insets from left to the right show the structure of an entropic glass with the yellow particle to be "caged" from the neighbors, the transition where particles start to touch each other and create contacts and the very dense regime where particles are compressed and shrinked.

To conclude, we summarize the different regions, starting from the left (low c) to the right (high c):

1) *Very dilute regime* (viscosity measurements, G''>G')
2) *Dilute regime* (G'>G'')
3) Colloidal *glass regime* (amorphous and frozen colloidal suspension)
4) *Transition* from glass to jammed state (particles start to be packed and shape deformation occurs)
5) Colloidal *jamming regime* (particle shrinkage and friction forces dominate due to particle contacts)

A similar phase diagram is built in figure 5.12 where we compare the elastic plateau modulus and the zero shear viscosity, both in normalized form; the first with the modulus G_o=11 Pa (G_o is the plateau modulus a the lowest concentration at reference temperature, 20°C) and latter with viscosity, against polymer concentration

for different temperatures. In the lowest concentration, 4wt. % viscosity measurements performed because the system was liquid with G''>G'.

The key points to be highlighted in this plot are the following: i) at a constant temperature (below the LCST) G' increases with concentration ii) at the highest temperature (35^{o}C) G' at low concentrations (repulsive glassy regime) strongly increases due to the attractive interactions in the system and iii) at high concentrations (jammed glass) the elastic modulus vanishes and viscosity dominates (flow curves measured-shear thinning type of flow).

The latter one can be explained through the system heterogeneities. If we consider a very dense particle suspension where particles are completely packed and attractive interactions dominate then small cavities possibly created and through them the initial system which is melted flows.

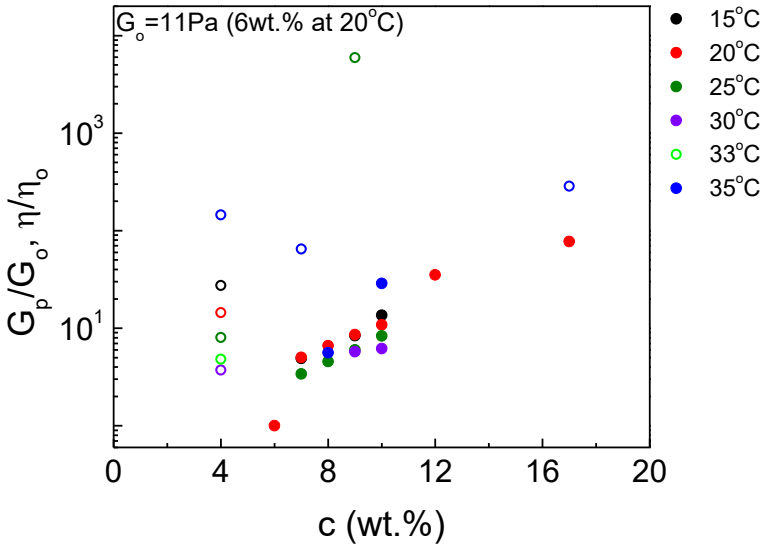

Figure 5.12. Elastic plateau modulus normalized with the lowest modulus (full symbols) at a reference temperature at 20^{o}C and viscosity normalized with the zero shear viscosity (empty symbols) against concentration. Different colors correspond to different temperatures.

5.6. Discussion and summary

The cross-linked PNIPAM particles (2.5wt. %) were first characterized in the dilute regime. The variation of size is a typical behavior of such thermoresponsive (PNIPAM) particles with the transition to take place at 32.5^{o}C.

The effect of mass concentration and temperature were tested in terms of oscillatory shear rheology. The question addressed in the beginning of the present chapter concerns determining the dynamics in systems at the same volume fraction achieved by different means (either with increasing c or reducing the T); this yields the same mechanical properties at relatively lower concentrations (the so-called: glassy regime) whereas at higher concentrations, the system is deformed due to the shrinkage of the particles which is caused due to the osmotic pressure (the so-called: jamming regime). In the following summarize we highlight the major points of this chapter.

i) At concentrations below the transition (9wt. %) the size “controls” (normalization factor) the viscoelastic behavior by including the variation with temperature (figure 5.11). Under these conditions the system reaches terminal crossover and the material flows.

ii) At concentrations above the transition (9wt. %) the size is unknown since particles due to the large concentration are shrinked (figure 5.11). Here, we are not able to reach terminal crossover as in the whole range of frequencies G’>G’’.

iii) Up to 5wt. % the system has an elastic-like response since G’>G’’.

iv) The increase of temperature reduces the size and this causes a decrease in the modulus; above 32.5^{o}C the colloidal suspension undergoes a transition and becomes attractive. First, we detect this from the light scattering characterization (R_H against temperature) in figure 4.6 and from rheology in figure 5.8 where the modulus has a rapid increase at 35^{o}C (strong aggregation results in such stiffening of the network).

Chapter 6: Structure of hagfish mucins

This chapter focuses on the investigation of the dynamic structure of mucin-like protein via dynamic light scattering, DLS. We studied different concentrations of mucins in a salt-free environment, in nanopure water, at 20^{o}C. The main goal was to decode the complex multi-mode dynamics and determine the size of such proteins. To this end, we used different data analysis strategies. Additional measurements were performed in a saline environment and we shall discuss the influence of salt at some of the concentrations.

6.1 Interpretation of light scattering data

The system characterization starts in the very dilute regime, where particles/macromolecules supposed to be isolated. The hydrodynamic size is calculated from the Stokes-Einstein-Sutherland equation (eq. 3.7). In this case, we assumed that the mucin-like glycoprotein is a hypothetical sphere which diffuses freely. Higher concentrations were investigated as well, around and beyond the entanglement concentration. The measured time autocorrelation functions of the scattered intensity were analyzed by three common techniques: i) a regularization method known as CONTIN algorithm[86]; ii) a cumulant method based on Taylor series[2] and iii) a non-linear cumulant analysis[88]. In the next two paragraphs, we present a brief introduction, theoretical background, comparison and some examples.

6.1.1. Basics of CONTIN analysis

The CONTIN method is also termed as non-monomodal distribution method; because it typically involves analysis of multi-mode distribution[48]. In order to gain information about the particle/macromolecule distribution we need to determine the distribution function of the measured decay rate, G(Γ). The electric field correlation function $g_1(\tau)$, measured in DLS experiments, is obtained by Laplace transform of G(Γ):

$$g_1(\tau) = \int_0^\infty G(\Gamma) e^{-\Gamma\tau}\, d\Gamma \qquad \text{Eq.6.1}$$

Where, Γ is the decay rate and τ is the relaxation time (or delay time) of the measured object. The relation between these two parameters, $g_1(\tau)$ and $G(\Gamma)$ is not trivial. The decay rate distribution is given by $G(\Gamma) = \sum_k a_k G_k(\Gamma)$, i.e., a summation of several exponential decay functions that decay at different rates; this is the main reason why CONTIN is particularly useful for highly polydisperse systems.

The main point is to use CONTIN and to invert the decay rate distribution for different values of α which is the so-called regularization parameter. Larger values of α translated into a large residual normalization, whereas smaller values signal larger side constrains and broader distribution (i.e. more modes due aggregations). The quality of fitting depends on the curvature of the distribution. The proper selection of α is a very difficult task because the very tiny differences in the selection of α changes dramatically the result.

In figure 6.1 below we show a typical example (at low concentration, c=0.156mg/ml and a scattering angle of $\theta=75^o$, $q=0.01915nm^{-1}$) of a correlation function analyzed with CONTIN. The red fitting line is the result of the CONTIN algorithm which indicates mainly one relaxation time where the peak appears. The green line in the bottom (baseline) is the so-called residuals and it provides information about the fitting quality. The smother the residual line the better the data treatment.

The inset represents the normalized distribution function against the logarithm of the time. The distribution function is normalized by the corresponding average scattering intensity and the solvent intensity (here toluene) for each angle as:

$$Normalized\ Distribution = \frac{I_{av} * G(\Gamma) * \sin(\theta)}{I_{toluene}} \qquad \text{Eq.6.2}$$

Where I_{av} is the average scattering intensity (raw intensity), $I_{toluene}$ the intensity of the solvent (toluene) and the G(Γ) is the distribution obtained by CONTIN.

The distribution of eq. 6.2 was fitted with a Gaussian function (eq. 6.3, below) for one or more peaks, depending on the concentration and the system polydispersity.

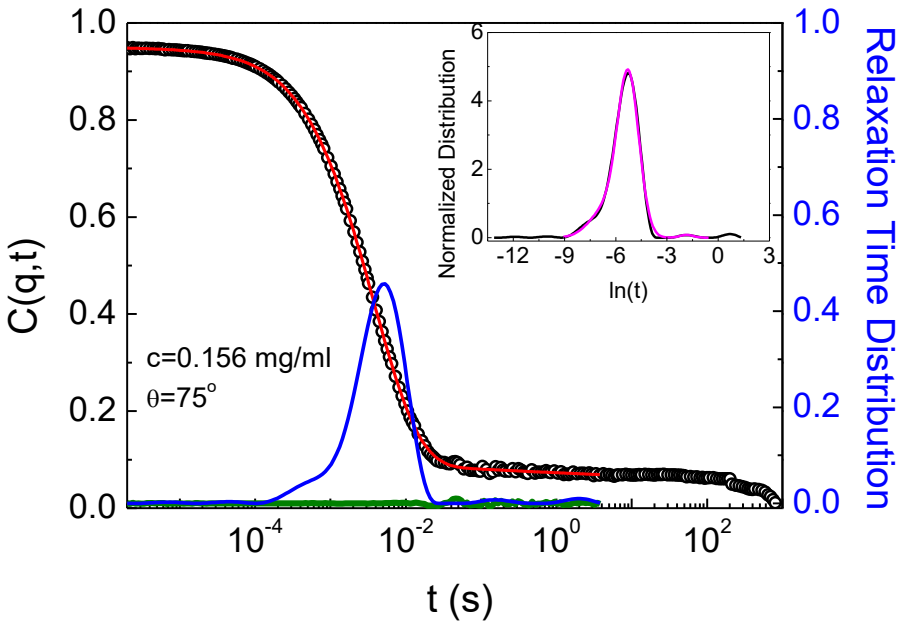

Figure 6.1. Typical example of a correlation function analyzed with CONTIN regularization method. The red curve indicates the fitting of the data and the blue distribution curve represents the size distribution. Inset: we show the normalized distribution against the logarithm of time. The Gaussian fitting of the present distribution provide information about the relaxation time of the measured object.

$$y = y_o + \frac{A}{w\sqrt{\frac{\pi}{2}}} e^{-\frac{2(x-x_c)^2}{w^2}} \qquad \text{Eq. 6.3}$$

Where y_o is the offset, A is the area under the peak, w is the width and x_c is the value of the x axis at the center of the peak. The relaxation time used is a fit parameter $x_c=\tau$.

Normalized scattering intensity:

The scattering intensity is extracted from the normalized distribution function. By applying the Gaussian fitting, the area under the peak corresponds to the normalized scattering intensity. A typical example of its q-dependence is shown in the figure 6.2 below. This power-law dependence is characterized by an exponent (slope) of about -3. The slope indicates the value of the dimensionless parameter d_f (the fractal dimension). As provided by table 3.2 discussed in chapter 3 the topology under investigation seems to be a 3D object with fractal or smooth surfaces.

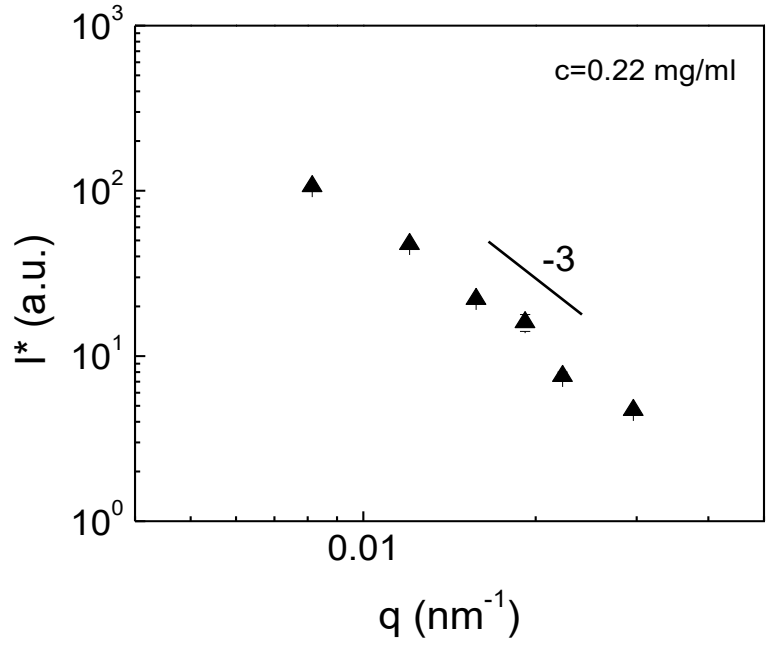

Figure 6.2. Normalized (dynamic) scattering intensity for a concentration of c=0.22mg/ml.

6.1.2. Basics of cumulant analysis

Cumulant analysis it is also known as a monomodal distribution. It is a quantitative, easy and reliable way to calculate the average diffusion coefficient. It is based on a series expansion and it is valid for relatively low polydispersities. The error in the measured quantities, say hydrodynamic radius $\mathrm{R_H}$, has to be $\frac{\Delta \mathrm{R_H}}{R_H} \leq 20\%$. The pioneering work of Koppel et al. introduced the idea of cumulants [87]. The relevant equation is $K(-\tau, \Gamma) = lng_1(\tau)$, which is analyzed in Taylor expansion series as:

$$K(-\tau, \Gamma) = lng_1(\tau) = \sum_{m=1}^{\infty} \frac{k_m}{m!}(-\tau)^m = -k_1\tau + \frac{k_2}{2!}\tau^2 - \frac{k_3}{3!}\ \tau^3 + \cdots \qquad \text{Eq.6.4}$$

where

-k_1 is the first cumulant which yields the diffusion coefficient D_s and is given by $k_1 = < D_s > q^2$. This method provides mean values for the diffusion coefficient and not the decay distribution.

-k_2 is the second cumulant which provides information about the polydispersity of the system due to the diffusion coefficient distribution function $\sigma_D = \frac{\sqrt{(<D_s^2> - <D_s>^2)}}{<D_s>} = \sqrt{\frac{k_2}{k_1^2}}$.

It is defined as

$k_2 = (< D_s^2 > - < D_s >^2) q^4$.

-Higher order cumulants such as k_3 are typically not needed[89].

In figure 6.3 we show a correlation function of a very dilute solution (c=0.08mg/ml) at a scattering angle of θ=75° (q=0.01915nm^{-1}). Figure 6.3a depicts a typical autocorrelation function (lin-log representation). The dashed line represents the region where the exponential decay exhibits its initial slope. The biggest advantage of cumulant analysis is that we avoid the presence of aggregates/clusters which provide a very large slow mode at longer times(the polyelectrolyte effect [32], [33]). For this reason, this method is required mainly for the definition of the fast modes. This is also the reason for which we term this method as a monomodal distribution. However the "length" at which we apply the fit is very small in comparison to other analysis strategies. This can be easily understood by considering figure 6.3b which depicts the autocorrelation function as function of time in a log-lin representation. It shows the very short fitting region associated with the initial slope (dashed region in figure 6.3a). The target is to detect this slope in the correlation function in order to extract a trustable and reliable value for the diffusion coefficient.

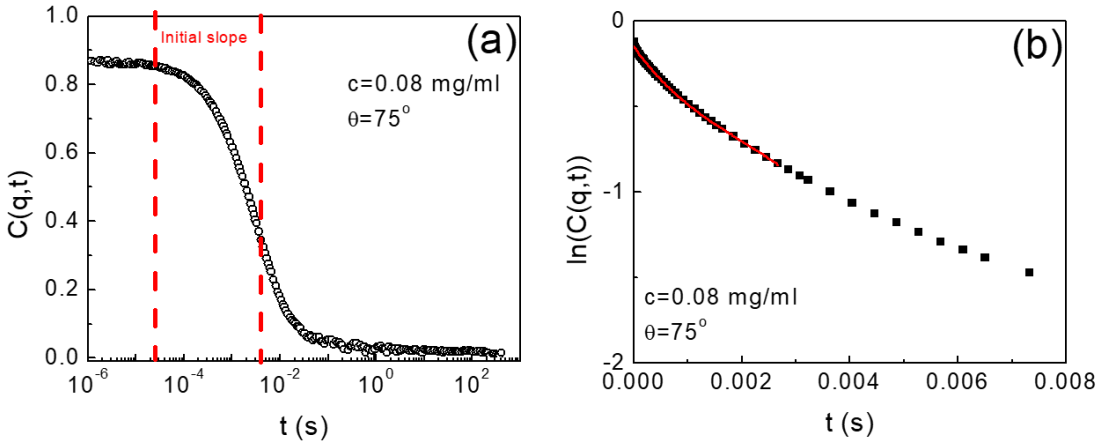

Figure 6.3. Low concentration of mucus, 0.08mg/ml at 75°: (a) we show a lin-log representation of the correlation function with the dashed lines to note the initial slope of the exponential decay; (b) we show a log-lin representation of the correlation function where the fitting line is the triple polynomial fitting of the data.

The data were fitted with a triple polynomial equation, eq. 6.5. Below, we explain in brief the exact steps followed for the estimation of the mucus diffusion.

$$y = A + Bx + Cx^2 + Dx^3 \qquad \text{Eq.6.5}$$

Here, A is the intercept, B is the first cumulant (k_1), C is the second cumulant (k_2) and D is the third cumulant (k_3). For each concentration, five different fits were performed in order to obtain good statistics. The average value of k_1 with its standard deviation were further used for extracting the average value of the diffusion coefficient, $\langle D_s \rangle = k_1/q^2$. In this work, we focus on the first cumulant.

Normalized scattering intensity:

The scattering intensity values normalized with the toluene intensity for the low concentration of c=0.08mg/ml are shown as functions of the scattering wavevector q in figure 6.4. The power-law slope is -3, 3D fractal of smooth surfaces as mentioned in figure 6.2 from CONTIN analysis.

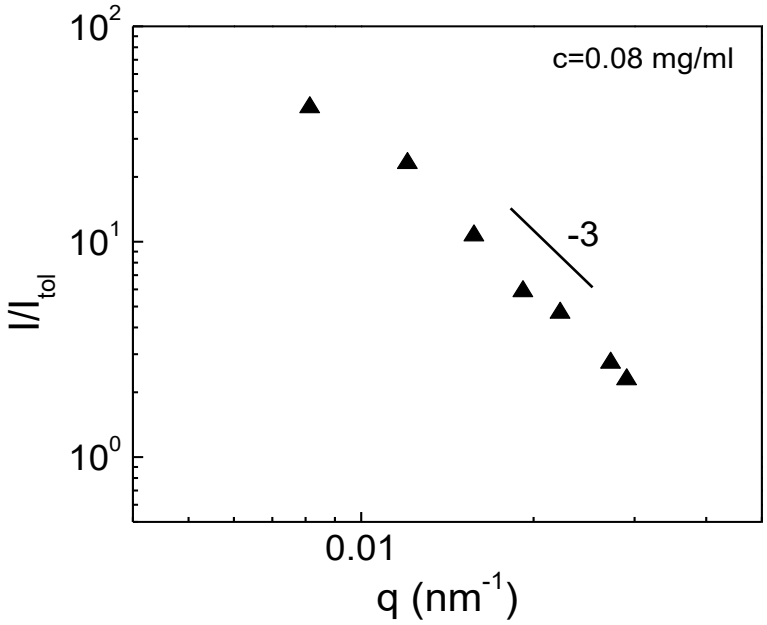

Figure 6.4. Normalized (dynamic) scattering intensity against scattering wavevector for concentration of 0.08mg/ml.

Table 6.1.Summarizes the main features of CONTIN and the cumulant methods of analysis.

CONTIN (Provenquer, 1982)	**Cumulant (Koppel et al., 1972)**
Distribution function of *Γ, τ, D*	Average values of diffusion, $<D_s>$
PDI>0.7 (broad polydispersity index)	PDI<0.7(narrow polydispersity index)
Contribution of all modes (decay rates)-large fitting region	Contribution of fast modes (e.g. avoid the presence of aggregates; the slow modes)-small fitting region

6.1.2.1. Nonlinear cumulant analysis (NLCA)

The third method tested is the so-called nonlinear cumulant analysis (NLCA). Based on the work of Mailer et. al., the third moment cumulant was used (equation 6.4) had no justification. On the other hand, the non-linear fitting procedure of equation 6.6 is very stable in respect to the values of the fitted parameters. NLCA has many advantages in comparison to the linear cumulant analysis and or CONTIN (paragraph 6.1.1) and cumulant analysis (paragraph 6.1.2). The following equation explained as a more robust procedure as well explained from Mailer et al. The non-linear fit is:

$$g_2(\tau) = B + \beta\left\{\exp(\bar{\Gamma}\tau)\left[1 + \frac{1}{2}\mu_2\tau^2 - \frac{1}{3!}\mu_3\tau^3 + \frac{1}{4!}\mu_4\tau^4 - \cdots\right]\right\}^2 \qquad \text{Eq.6.6}$$

where the baseline B is 1 for ideal conditions, μ_2, μ_3 etc. represent the order of cumulants with μ_2 being the second cumulant.

Results in figures 6.10, 6.11, 6.12, 6.13, 6.14, 6.15, 6.18, 6.19 are the ultimate results based on equation 6.6. In the appendix II, we show an example of the fitting curve based on equation 6.6. and we illustrate all the existing data on the apparent diffusion coefficient and intensity profile.

6.1.3. Polydispersity and slow modes

The investigated mucus exhibits a very broad distribution of relaxation times (see also detailed discussion below). This can be quantified with the PDI (polydispersity index), which is defined as the square of the standard deviation of the polydispersity over its mean value within such cases, the CONTIN analysis is necessary. We note that mucins are charged biopolymers (with sulfonate groups) and this provides a big

slow mode, which is characteristic of polyelectrolyte systems independently of concentration. Aggregation due to inter- or intra-mucin interactions provide additional slow mode(s). The slow relaxation due to clusters is more pronounced at higher concentrations. For this reason, cumulant analysis used where there is the need to avoid the contribution of the slow mode.

We discuss the analysis of a relatively low concentration, c=0.22mg/ml. CONTIN results are shown in figure 6.5 with the time autocorrelation functions at different scattering angles in figure 6.5a and the corresponding distributions of relaxation times in figure 6.5b. For each angle, we show the distribution where there is a characteristic peak (assigned to the relaxation time). For each angle the measuring time in the instrument was up to 1000s. The distribution is fitted with a Gaussian function for each peak. The main peak is used for extracting the diffusion coefficient.

In addition one can observe the fast mode (shown in figure 6.5b as a shoulder on the left side of the distribution) and the slow mode (indicated in figure6.5b as a second peak or a shoulder on the right side of the distribution). The fast mode, describes the motion of smaller particles (i.e. DNA, lipids, proteins and cells as mucus components).Counterions have typical rates which are ultra-fast (~10^{-6}s) in respect to [32]; whereas in case of figure 6.5 and 6.1 the fast diffusion seems to be at (~$5*10^{-4}$s). For these roughly two decades difference, we do not believe that this first peak corresponds to the movement of ions presented in the solution. The slow mode is the motion of mucin aggregates.

The slow relaxation process is complex, depends on many factors (interactions, system, sample treatment during solvent evaporation to increase concentration) and as a result it is uncontrollable, hence it will not be further investigated. Example of the strong slow mode presented in figure 6.8 below (yellow box at large times).

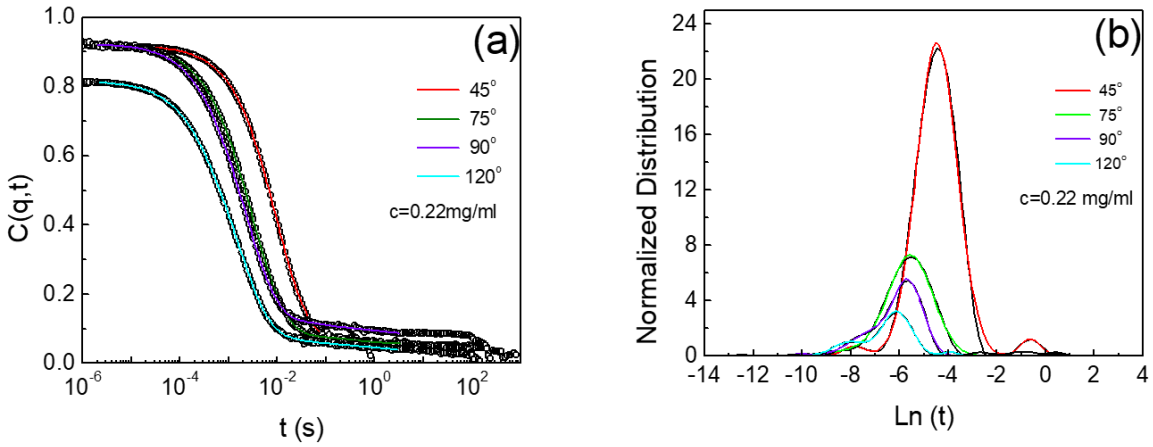

Figure 6.5. (a) Correlation function of a low concentration of 0.22mg/ml at four different scattering angles. The fitting curves provided by CONTIN; (b): Normalized distribution function fitted with a Gauss equation.

In figure 6.6 we compare results from the CONTIN analysis (figure6.6a) and the cumulant analysis (figure 6.6b). In the graphs: the term “low concentration” refers to the beginning of entanglement regime whereas the term “high concentration” refers to a concentration deep in the entanglement regime. The values of the apparent diffusion coefficient and consequently the hydrodynamic radii are very similar: 375nm (CONTIN) and 396nm (cumulant). However, we can note the q-dependence of mucin diffusion which is a signature of a polydisperse sample. Nevertheless, we found that <u>at low concentrations the different interpretation methods show similar results.</u>

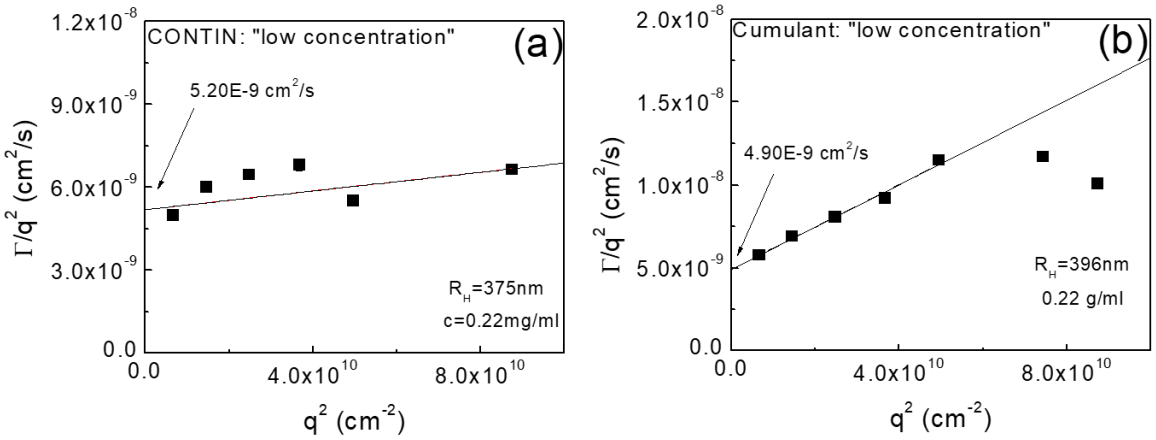

Figure 6.6. Apparent diffusion coefficient (Γ/q^2) against q^2: (a): CONTIN analysis and the size calculated is 375nm; (b): Cumulant analysis and the size calculated is 396nm.

The same comparison was performed at a higher concentration, c=0.9mg/ml and the results are now briefly discussed. In figure 6.7 we depict the time-autocorrelation functions (figure 6.7a) and their corresponding distribution (figure 6.7b). We observe that the slow mode is much greater and there is absence of baseline. For each angle, the measuring time in the instrument was up to 2000s. More than one random peaks appear in the distribution, which do not show any consistent trend with the scattering angle, in contrast to the lower concentration (figure 6.5b).

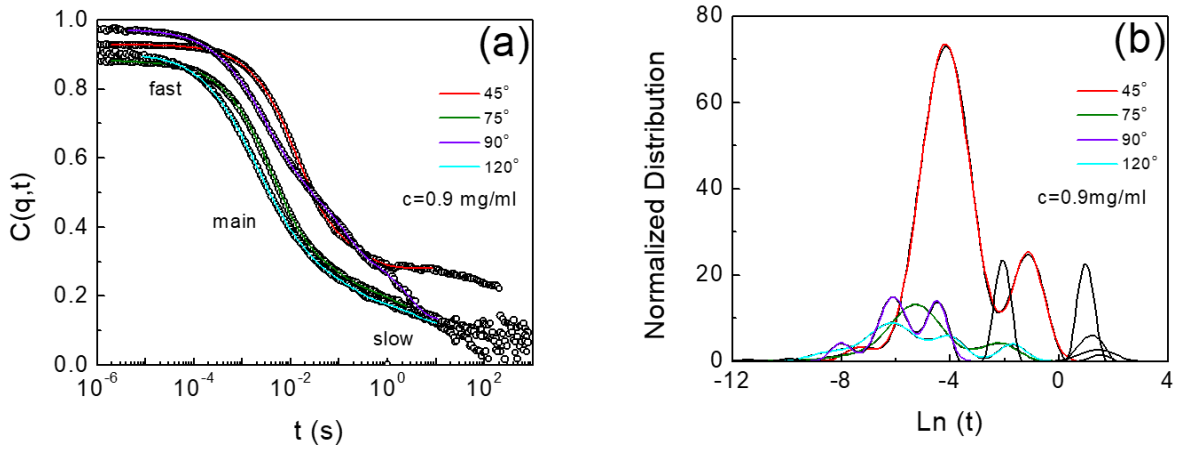

Figure 6.7. (a) Correlation function of higher concentration, 0.9mg/ml at four different scattering angles. The fitting curves provided by CONTIN; (b) Normalized distribution function fitted with a Gauss equation.

Figure 6.8a depicts the results of the CONTIN analysis and figure 6.8b the respective results of the cumulant analysis. In this case of higher concentration, CONTIN fails (the dashed box in figure 6.8a shows how scattered the data are). The values of the apparent diffusion coefficient and consequently the hydrodynamic size (which at this concentration is a correlation length rather than single mucin size) differ: 1000nm (CONTIN) and 552nm (cumulant). We found in general that at high concentrations the different analysis methods show different result. This can be appreciated by means of the analysis with the CONTIN algorithm (which is an ill-posed inversion problem). The increase of Γ/q^2 versus q^2 signs the presence of large and polydisperse objects in the solution, even if the increase is relatively smooth (figure 6.8b).

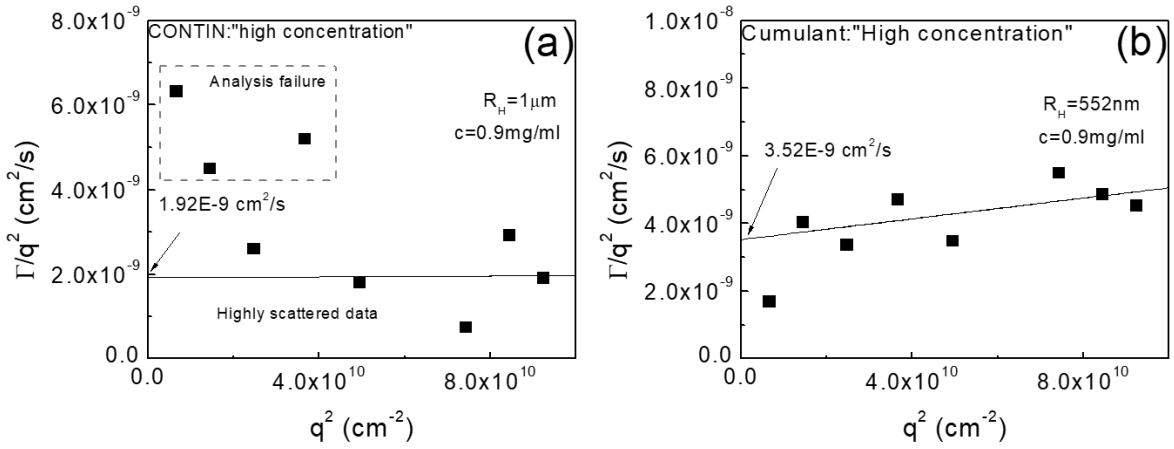

Figure 6.8. Apparent diffusion coefficient (Γ/q^2) against q^2: (a) CONTIN analysis and the size calculated is 1000nm; (b) Cumulant analysis and the size calculated is 552nm.

The effect of concentration on the slow mode is appreciated by observing the changing shape of the correlation function, as typically seen in figure 6.9. As the concentration increases from very low to intermediate and finally very high, the slow mode increases. This is also an evidence that at low concentration where the (relative weak) slow mode is present due to the polyelectrolyte effect, both CONTIN and the cumulant work equally well and give virtually the same results. At higher concentrations where the slow mode is much larger, CONTIN fails and cumulant provides information only on the faster dynamic process. At this point, it is important to note that the presence of the slow modes can be measured more accurately with the multi-speckle dynamic light scattering (MSDLS) technique [90].

Failure of CONTIN: the slope of -3 shown in figure 6.4 signs the presence of possible scattering from surfaces [50]. Thus surfaces in addition to internal modes within polymer network at large concentrations strongly influence the distribution function. For this reason, CONTIN at high concentrations gives a solution with many peaks originated from the complexes being in the system. In comparison to low concentrations where aggregates are less and slow mode is smoother. Cumulant "success": this is due to the proper collection of the initial slope which has the consequence of including only modes at short times.

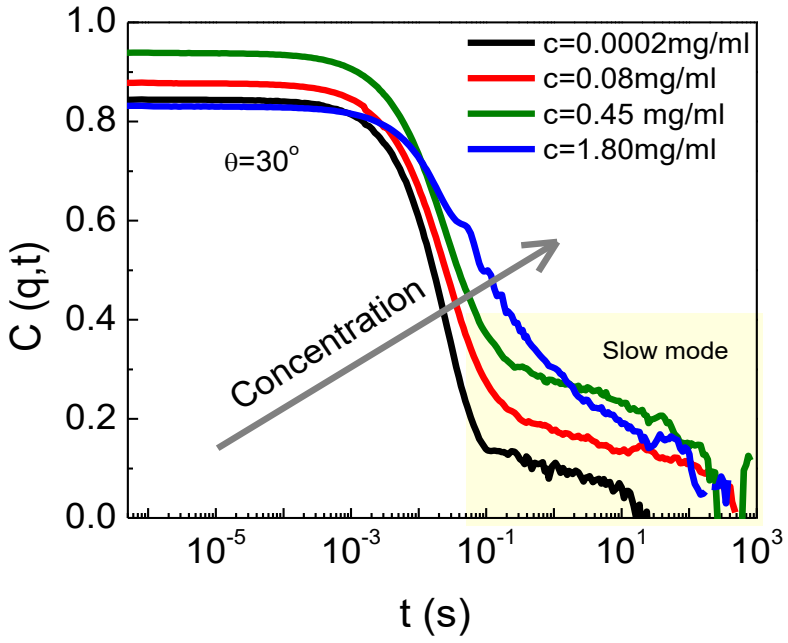

Figure 6.9. Correlation functions at 30° for different concentrations of mucins with the slow mode at long times (yellow box).

Intensity profile:

For all measured concentrations the power-law slope of I(q) is -3. The intensity profiles do not include the plateau region (Guinier plateau) at low q. Mucin proteins are very large and in order to explore the low-q region we need the small-angle light scattering (SALS) which is challenging for further investigations. In our setup the lowest angle used is θ=25° (q=0.00681nm^{-1}) whereas for SALS the minimum measurement can be done at θ=5° (q=0.00137nm^{-1}). Hence, the maximum angle used is θ=150° (q=0.03039nm^{-1}) whereas for SALS the maximum measurement can be done at θ=25° (q=0.00681nm^{-1}).Note that we measured, some static intensities via static light scattering (SLS) and they confirm the slope of -3. The range of angles we measured in SLS is: 25°<θ<150° with step of θ=5° for t=10s in each angle. The protocol applied three times. Hereafter, we shall concentrate on the dynamic intensities and properties.

6.2 Diffusion dynamics and scattering intensity in salt-free environment

In this section, we address the dynamic microstructure of mucins at different concentrations. For each one, the apparent diffusion coefficient was obtained (via CONTIN, cumulant and NLCA) and normalized with the apparent diffusion coefficient which corresponds to the lowest measured concentration, c→0 (limit of zero concentration). In figure 6.10 all presented data are originated from the NLCA analysis. The ratio was plotted against concentration in order to define the onset concentration for interactions (considering them only in the presence of interaction the diffusion coefficient becomes concentration dependent). This onset concentration marks the beginning of the entanglement regime (region III). For polyelectrolytes, the dilute (region I) and the semidilute regime (region II) cover many decades of concentrations [29].

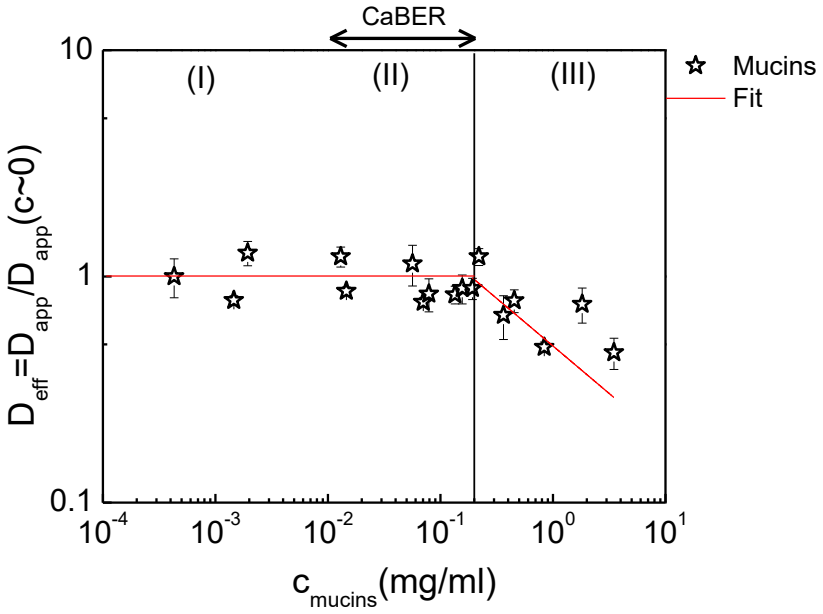

Figure 6.10. Apparent diffusion coefficient normalized with the apparent diffusion coefficient when c→0 against mucin concentration for different batches: A, B and D.

As the concentration increases, the diffusion remains constant (for roughly three decades in time). This is expected since we deal with polyelectrolytes. The vertical line indicates the concentration of c=0.2mg/ml which marks the onset of concentration-dependent diffusion. Different batches contain the same material (mucin vesicles in stock CP buffer solutions) and the difference between them is the

amount of vesicles ($c_{vesicles}$). The protocol for their concentration determination is discussed in chapter 4, paragraph 4.2.3.

In the following table we summarize some characteristic mucus concentrations. The c (entanglement) is the concentration where mucins make entanglements. The c (reference) is the concentration which was chosen as reference in order to study the effect of salt. The c (dilute) is the lowest concentration measured in light scattering and c (slime) is the natural concentration of hagfish slime where mucins and threads coincides.

Table 6.2. Characteristic values of mucin concentrations.

code	**concentration (mg/ml)**
c (entanglement), c_e	0.2
c (reference)	0.08
c (dilute)=c_o	0.0002
c (slime)	0.02

The concentration dependence of the diffusion coefficient (*$D \sim c^0$ in the dilute and the semidilute unentangled and $D \sim c^{-0.5}$ for the entanglement regime*[29]) is consistent with observations reported in the literature. As mentioned in chapter 2, for polyelectrolyte solutions in a salt-free environment the slowing-down of the diffusion above the entanglement concentration follows a $c^{-0.5}$ dependence [29]. However, the work of M. Sedlák and E.J. Amis [32]reported different scaling of $c^{-0.8}$ and $c^{-0.35}$ for a high molecular weight polyelectrolyte and two distinct concentration regimes.

A clear concentration dependence was also followed by the intensity. We plot the reduced intensity, i.e., the intensity when $q \rightarrow 0$ over the concentration, against mucin concentration. At low and intermediate concentrations, the intensity is independent of concentration, but at c_e=0.2mg/ml it decreases. This cross-over concentration which corresponds to the entanglement concentration c_e is very well in agreement for both dynamic (diffusion in figure 6.10) and static properties (intensity in figure 6.11). The diffusion dynamics as well as the intensity profile provided from DLS.

In the previous paragraph, we explained that we cannot extract the low-q region, which means that we do not know an exact determination of $I_o(q\rightarrow 0)$ value. For this reason, we explain in figure 6.12 how we extract $I_o(q\rightarrow 0)$ by means of the Debye plot [91].

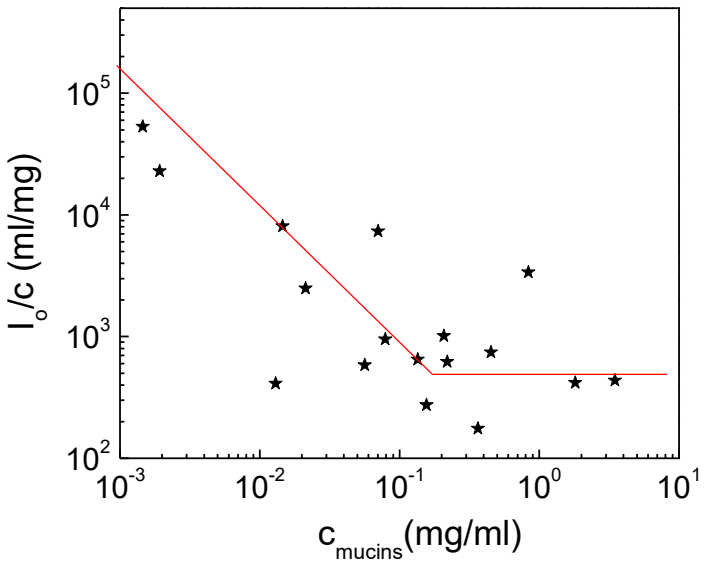

Figure 6.11. Reduced intensity (intensity over mucin concentration) against mucin concentration.

6.2.1. Intensity extrapolation at q→0

In order to estimate the value of the intensity at zero-q, we used the Debye plot, which is depicted in figure 6.12. In particular, we plot $1/I_o^{0.5}$ against q^2 for a low concentration of c=0.08mg/ml as an example; the same procedure performed for all the concentrations but is not shown. The linear fit of the data, y=ax+b, provides information about I_o and ξ, which is an apparent size (could be termed correlation length). More precisely, $\xi=(a/b)^{0.5}$ and $I_o=1/b^2$, where a is the slope and b is the intercept (see arrow in the plot, b=0.11).

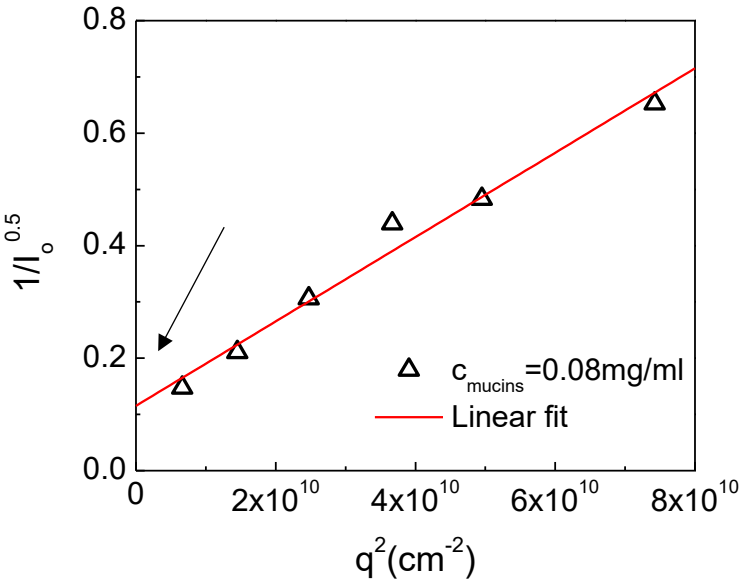

Figure 6.12. Debye plot, the inverse of the square root of the scattering intensity against q^2 for low mucin concentration of 0.08mg/ml. The arrow in the graph shows the intercept of $1/I_o^2$and through this we define I_o

The (static) correlation length was extracted and its values at different mucin concentrations are presented in figure 6.13, along with the hydrodynamic radius. Both ξ and R_H are concentration-independent up to a threshold value of about c=0.2mg/ml (same as that observed in the diffusion coefficient, figure 6.9) beyond which they exhibit a change with concentration: The hydrodynamic radius increases above the threshold concentration, c_e=0.2mg/ml. The correlation length decreases above the critical concentration.

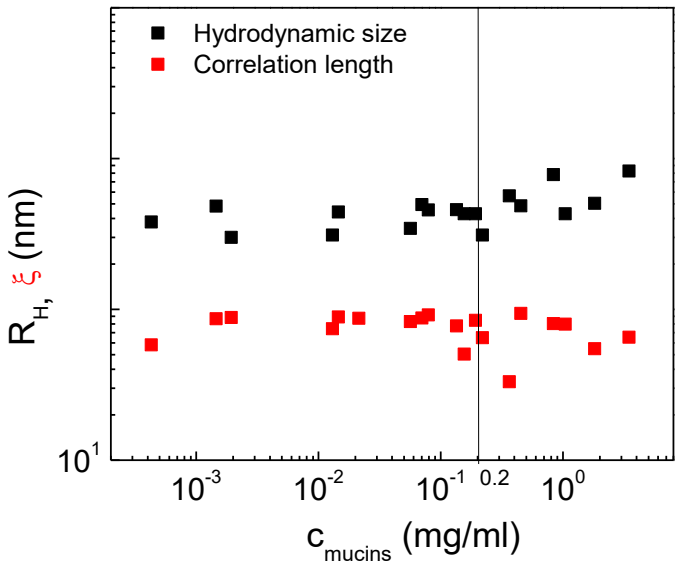

Figure 6.13. Apparent hydrodynamic size, R_H and correlation length, ξ, (static size) against mucin concentration. The vertical line indicates the critical concentration at 0.2mg/ml.

6.3 Saline environment

We investigated various salts at different concentrations. The reference concentration was c=0.08mg/ml (which is the same concentration was chosen in CABER experiments for studying the effects of salts and compare the system by using different methods, discussed in chapter 7). Artificial seawater was properly prepared in nanopure water by using four salts and the recipe of Kester et al. [92]. In order to mimic the natural environment we showed in table 6.4, the artificial seawater recipe by using different salts [92]. The pH has to be roughly 7-8. To address the role of each salt on viscoelastic properties, we used three different salts (bold letters in table 6.4) at different concentrations, including the natural one.

Table 6.4.Recipe for artificial seawater by using six different salts.

Salts	Natural Concentration [1] (mM)
NaCl	**409**
Na_2SO_4	28
KCl	**9**
$MgCl_2$	53
$CaCl_2$	**10**
$NaHCO_3$	23

[1] concentration of salt in seawater [92].

We focus in particular on calcium chloride, $CaCl_2$ and propose our hypothesis for its ability to swell the vesicles. Some results of measurements performed with sodium chloride, NaCl in combination with $CaCl_2$ are also presented and discussed.

6.3.1. Artificial seawater

The time autocorrelation functions in figure 6.14a exhibit a slow mode at all scattering angles. From the diffusion coefficient we extract a dynamic size (radius) of 400 nm (see figure 6.14b) which is similar to the size in the salt-free environment (455nm) by considering only the NLCA analysis. It appears that the different salts in

appear in nanopure seawater act synergistic and each one has its own functionality into the mucus behavior, but to now appreciably alter to overall dynamic size.

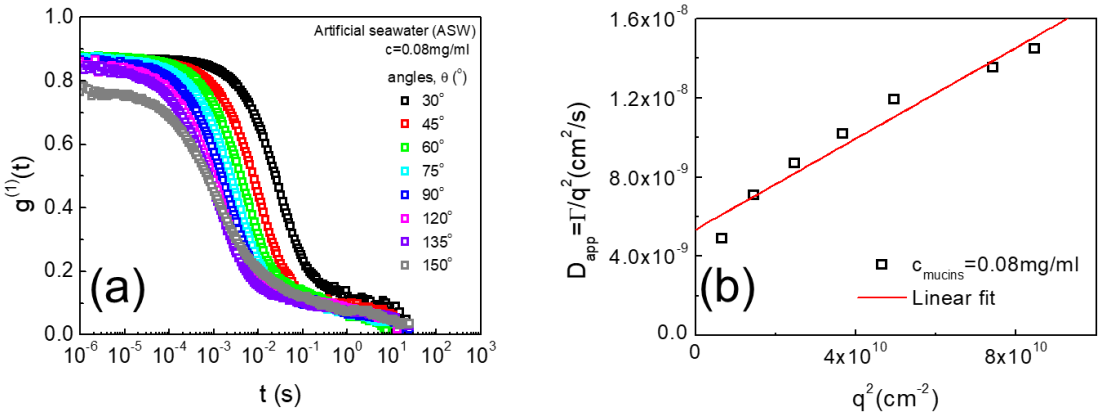

Figure 6.14. (a) Correlation functions in the reference concentration at 0.08mg/ml for different scattering angles in artificial seawater (pH=8); (b) Apparent diffusion coefficient against q^2 and size estimated at 400nm.

6.3.2. Diffusion coefficient

In figure 6.15a we show the concentration dependence of the diffusion coefficient. At c=0.08mg/ml (within the CABER working regime) various salts were tested and the diffusion dynamics does not change appreciably. Their values lie within the range of the respective values in salt-free environment. This observation can be explained by considering the following:

6.3.2.1. Effects of buffer solution

The reference concentration (c=0.08mg/ml) is taken as a salt-free environment since there is no added salt. For this reason, the ionic strength or the salt concentration ideally is equal to zero but actually, it is not. Ions from the citrate-pipes buffer solution during sample preparation influence the mucins interactions. The very low ionic strength provided from the buffer ions induces a screening effect (counterions). Hence, the addition of salt provides an environment in terms of ionic strength similar to that of nominally salt-free conditions. It seems that the amount of salt has not reached the needed threshold in order to strongly influence the size of mucins.

6.3.2.2. Slow mode

In our study, we focused on the fast dynamics of the system. In this region the presence of salt does not affect the microstructure, mucins are resistant to the ionic strength (considering the fast dynamic process). Here, is important to highlight that mucins are very strong polyelectrolytes and the ionic strength (provided by counterions which originated from buffer solution) is likely not enough to screen all interactions (especially in the slow mode). However, the effect of additional salt (monovalent/divalent) becomes more pronounced in these slow modes, which is discussed in detail in the next section.

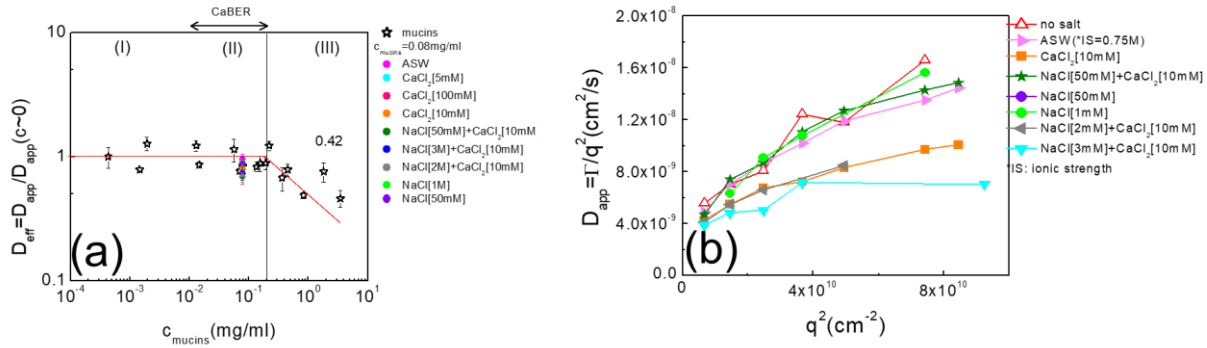

Figure 6.15. Left, a: Apparent diffusion coefficient normalized with the apparent diffusion coefficient when c→0 against mucin concentrations. The region (II) indicates the CABER working regime and the the reference concentration (c=0.08mg/ml) tested at different saline environments (different colors). Right, b: Apparent diffusion coefficient for different salts at their natural concentrations for reference concentration (c=0.08mg/ml).

Figure 6.15b depicts the ratio Γ/q^2 as function of q^2 of the mucin solutions for different salts under natural conditions. The mucus solutions (with and without added salt) exhibit a linear increase of the apparent diffusion coefficient, reflecting large objects, likely clusters. However, the saline mucus solutions exhibit a decrease of Γ/q^2 at large-q. In this regime, the more pronounced reduction is that associated with $CaCl_2$. An open question is whether we can link this decrease to an internal cross-linking of the mucin-like proteins. Actually, there is a well-documented work which supports this idea, by L. Böni et al. [12]. According to their measurements, Ca^{2+} has three distinct roles: i) the mucins condensation within vesicles, ii) the mucins decondensate via Ca^{2+} activated transporters in the vesicles membrane at high ionic

strength environments and iii) the mucins ionic gelation in the cold seawater. We discuss this in some detail in the next section.

Figure 6.16 shows the q-dependent intensity data both for static and dynamic measurements, DLS and SLS consequently. The static intensity discussed here was normalized according to the expression below. The intensity of sample, water and toluene were measured at different angles.

$$I^* = \frac{I_{static}}{I_{toluene}} \qquad \text{Eq.6.7}$$

For all solutions (with and without salt), the slope of I(q) is practically identical, equal to -3, either for static (full symbols) or for dynamic (empty symbols) measurements. The lowest concentration indicated as “no salt” in the plot is about c=0.03mg/ml and exhibits the lowest scattering intensity, whereas on the other hand the concentration of c=0.08mg/ml which indicated as c_{ref} in the plot, exhibits larger scattering intensity by one order of magnitude. The addition of ASW, $CaCl_2$ (0.01M) and NaCl-$CaCl_2$ (0.5M-0.01M) yields exactly the same response of mucus solution. We conclude that the amount of salt is not enough to strongly change the static/dynamic properties.

Remarkably, the presence of NaCl (0.5M) only yields a much larger scattering intensity. A tentative interpretation of this suggests that under these conditions we have predominance of closed vesicles in the solution. Aggregations of closed vesicles in the solution can be responsible for this rapid increase of the scattering intensity. At the same conditions (c=0.08 mg/ml mucin solution with 0.5M NaCl), the addition of 0.01M (natural concentration) of $CaCl_2$ reduces the scattering intensity (green data). This could be attributed to the divalent ions of Ca^{2+} and whose function is to swell (open-up) the vesicles. In the next section, we present some dynamic microstructural properties of mucus solutions affected by Ca^{2+}.

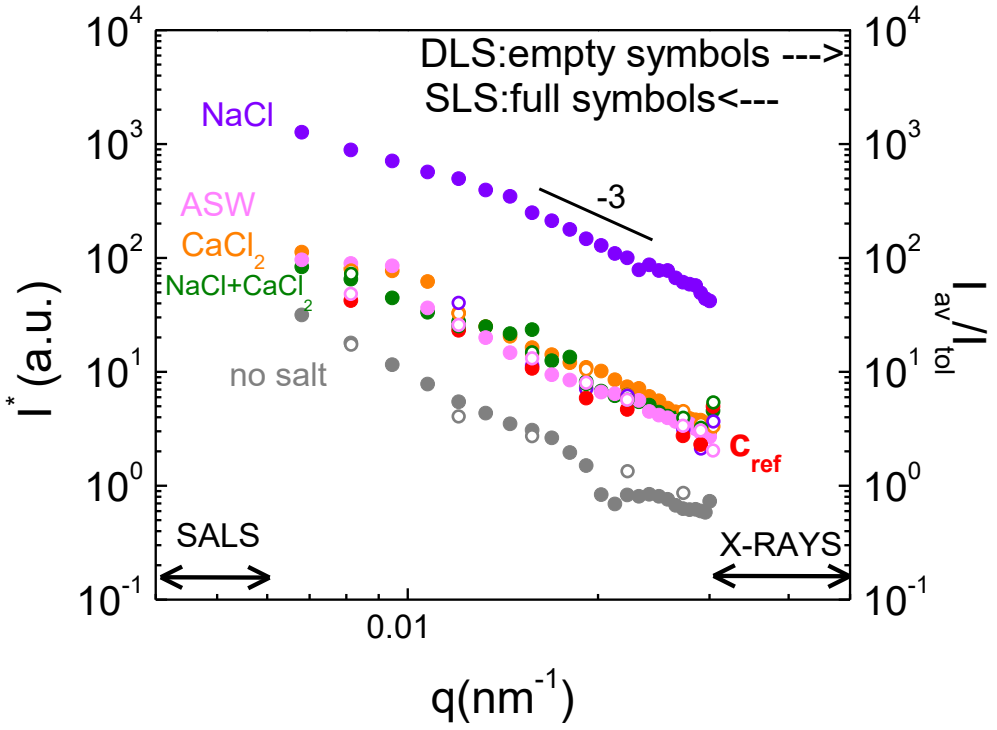

Figure 6.16. Normalized static and dynamic intensities against scattering wavevector, q. The left vertical axis represents the static intensity (full symbols) and the right vertical axis represents the dynamic intensity (empty symbols).

6.3.3. Impact of $CaCl_2$

The crucial role of $CaCl_2$ is studied separately from the rest of the salts. We provide some evidence about its role on the vesicles swelling. First, we tested it, at a reference concentration of mucin solution (c=0.08 mg/ml) by using various concentrations of $CaCl_2$. These results are presented in figure 6.17a where we observe the largest slow mode in the nominally salt-free environment (which is not 100% salt-free but contains ions from the buffer solution-low ionic strength, as already mentioned).

This slow mode tends to become smaller due to the addition of 5 mM of $CaCl_2$ which corresponds to a concentration lower than the natural concentration. A larger (than the natural) concentration of 100 mM $CaCl_2$ reduces the slow mode, whereas the natural concentration at 10 mM completely eliminates it. It is tempting to speculate that under natural conditions for $CaCl_2$ all vesicles swell and form a well-characterized, homogeneous network.

To further elucidate this scenario we compare in figure 6.17b the results of a similar test which includes a salt-free environment, $CaCl_2$ and a combination of two salts $CaCl_2$ and NaCl, all in their natural concentrations. We observe the presence of slow mode in the absence of salt whereas the two salts reduce the slow mode, apparently because of the screening effects and possibly to the swelling and opening-up of the vesicles. However, the last experiment using $CaCl_2$ only indicates (figure 6.17b) vanishing complete elimination of the slow mode.

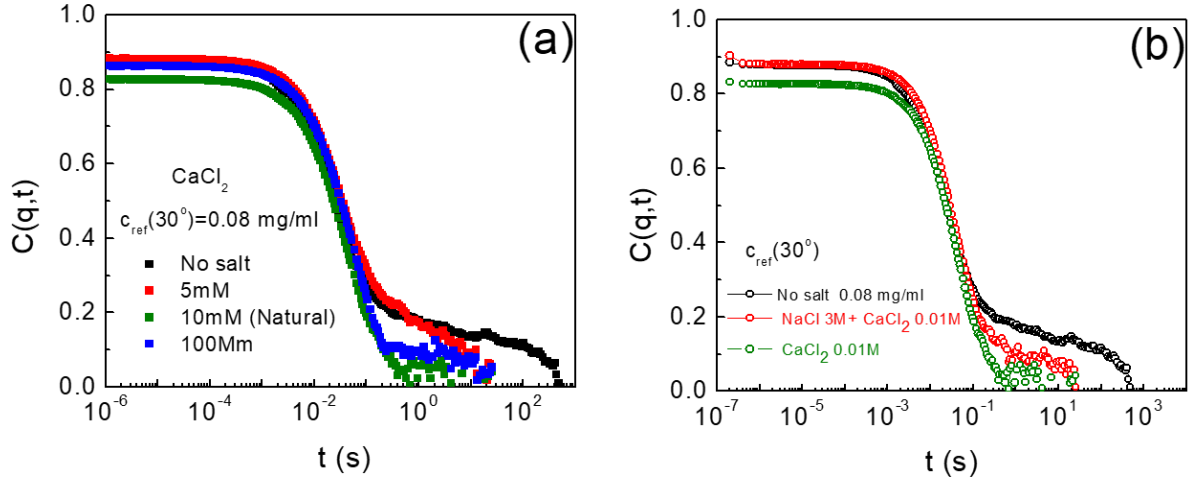

Figure 6.17. Correlation functions of mucins at a reference concentration of 0.08mg/ml. Left, a: Calcium chloride ($CaCl_2$) at different concentration at 30º. Right, b: Sodium chloride (NaCl) and calcium chloride ($CaCl_2$) effect at 30º.

The extracted (from the analysis of the correlation functions in figure 6.17a at different angles) apparent diffusion coefficients are plotted against q^2 in figure 6.18. The vertical arrow marks the threshold q-value, beyond which a decrease of Γ/q^2 at large-q in case we add $CaCl_2$ independently of concentration. Could we hypothesize again that this behavior originated from some possible internal cross-linking (via charges) for the mucin proteins? With the term cross-linking we are referring to the possible local aggregations (since diffusion drops at large q-values, at small length scales) within the mucin proteins via Ca^{2+} bonding. The same observation holds for figure 6.15 and for all salts at large q values, but for $CaCl_2$ the effect is more pronounced, as already discussed. However, the apparent size does not strongly change (it remains roughly the same, about 488 nm, average size), which reinforces that idea that the overall network/mucus dimension is not affected in this range of ionic strength.

Regarding figure 6.18, an additional comment refers to the way of measuring the solution. In case of a salt-free environment (black data) we measured up to 2000s, whereas in case of salt we performed averaging of shorter-duration measurements (100s for 20runs).

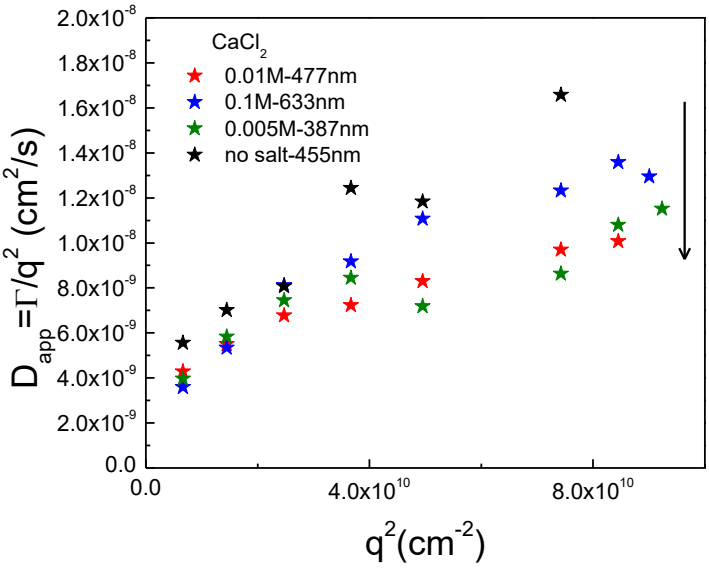

Figure 6.18. Apparent diffusion coefficient against q^2 at a reference concentration of c=0.08mg/ml for different concentration of calcium chloride ($CaCl_2$). The vertical arrow indicates the decrease of the diffusion at large-q when Ca^{2+}added, which is connected to locally created aggregates within mucin network.

The last analysis concerns the scattering intensities I(q) in the reference concentration (c=0.08mg/ml) at various $CaCl_2$ concentrations, below and above the natural value of 0.01M. As already mentioned, the power-law exponent remains -3 and the static and the dynamic intensity values coincide, whereas the difference in ionic strength of these three concentrations does not yield any appreciable change.

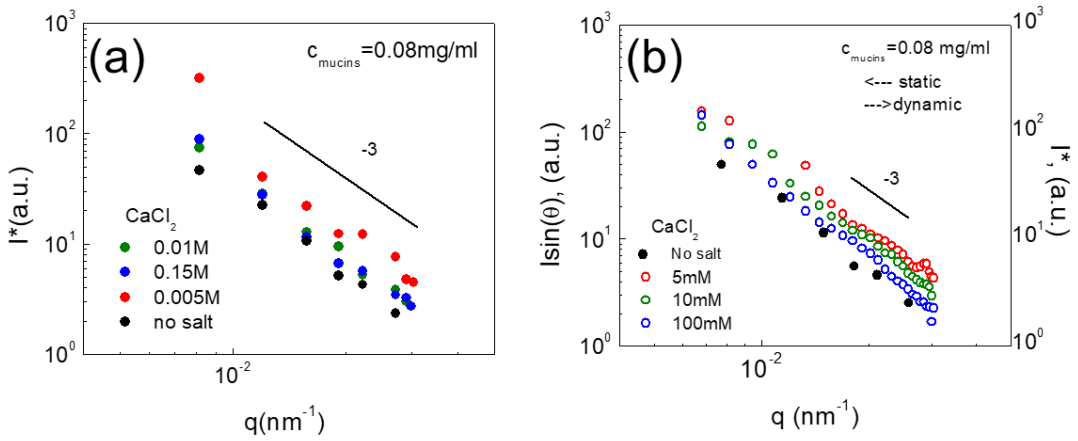

Figure 6.19. Normalized static (empty symbols) and dynamic (full symbols) intensities against scattering wavevector for a reference concentration of c=0.08mg/ml; (a) Dynamic intensity; (b) dynamic and static intensity.

The effects of adding 0.01M Ca^{2+}[12], [43] can be summarized as follows:

1) Vesicles condensation: Mucin proteins are packed into the vesicles via Ca^{2+} bonding.

2) The opening of the vesicles (through a complete swelling) is realized via Ca^{2+}-activated transporters in the vesicle membrane at high ionic strength [43]. This is consistent with the absence of slow mode and higher viscoelasticity (discussed in the context of CABER experiments).

3) Possible cross-linking at large q-values (small length scales) via Ca^{2+} bonding: structure collapses (via local aggregation) at high salt concentrations. Aggregations lead to ionic gelation and the diffusion slows down.

In figure 6.20, we show results from Böni et al. [12] which indicate the crucial role of Ca^{2+} on the swelling and opening of vesicles in comparison to the monovalent ions of Na^{+} via turbidimetric measurements, for the entire hagfish exudate (mucin vesicles and protein skeins together, not simply isolated mucin as in the present work). In the absence of $CaCl_2$ higher absorption values are reported, which is attributed to some remaining condensed vesicles. The condensation of the vesicles vanishes once 0.01M of $CaCl_2$ are added, as judged by the decreased absorption values. Even if the ionic strength is high, in the absence of $CaCl_2$ some vesicles remain condensed and affect microscopic properties but also bulk properties such as viscoelasticity (to be discussed in Chapter 7). Even if this system (entire hagfish exudate) differs from

the isolated mucin, we believe that the findings are relevant to (and consistent with) the present work.

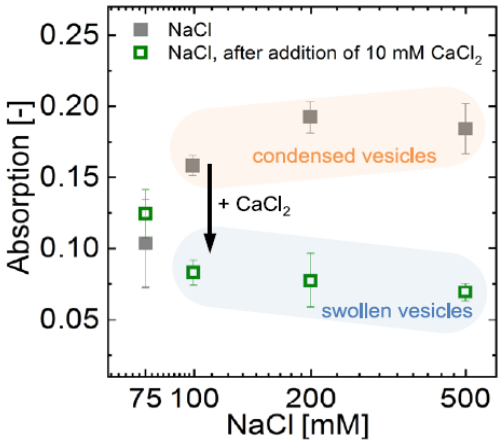

Figure 6.20 Hagfish slime exudate under UV-VIS turbidimetric measurements. The presence of NaCl shows some remained condensed vesicles (grey full symbols in the orange area) due to the larger absorption. The presence of NaCl with 0.01M of $CaCl_2$ (natural concentration) swells these condensed vesicles (green open symbols in the blue area) and this is indicated due to the decrease in the absorption values [12] .

6.4 Discussion and Summary

Here we summarize the main results in a salt-free environment as well as in the saline one. The technique used in order to characterize and investigate dynamics of mucin glycoproteins is dynamic light scattering technique with three different methods of analysis, CONTIN, cumulant and non-linear cumulant analysis (NLCA). The last method used (NLCA) provides the proper apparent hydrodynamic size and these results shown as finals in the present thesis because seem to be the most appropriate for the investigated system.

Salt-free environment:

1) Increasing concentration yields the presence of the slow mode and this is illustrated in figure 6.9 (yellow box) due to possible non-ergodicity. In this case, as it is written in that paragraph, another more appropriate technique is required, multi-speckle dynamic light scattering (MSDLS)[90].
2) The diffusion dynamics seems to reveal similar behavior with that of polyelectrolytes (with dilute and semidilute regimes spanning several decades) and the so-called entanglement concentration to be at about

0.2mg/ml. A qualitative biological implication is discussed in chapter 8, general conclusions.

Saline environment:

1) The microscopic properties from light scattering indicate that the diffusion dynamics are not strongly influenced by the addition of salt (figure 6.15a). If we consider very strongly charged mucins it is expected that the amount of salt added is not enough to influence the diffusion appreciably, even if there is also small amount of buffer solution in the sample.
2) The q-dependent static and the dynamic intensities exhibit a power-law $I(q) \sim q^{-3}$ at high q's, and an absence of Guinier plateau region at lower q-values. As mentioned above, SALS and X-rays can provide access to these regions.
3) The divalent cation of Ca^{2+} seems to play a very crucial role on this system. Different effects have been investigated such as: i) vesicles condensation ii) opening of the vesicles, iii) physical cross-links at the microscopic scale. Section 6.3.3 addresses this topic extensively.

Chapter 7: Rheology of hagfish mucins

In this chapter we discuss the rheological response of hagfish mucins under two aspects: i) the extensional deformation (stretching) and ii) the oscillatory shear deformation (SAOS). Concerning the former, first we focus on the concentration effect in a salt-free environment, and then we examine the impact of salt on the extensional properties. Regarding the latter, we investigate the linear viscoelastic properties. We explain the sample preparation procedure which differs from the normal protocol used (reported in chapter 6) and discuss the analysis of the SAOS measurements.

7.1. Extensional rheology

Stretching tests were performed with the HAAKE Caber rheometer at different mucin concentrations. Experiments were conducted at room temperature (typically 23^{o}C) and the diameters of the upper and the lower plate were 6 mm. The gap was set to roughly 12 mm (chosen empirically). It corresponds to the plates distance after the step-stretch.

The strike time was selected to be 50 ms and in this period, the top and the bottom plates reached this gap. 20 ms corresponds to the lowest trustable strike time, whereas times below 20 ms were not needed since the plates separation is very rapid and the thinning not very clearly detected with a laser micrometer [93].

We did not have to consider evaporation issues with water during the measurement since the experiment was very fast. For each sample we prepared three loadings and for each loading the thinning of the diameter was measured three times. This allowed testing reproducibility of the measurements and extracting reasonable averages. The solution (80μl) was placed at the bottom plate with a micropipette of 100μl.

CABER samples were prepared with protocol B (see section 4.2.2, network formation). The ionic strength is one of the most crucial parameters because of the polyelectrolyte nature of mucins. Here, the ionic strength is due to the buffer solution (stabilized vesicles), as discussed in Chapter 6. The following coding was used for protocol A : i) “salt free environment”: only presence of ions from buffer and ii) “saline

environment": ions from buffer solution plus additional ions under investigation (e.g. NaCl or KCl etc.)

7.1.1. Impact of concentration

The effect of concentration (figure 7.1) is discussed in the context of diameter of the mucin filament which decreases with time. Different curves correspond to different concentrations (figure 7.1b), whereas the values next to the curves correspond to the exact value of concentration in mg/ml. The dashed arrow indicates the direction of increasing concentration.

Figure 7.1a depicts a typical example of extensional measurement (a relatively high concentration of mucins). The vertical axis represents the diameter of the filament which decreases with time and it is normalized with the diameter of the plate, D_o. The horizontal axis represents the experimental time, once the plates are separated until the sample breaks. The dirn mection of increasing concentration in figure 7.1.b can be identified by: i) the break-up time in the horizontal axis, and ii) the range of the viscoelastic plateau (a short emerging plateau which becomes more evident when the material is more viscoelastic). The line in the graph is the exponential fitting of the data using eq. 3.12:$\frac{D(t)}{D_o} = \left(\frac{GD_o}{4\sigma}\right)^{1/3} \exp(-\frac{t}{3\lambda})$. The adjustable parameters are the relaxation time, λ, and the apparent modulus, G_{app}.

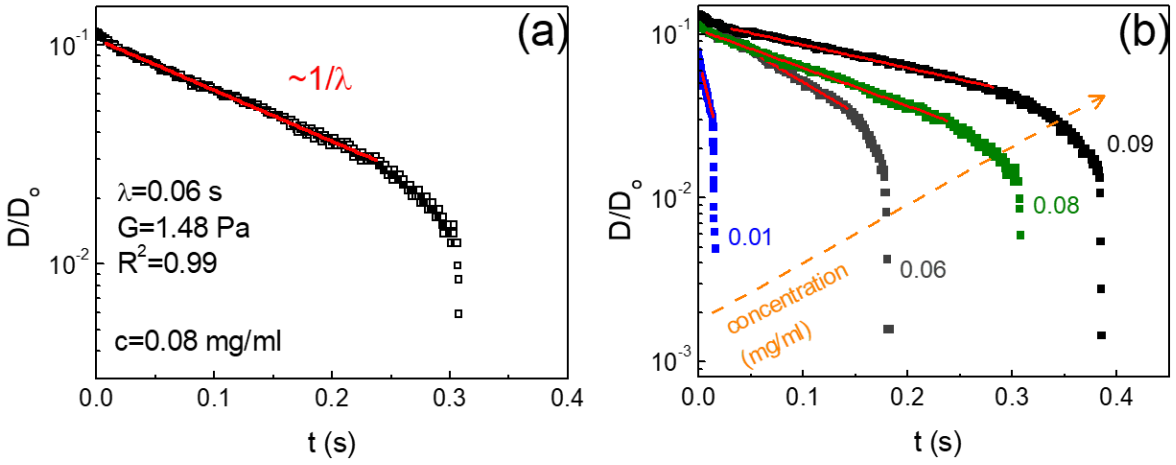

Figure 7.1. Diameter of the filament normalized with the diameter of the plate against time: (a) data for a concentration of 0.08 mg/ml is shown and the red line represents the exponential fitting of the data; (b) Different concentrations from low to high in the direction of the arrow.

These parameters are plotted against mucin concentration in figure 7.2. In the plot of figure 7.2a we show the relaxation time (full symbols) and the break-up time (empty symbols) as functions of concentration. The dashed line represents the concentration limit in the CABER working regime, the so-called “beads-on-a-string” (BOAS) effect (see inset photo). Beyond this limit, the system forms connected drops which reflect the presence of instabilities [60]–[62]. The relaxation time as well as the break-up time increase with concentration, apparently because the filament thins (decrease its diameter) at a slower pace when the amount of mucin is larger.

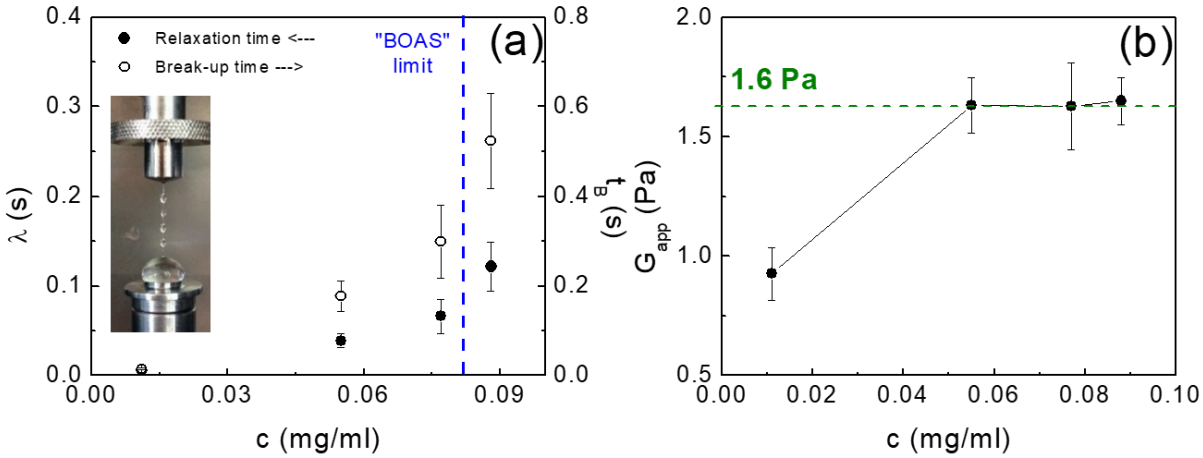

Figure 7.2. (a) Relaxation time (filled symbols) of mucin proteins against polymer concentration on the left vertical axis and break-up time (empty symbols) of mucins on the vertical right axis. The dashed like shows the concentration limit on such extensional tests (see inset photo); (b) Apparent elastic modulus against biopolymer concentration. The relaxation time and the apparent modulus are extracted from the exponential fit to the data. The break-up time is the point in Figure 7.1 where the diameter stopped thinning.

Figure 7.2.b depicts the apparent elastic modulus against mucin concentration. At the lowest concentration the value of G_{app} is about half that at the higher concentrations where it remains constant (about 1.6 Pa) within experimental error. Moduli values of other mucus are in the range of 0.1<G<100 Pa and the corresponding table 7.3 is discussed in paragraph 7.2.2 below [35]. Mucin-like glycoproteins exhibit strong repulsions within the protein chain due to the charged side sulfonate groups (SO_3^-). The small amount of buffer solution (with ionic strength of about 0.08M) in the sample plays the role of counteriors (possibly small screening effect), as discussed in Chapter 6.

Even if this an apparent modulus, its trend is in the right direction as it increases with concentration in virtually salt-free environment (i.e., strong stretching regime), as also predicted [94]

7.1.2. Impact of salt

Now we examine the rheological response of mucins at a chosen reference concentration of c=0.08 mg/ml, in presence of different added salts. The question we wish to address is why we use different salts (monovalent and divalent ions) in order to test the mechanical stretching response. The general biological answer is that hagfish slime exhibits its unique properties in seawater (discussed in Chapter 4). The effects of salts on mucins in different saline environments are discussed below. We want to remind to the reader that in our comparison and arguments we do not include the concentration of the buffer solution (with ionic strength being 0.08M) which is very low and does not affect mucin properties appreciably. The salts we used are bolded in table 6.4 (recipe of ASW).

7.1.2.1. Monovalent ions: sodium chloride (NaCl) and potassium chloride (KCl)

In figure 7.3 we show the normalized diameter of the filament against time. Figure 7.3a depicts results for NaCl and figure 7.3b for KCl. In both cases, measurements were performed at a reference mucins concentration of c=0.08 mg/ml. The natural concentration (in seawater) of NaCl corresponds to 0.5 M and for KCl to 0.01M.

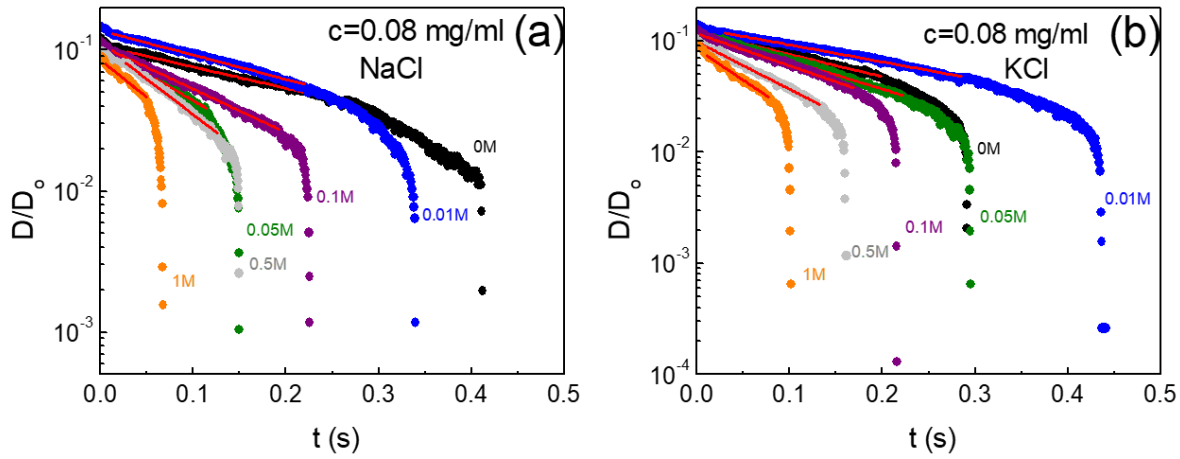

Figure 7.3. Diameter of the filament normalized with the diameter of the plate against time: (a) Different concentrations of NaCl -monovalent ions-; (b) Different concentrations of KCl monovalent ions-. The reference concentration of mucins was 0.08mg/ml.

In figure 7.4 results for both NaCl and KCl solutions are shown with respect to their relaxation and break-up time. For NaCl both characteristic times remain relatively constant whereas for KCl they decrease as the concentration of salt increases. To interpret this result we conjecture that the higher the relaxation time, the more viscous and 'coherent' is the viscoelastic mucin network.

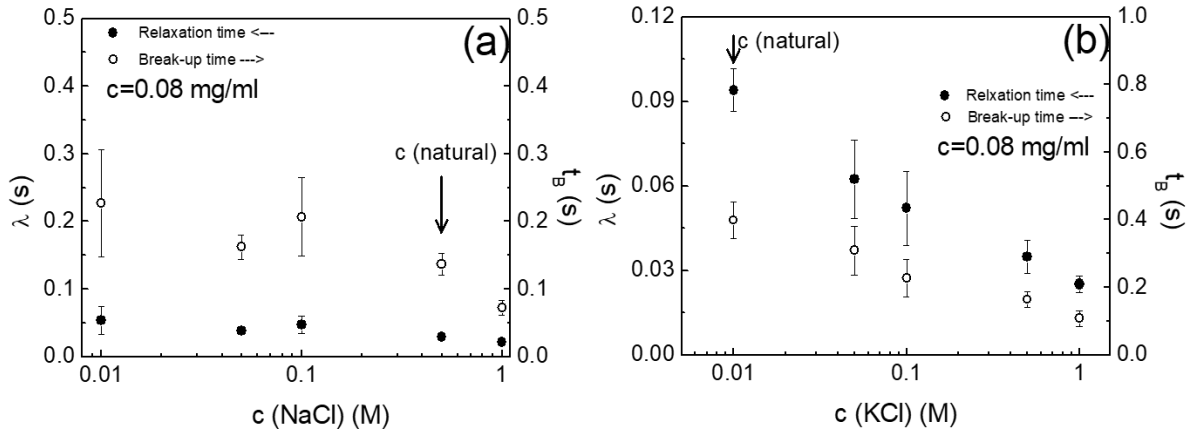

Figure 7.4. Relaxation time λ (filled symbols) on the left vertical axis and break-up time t_B (empty symbols) on the right vertical axis against salt concentration: (a) monovalent ions of NaCl at a reference concentration of mucins of 0.08mg/ml; (b): monovalent ions of KCl at the same reference concentration. Natural concentration of salt in the seawater indicated with the vertical arrow.

The extracted apparent modulus provides an estimate of the apparent elastic contribution in the material response, as already mentioned. The two salts examined

here exhibit a similar concentration dependence of G_{app} (figure 7.5). The vertical arrow indicates the natural concentration of the specific salt in natural seawater. For NaCl we observe slightly reduced elastic contribution in the seawater mucin properties whereas for KCl, the largest elastic contribution in the network is reached at natural conditions. We can clearly observe that, unlike the predictions of weak increase of plateau modulus with solution concentration [94] here the apparent modulus decreases.

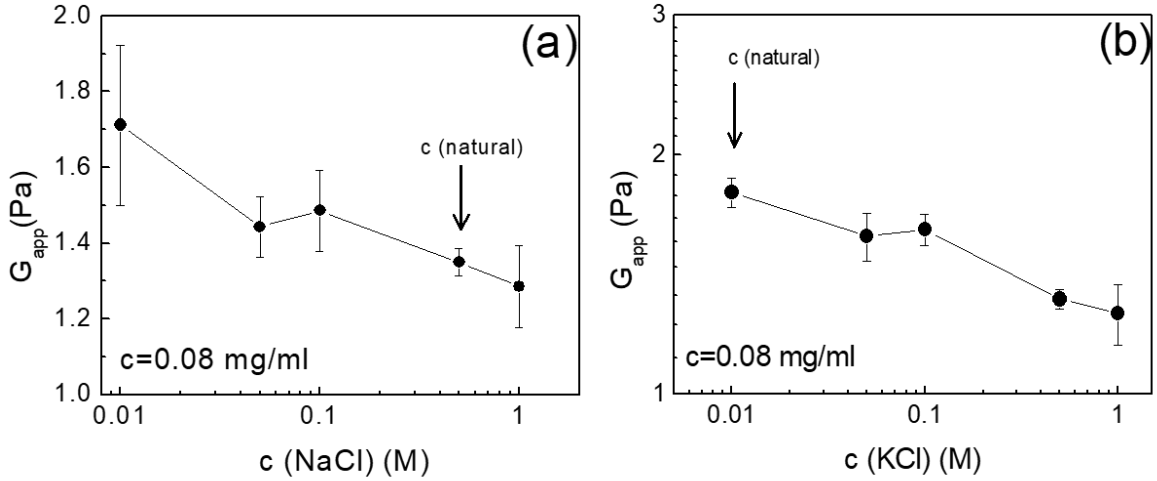

Figure 7.5. Apparent modulus, G_{app}, against salt concentration, at a reference concentration of mucins of 0.08mg/ml: (a) NaCl; (b) KCl. Natural concentration of salt in the seawater indicated with the vertical arrow.

7.1.2.2. Divalent ions: $CaCl_2$

In seawater we can find many divalent ions, predominantly Mg^{2+} and Ca^{2+}. In the present work we investigated the divalent ion of Ca^{2+}. It is believed that it affects substantially mucus function and consequently the final hydrogel properties, more than other divalent ions such as the Mg^{2+} [43]. One key characteristic of Ca^{2+} is the opening of vesicles in the suspension which is still under investigation [12], [43]. As already mentioned in chapter 4, vesicles swell and open-up (release of mucin-like proteins) in water. What remains uncontrollable, yet crucially important for properties, is the amount of vesicles which swell in a salt-free environment. In seawater, all vesicles are supposed to be opened due to the synergistic effects of all salts.

Figure 7.6 shows the effect of $CaCl_2$ on the extensional properties, at different concentrations. The thinning of filament diameter is depicted in figure 7.6a and the

relaxation time and the break-up time against salt concentration in figure 7.6b. We observe a non-monotonic behavior compared to the monovalent ions above (NaCl and KCl).

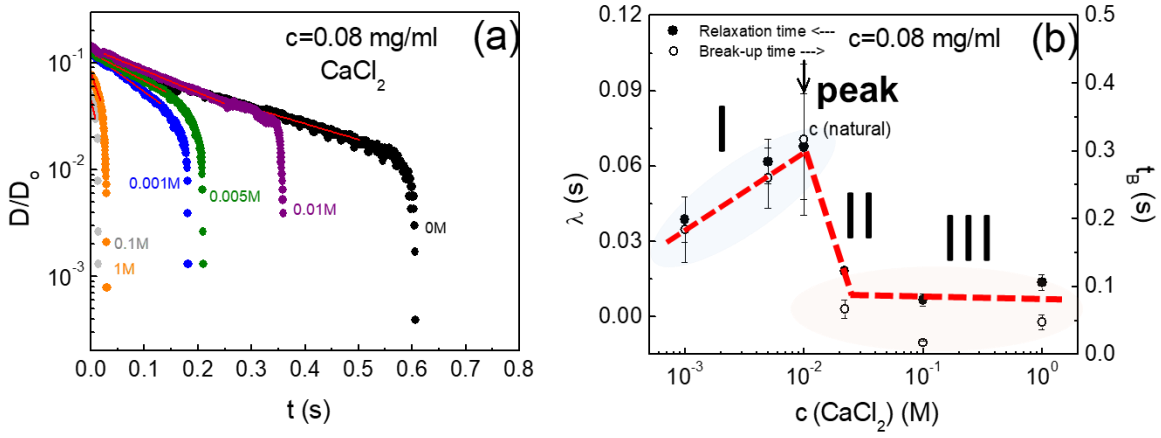

Figure 7.6. (a) Diameter of the filament normalized with the diameter of the plate against time for different concentrations of $CaCl_2$ at a reference concentration of mucins of 0.08mg/ml; (b) Relaxation time λ (filled symbols) on the vertical left axis and break-up time t_B (empty symbols) on the right vertical axis against concentration of $CaCl_2$ at the same reference concentration. The vertical arrow shows the natural concentration of salt in the seawater.

The characteristic times (figure 7.6b) follow three distinct types of concentration dependence:

Region I: times increase up to a point where the natural concentration is reached (0.01M). This behavior could be linked to the network enhancement where more and more vesicles swell and open-up. The maximum time corresponds to the natural environment and appears to reflect the fully developed hydrogel due to the complete swelling of all vesicles.

Region II: The peak is proceeded by a decrease of the characteristic times. This possibly happens due to the collapse of the structure formed by the mucin molecules and eventual attractions with increasing ionic strength.

Region III: The characteristic times remain constant even if the concentration of salt increases at very large ionic strength. This is attributed to a saturation of counterions.

Figure 7.7 represents the G_{app} as function of salt concentration. A change in concentration dependence (albeit weak) can be observed at the same (natural) salt concentration and we may distinguish the same three regions as above.

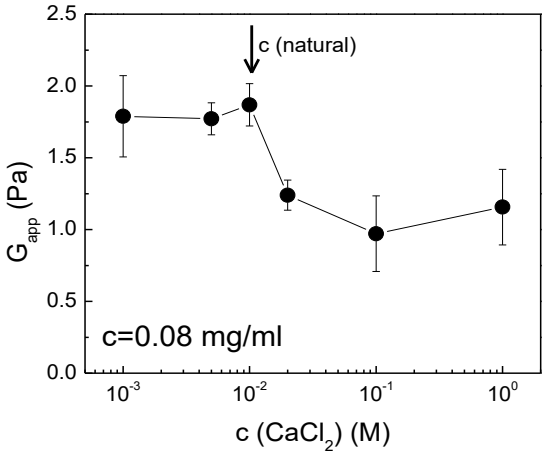

Figure 7.7. Apparent modulus G_{app} against concentration of $CaCl_2$ at a reference mucins concentration of 0.08mg/ml, with the vertical arrow showing the natural concentration of $CaCl_2$ in seawater.

7.1.2.3. Artificial seawater

In this section we focus on the artificial seawater's influence on mucus stretching. The ionic strength of pure (100%) seawater (recipe in table 6.4) is 0.7M for the use of four salts and 1M for all salts presented. Figure 7.8a shows the time-thinning normalized diameter of the filament and figure 7.8b the viscoelastic relaxation time and the break-up time versus concentration. At 100% seawater which corresponds to the natural conditions, we note the weakest viscoelasticity, attributed to screening of interactions.

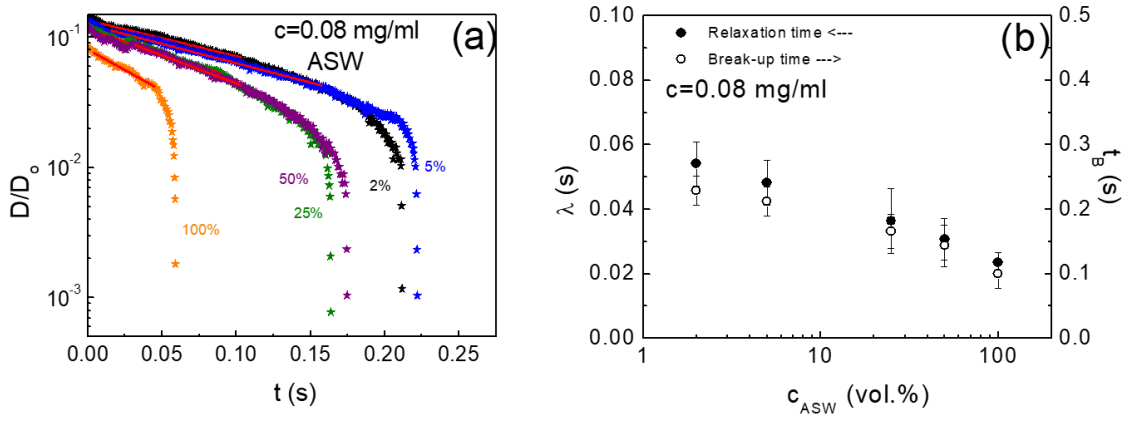

Figure 7.8. (a) Diameter of the filament normalized with the diameter of the plate against time for different concentrations of artificial seawater at a reference concentration of mucins of 0.08mg/ml; (b) Relaxation time λ (filled symbols), on the vertical left axis and break-up time t_B (empty symbols) on the right vertical axis against concentration of artificial seawater at the same reference concentration. The pure seawater concentration corresponds to the natural environment.

Similar remarks hold for the apparent modulus as function of seawater concentration (figure 7.9). The screening effect slightly weakens the viscoelastic behavior. G_{app} decreases with concentration of ASW (i.e., addition of salt), unlike expectations from scaling theory on simple polyelectrolyte gels[94].

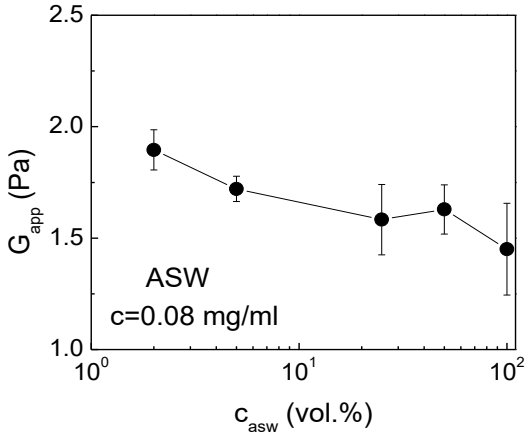

Figure 7.9. Apparent modulus G_{app} against concentration of artificial seawater at a reference concentration of mucins of c=0.08mg/ml. The pure artificial seawater corresponds to the natural environment of mucins.

7.1.3. Summary of extensional results

Monovalent ions exhibit a monotonic behavior as the concentration of the salt increases. Despite the small differences between salts for both λ and G_{app}, it seems that, NaCl has weaker contribution on the viscoelastic properties at the natural concentration in comparison to KCl. This effect is probably due to the amount of salt which needed to screen the inter- and intra- molecular interactions: c_{NaCl} (0.5M)>c_{KCl} (0.01M). The relaxation time (figure 7.10a) and the apparent modulus (figure 7.10b) for the more saline environment are lower due to the screening of the interactions.

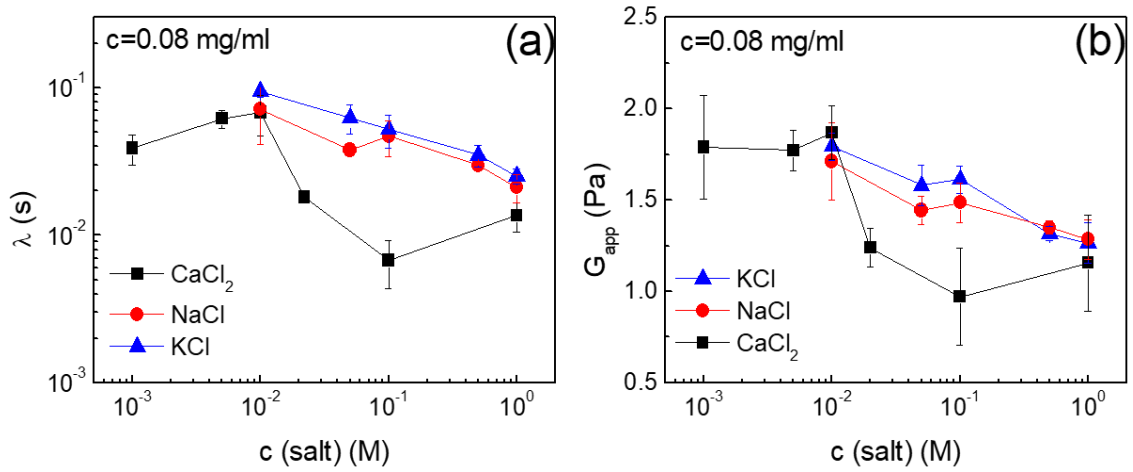

Figure 7.10. Reference concentration of c=0.08mg/ml at different salts. (a) Relaxation time against salt concentration; (b) apparent modulus against salt concentration. Both the relaxation time and the apparent modulus decrease as the salt concentration increases due to the screening effects.

7.2. Oscillatory rheology

Mucus systems such as hagfish mucins are known to be very soft viscoelastic systems with very low elastic modulus (e.g. 0.01 Pa) [11], [45]. Measuring oscillatory shear rheology is challenging in these cases due to the complex sample handling and weak signal. Here, we address two challenges: i) the sample preparation, which is important to provide appropriate signal (torque) and ii) the rheological protocol for assessing the system and for long-time measurements.

7.2.1. Sample preparation and rheological protocol

i) Sample preparation (Protocol B)

The sample preparation discussed in section 4.2.2. follows protocol A. Protocols A and protocol B yield hydrogel mucus networks with different viscoelastic properties. A comparison is summarized in table 7.1.

Table 7.1 Sample preparation protocols

Protocol A (Non-dialyzed mucins)	**Protocol B (Dialyzed mucins)**
Ions only from buffer solution	Ions-free environment
Low ionic strength, (0.08M)	Absence of ionic strength, ideally (0M)
Some vesicles possibly remain closed (packed mucins)	All vesicles are swollen (mucin released)

Figure 7.11 illustrates the dialysis procedure where day 1 on the left is the first day of dialysis and on the right is the last day of dialysis (usually dialysis lasts 3 days). In order to prepare the samples we used dialysis tubes (with the molecular weight of tube pores 25kDa), two plastic clumps in order to close the tubes (top and bottom), fresh nanopure water and the initial material (here mucin vesicles).

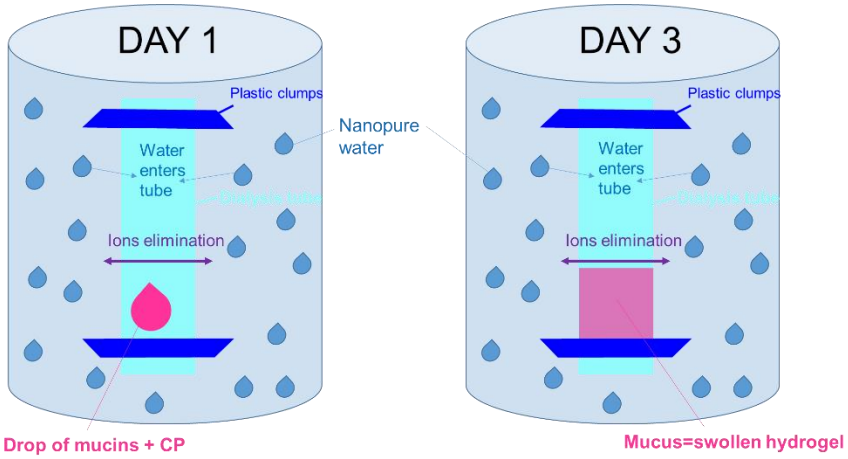

Figure 7.11. Cartoon illustration of sample preparation protocol B for the dialyzed mucins. On the left we show the beginning of dialysis (DAY 1) and on the right the end of dialysis (DAY 3).

Dialysis steps:

1) A big glass vial (1-2l) was filled with fresh nanopure water.
2) A dialysis tube was used with the one side closed (with the plastic clump).
3) A small amount of stabilized mucin vesicles (100-200µl) was added.
4) The other top side was closed with the plastic clump and the tube was placed in fresh nanopure water environment.
5) The sample was kept in the fridge (4ºC) for 3 days and water was changed five times per day.

Thus, we can prepare relatively large amounts of sample in a truly salt-free environment. The sample after dialysis was removed from the tube gently and was placed in a new vial with known mass (see figure 7.12). In this way we estimated the water content, hence the mucus concentration. We explain this simply by means of the following example.

Figure 7.12 Mucus after dialysis

The mass of mucin and water (mucin+water=mucus) weights 1.6 g (assuming water density 1 g/ml). In the dialysis bag we added 100 µl of buffer solution with stabilized mucin vesicles. The vesicles concentration was 27 mg/ml in the buffer (initial batch). Hence, the mucus concentration was 2.7 mg/1.6 ml =1.68 mg/ml.

ii) Rheological protocol

Measurements were conducted with a stress-controlled rheometer MCR501 from Anton-Paar (Austria). Two different stainless steel cone-plate geometries were used. For low concentrations a diameter of 50 mm with cone angle of 1º (truncation of 102 µm), and for high concentrations a diameter of 25 mm with angle of 2º (truncation of 50 µm). The minimum torque was 0.1 µN.m. Measurements were performed mainly at 20ºC whereas some tests were conducted at 5ºC which corresponds to the natural mucin environment in seawater. The measurements protocol involved: i) system rejuvenation via dynamic strain sweep experiments at different frequencies, which also provides the limits of linear viscoelasticity; ii) dynamic frequency sweep tests in order to explore the linear viscoelastic response at small strains ; iii) creep and recovery experiments at different stresses.

It is important to note that water-based systems are prone to evaporation. This strongly influences the system concentration and consequently its mechanical response. For this reason, we developed an “evaporation protocol based on olive oil”. A metal ring with a Teflon ring in its bottom was placed at the perimeter of the bottom stationary plate and sealed with grease. The sample was loaded on the rheometer and the top plate was moved down in order to reach the trimming position. Dialyzed mucins were properly and carefully trimmed by means of a scalpel and the area between the sandwiched sample and the ring was filled with olive oil for effective sealing. The cartoon of figure 7.13 illustrates this protocol.

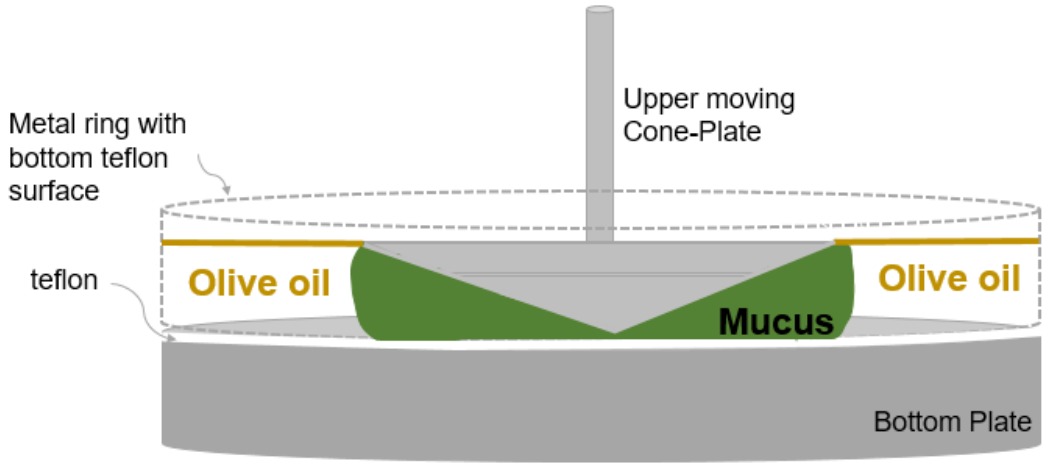

Figure 7.13. Cartoon illustration of the rheological protocol used in order to eliminate evaporation.

By following this protocol, we have the ability to measure for many hours at the same concentration since we completely avoid water evaporation. Olive oil does not diffuse into the sample and does not interact with mucin. Below, in figure 7.14 we show the real setup after the measurement was completed and the top cone moved up, where the viscoelastic mucin solution is also shown (kept with a spatula, forming a thread resembling egg white).

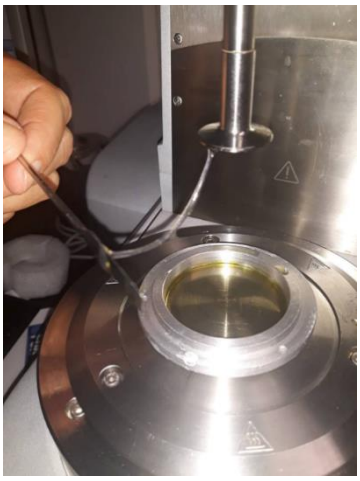

Figure 7.14. Dialyzed mucus after measurement in a stress-control rheometer with the solvent trap setup. The olive oil shown in the bottom plate along with the containing ring.

7.2.2. Small amplitude oscillatory shear (SAOS)

Different concentrations of mucus were measured under small amplitude oscillatory shear in order to determine the linear and the nonlinear regimes. Concentrations ranging from c=0.07mg/ml to 3.3mg/ml were measured at three frequencies (0.1, 1, 10rad/s). In figure 7.15, we show typical data at 1rad/s and 20^{o}C. The elastic modulus (G') does not exceed the value of 10Pa for all measured concentrations.

Figure 7.15a depicts data for the lowest concentration of mucus where the crossover is at 100% strain amplitude, whereas at larger concentrations the complete melting of the system is not detected. An indication of a possible crossover appears at very large strain amplitudes above 1000%. This type of behavior is similar to other mucus systems such as the mammalian lung mucus [41] and the cystic fibrosis sputum [35].

Figure 7.15c is the highest concentration measured and we show two sets of data at the same concentration (3.3mg/ml). The black circles represent the salt-free environment (as also shown for the other two concentrations); on the other hand, the

light blue squares represent the artificial seawater environment of mucus. In the latter case, the modulus drops by one order of magnitude and the vertical arrow indicates this direction. The decrease of both elastic (G') and the viscous (G'') moduli is due to the electrostatic screening of the interactions within mucin proteins. Next, we explain briefly the procedure follower in order to prepare the saline mucus sample.

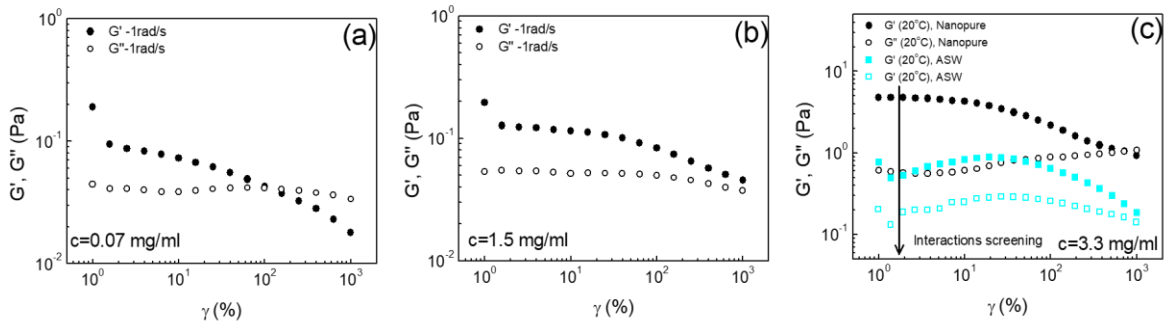

Figure 7.15. Dynamic strain sweep (DSS) tests performed at different concentrations, frequency of 1rad/s and T=20°C: (a) c=0.07mg/ml, low mucus concentration; (b) c=1.5mg/ml, intermediate mucus concentration; (c) c=3.3mg/ml, high mucus concentration, in nanopure water (black circles) and in artificial seawater (light blue squares).

In paragraph 7.2.1 and figure 7.11, we explain and show the second sample preparation procedure (protocol B) for the dialyzed mucus. In the case of the artificial seawater, we followed exactly the same procedure with the only difference that the dialysis was performed in the artificial seawater. More precisely, instead of using nanopure water (step 5) we used saline water with the recipe described in table 6.4 [92].

The goal of these measurements was to accurately probe the viscoelastic properties. Mucus is characterized by a very soft nature which is translated to a very low elastic and viscous moduli in comparison to other synthetic or biological polymers in semidilute and concentrated solutions (e.g. polystyrene). In the following table, which is taken from the literature [35], we show typical moduli values of such systems (eventually animal mucus) which are in agreement with our findings.

Table 7.2. Typical values of viscosity, elastic and viscous modulus of various animal mucus which taken from [35].

Animal	Type of mucus		ω (rad/s)	η'' (Pa·s)	G^* (Pa)	G' (Pa)	G'' (Pa)	δ
Dog	Respiratory	Subglottis	1	1.0–20	4.8–66	4.7–63	1.0–20	12–18
		Tracheal	0.05–400	0.038–32	2.1–85	2.0–80	0.50–40	9–54
		Bronchial	1		14–120			
Pig	Gastrointestinal	Gastric	0.01–100	0.13–63	3.3–34	3.2–32	0.63–13	11–22
		Small intestinal	0.01–100	0.063–5.0	0.19–12	0.18–10	0.050–6.3	16–32
		Colonic	0.01–100	0.16–1000	64–160	63–160	10–16	6–9
Rat	Respiratory	Nasal	1–100	0.0012–4.4	0.45–11	0.44–8.2	0.062–8.4	8–60
		Tracheal	1–100	0.0050–2.8	1.6–9.1	1.5–8.2	0.17–5.8	6–43
Horse	Respiratory	Tracheal	10	0.61–1.2	19–36	18–34	6.1–12	19–20
Rabbit	Respiratory	Tracheal	1		35–130			
Ferret	Respiratory	Tracheal	1		12–110			

7.2.2.1. Yield strain

The yield strain and stress mark the transition from solid-like to liquid-like response of the system but we note that the nonlinearity in the system appears before yielding. In a DSS experiment, there are different characteristic values of strain (and corresponding stress) that can be determined: i) onset of nonlinearity, ii) the change of slope with strain in the stress-strain curve, iii) the crossover point where G'=G'', and iv) the strain at which the G'' has its maximum. Below we explain for each one the way we use.

i) <u>Onset of nonlinearity</u>

We use as example the lowest concentration measured (c=0.07mg/ml). The onset of nonlinearity in this case is a strain amplitude of 10% at 1rad/s. We observe that at the same concentration in figure 7.15a (G'~0.1Pa) and figure 7.16 (G'~0.04Pa) moduli are slightly different. This small deviation is due to the fact that the first value corresponds to the first rejuvenation performed and the second one to the second rejuvenation test. We explain this below in the discussion part (v).

In section 7.2.1 in the second part (ii) of the rheological protocol, we noted that measurements were performed at 20^{o}C whereas the natural environment is at 5^{o}C. Once the measurements at 20^{o}C were finished the temperature was cooled down at 5^{o}C and new set of measurements performed. After these tests, the temperature was fixed again to 20^{o}C in order to test the consistency of the sample rejuvenation. For this reason the second set of measurements at 20^{o}C was called "second rejuvenation" (written in the legend of figure 7.16).

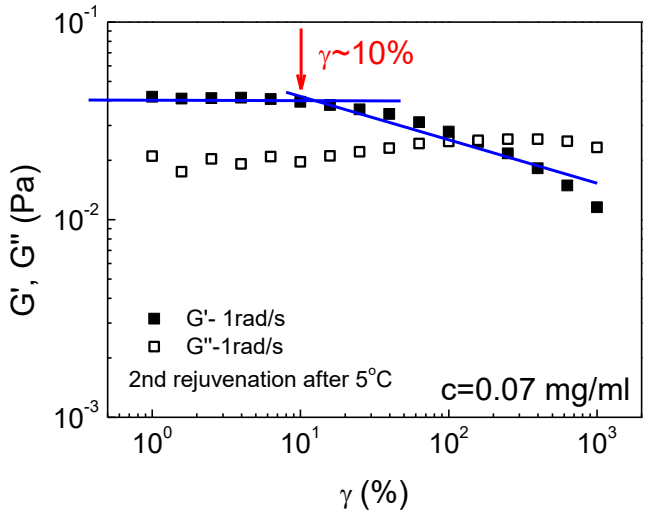

Figure 7.16. Dynamic frequency sweep test at 0.07mg/ml, 20°C and 1rad/s. The two lines show the linear regime of G' and the nonlinear regime. The vertical arrow indicates the strain value at 10% for G' and G''.

Differences in moduli are within experimental error (see part v, figure 7.18, 1st and 2nd rejuvenation) and it is important to highlight that at low concentrations the frequency sweeps (discussed in the next paragraph) exhibit the same behavior (data superimpose) whereas for larger concentrations they differ. This phenomenon can be explained via the time needed for the system to equilibrate while reaching 20°C after cooling (low concentration needs smaller equilibration time after the strain sweep). In our case the waiting time after strain sweep tests was the same and this is the main cause for the observed difference in the moduli.

ii) Stress-strain curve

This is discussed for two concentrations, c=0.07mg/ml and c=3.3mg/ml). The respective elastic moduli extracted from the slope of the linear regime are 0.06Pa and 5.6Pa, the same within experimental error as those extracted from the moduli, e.g. figure 7.16.The stress-strain curve is based on:

$$\sigma = G^*\gamma = \left(\sqrt{G'^2 + G''^2}\right).(\gamma/100) \qquad \text{Eq. 7.1}$$

where σ is the stress, γ is the strain unit, G* is the complex modulus.

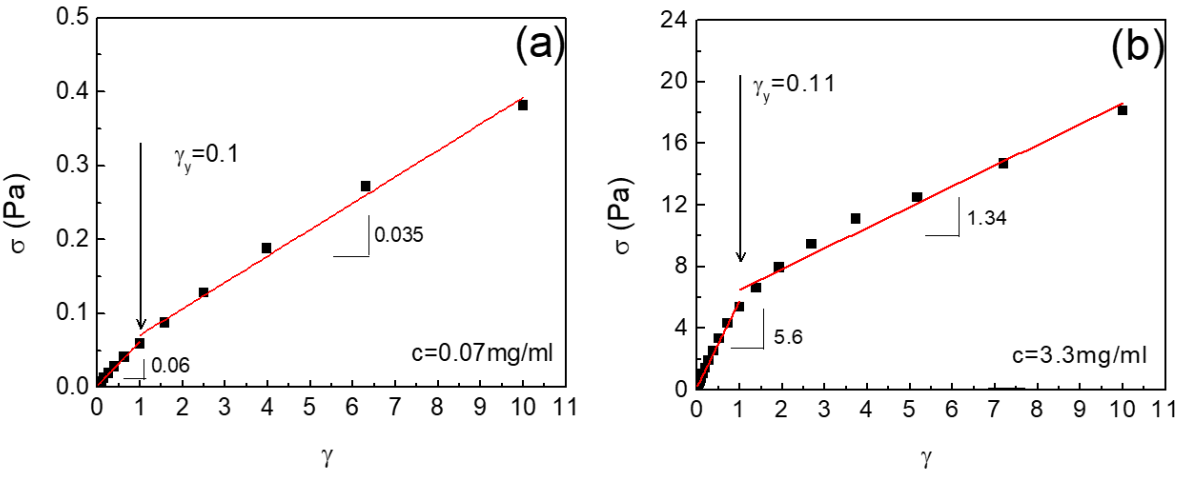

Figure 7.17. Stress-strain curves for two concentrations at 20°C and constant frequency 1rad/s: (a) c=0.07mg/ml with yield strain at 100%; (b) c=3.3mg/ml with yield strain at 110%. The vertical arrow indicates the change in slope, which is assigned to the yield point.

The linear fitting used for both the linear and the nonlinear regime (y=ax+b) and the yield strain up to the slope-change is roughly at 100%. For denser solutions, the change in slope is more pronounced.

iii) Moduli crossover point

The crossover value indicates the exact point beyond which G'' overcomes G' and the system flows (melting point). As already mentioned, for some concentrations this point is not detectable on figure 7.15b.The maximum strain measured was to 1000%.

iv) Maximum of G''

Sometimes the yield strain of a material is associated with the strain at which the G'' exhibits the maximum. The analogy to this is that at the yielding the maximum energy dissipation is expected to take place. In our results, this point is not pronounced and for this reason, we do not use it.

v) Discussion and summary

In this paragraph, we discuss cases (i) and (ii) for the various concentrations. In figure 7.18, we show three sets of data where the full symbols correspond to the nanopure water conditions (salt-free) and the empty symbols to the artificial seawater environment (saline).

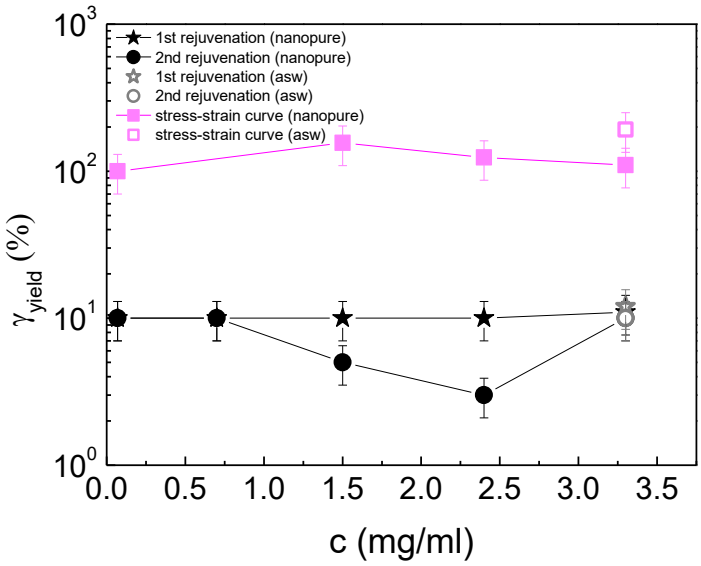

Figure 7.18. Yield strain amplitude (%) against concentration for nanopure (filled symbols) and artificial seawater, ASW (empty symbols) environment. The squares represent the second way of extracting this value (ii), the stars represent the first way (i) and the first rejuvenation; the circles represent the first way (i) and the second rejuvenation.

1st rejuvenation: The yield strain within experimental error takes a value of 10% in the salt-free environment and in a saline environment as well.

2nd rejuvenation: The yield strain at low concentrations is similar to that in comparison to higher ones (10%). The saline environment as before does not significantly affect its yielding value.

Stress-strain curve: In case, (ii) the yield strain seems to be constant as the concentration increases. The two ways (i) and (ii) of extracting yield strain differ by one order of magnitude, but both methods represent a constant yield strain. The constant yield strain values suggest the same characteristic average length scale involved in the system but do not imply that the nature of the gradual yielding process is the same at different concentrations.

Differences in the yield strain in figure 7.18 are attributed to different regions for the estimated yield strain. In case (i) the yield strain corresponds to the onset of nonlinearity whereas in case (ii) the slope change in the stress-strain curve indicates the region already being in the nonlinear regime where system flows. For this reason, γ_{yield} from stress-strain curve is one order of magnitude larger.

7.2.3. Linear viscoelasticity

The mechanical properties of the mucus gel were characterized with SAOS for a better understanding of its viscoelastic response. The experiments were performed in the linear viscoelastic regime with strains below the onset of nonlinearity. We report the flow behavior at different concentrations and we show the effect of temperature (5ºC and 20ºC).

7.2.3.1. Dynamic frequency sweep test (DFST)

In figure 7.19 we depict the behavior of the gel-like mucus for different angular frequencies for a constant strain amplitude (10%) for two concentrations. The plot on the left, figure 7.19a, indicates the lowest concentration (c=0.07mg/ml) and the data superimpose for the two different temperatures; moduli do not depend on temperature in this case. The plot on the right, figure 7.19b, indicates an intermediate concentration (c=1.5mg/ml) where the viscoelastic behavior deviates (stronger gel) when the temperature decreases; moduli depend on temperature.

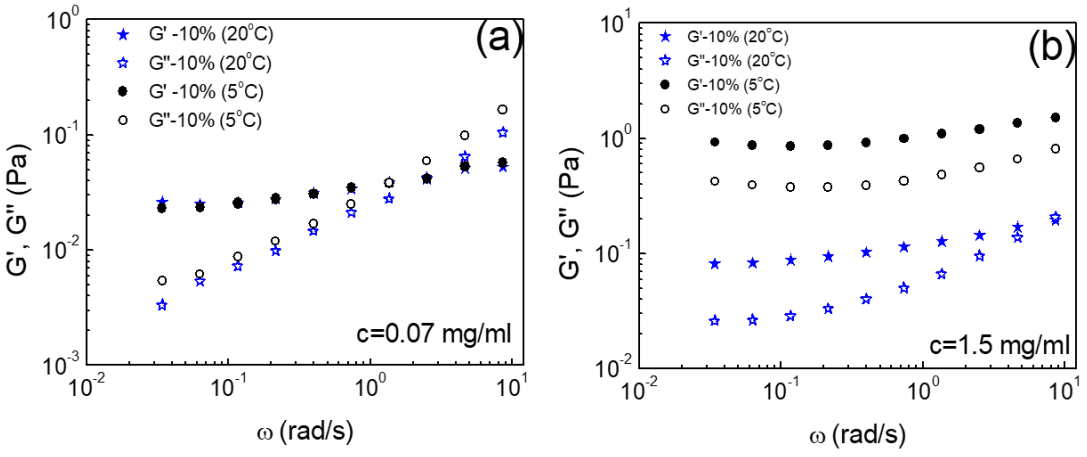

Figure 7.19. Dynamic frequency sweep experiments at a constant strain amplitude of 10% for 5ºC (black cycles) and 20ºC (blue stars): (a) low concentration c=0.07mg/ml; (b) intermediate concentration, c=1.5mg/ml.

To explain this distinct behavior at different concentrations, we propose a hypothesis based on the natural environment of mucins. Hagfish slime (mucin and thread proteins) has a natural concentration up to c=0.01 wt.% [11] and the amount of mucins in the whole slime is c=0.02mg/ml [44]. In the present work, we deal with higher concentrations in comparison to the natural ones. Our findings may indicate

that as soon as we increase the amount of mucins and concomitantly reduce the temperature (to mimic seawater), the formed the network has a complicated structure (dense and interpenetrating, which we call stronger) even in presence of electrostatic interactions where mucins repel each other. The overlap concentration determined with DLS is c_e=0.2mg/ml (chapter 6) with protocol A instead of B used for shear experiments.

At low concentrations (dilute mucus, below c_e), it seems that the temperature variation is not enough to change the microstructure and consequently the rheological response (figure 7.19a). On the other hand, at high concentrations the modulus increases with decreasing temperature. Above c_e (figure 7.19b) the plateau modulus reflects interactions which dominate the mucins network (entanglement regime).

An additional effect, that of salt on the mucus is shown in figure 7.20 for two similar concentrations (c=3.3mg/ml) in salt-free and in a saline environment, respectively. Measurements were performed in the linear viscoelastic regime (strains of 2%, nanopure and 10%, artificial seawater). The addition of salt in mucus decreases the elastic plateau modulus due to the electrostatic screening (changes the configuration of the chain).

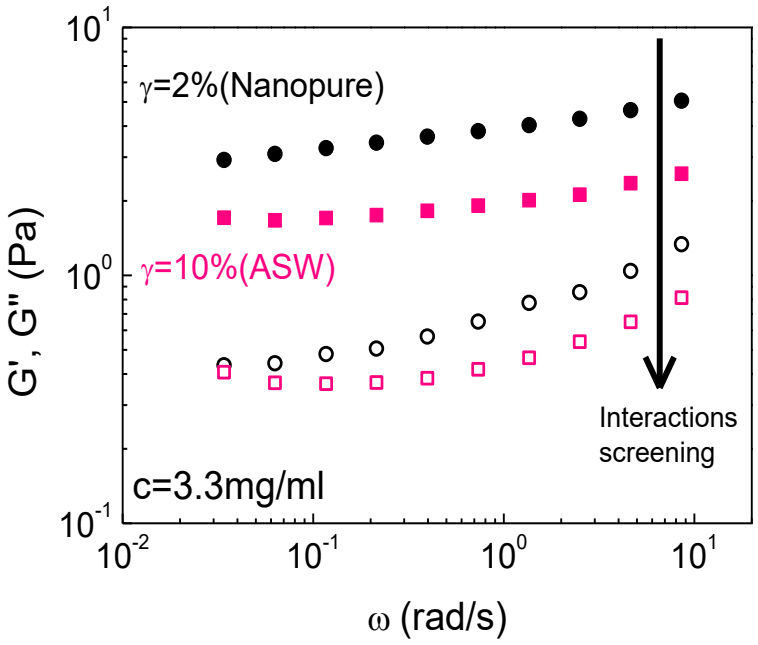

Figure 7.20. Dynamic frequency sweep experiments at strain of 10% for the saline environment and 2% for the salt-free environment, and temperature of 20°C. The vertical arrow indicates the direction of screening of the interactions.

The value of the elastic modulus in ASW is about 2Pa, in agreement with the findings from CABER. In case of ions-free environment mucins seem to promote stronger repulsions, yielding larger modulus. Three remaining questions are: i) Being strong polyelectrolytes due to the dense charged groups within the polymer chain, how are mucin protein able to create this physical network?; ii) How do the charges change the conformation of the chains and correspondingly the hydrogel (e.g. how do strong repulsive chains overlap)?; iii) what is the role of temperature?

7.2.3.2. Creep and recovery

Creep experiments were performed in order to extend the linear viscoelastic regime to lower frequencies. The creep compliance, J(t), was measured. Recovery tests followed the creeps in order to assess the relaxation of the sample. The main idea of such tests is illustrated in figure 7.21 and explained in a simple way. In this type of experiments, the strain is monitored as a function of time while a constant stress (e.g. here 0.2Pa) is applied for a certain amount of time (e.g. 300s). The ratio of the time-dependent strain to the applied constant stress defines the shear creep compliance, J(t). The creep compliance is the inverse of the relaxation modulus G(t).

$$J(t) = \frac{\gamma(t)}{\sigma} = \frac{1}{G(t)} \qquad \text{Eq. 7.2}$$

The measured compliance through appropriate conversion of the data yields the elastic and the viscous moduli shown in figure 7.22a. We do not focus on details of this method which can be found in reference [95], [96].

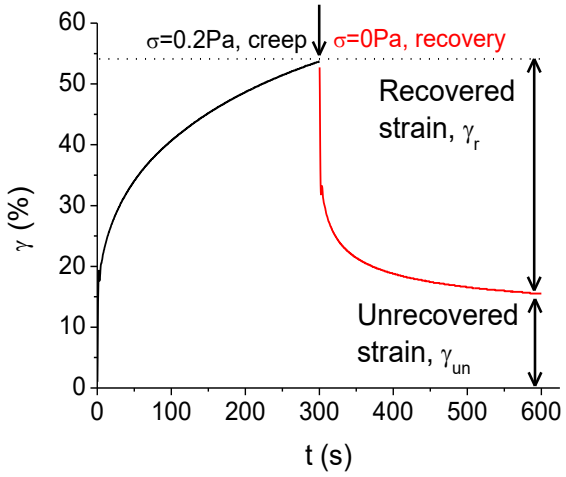

Figure 7.21. Typical creep and recovery test in terms of strain (%) against time.

The stress is chosen from strain sweep test (DSS). More precisely, below the onset of the nonlinearity a strain is selected and it is multiplied with the corresponding modulus. This stress value is the maximum one for using within the range of the linear regime. Two major parameters were tested: i) the flow behavior at very long times and ii) the recovery at fast creep-recovery tests.

i) Flow behavior (long time creep)

As discussed above, mucus is a very soft and elastic biomaterial where the elastic contribution is always large. At very high concentrations of mucins (example here) G' exhibits a plateau. In this respect, the absence of detectable low-frequency crossover makes it be very interesting to be examined under creep over long time. In the step stress measurement (creep) of c=3.3mg/ml at T=20^{o}C, a stress of σ=0.2Pa was applied for a certain time (here 21h). Evaporation was not a concern, as discussed (figure 7.13). Below, in figure 7.22a the extent of linear regime indicates that hagfish mucins seem to start to flow at ω=10^{-5}rad/s or about 21h, the duration of the test. The sample exhibits a behavior similar to that of colloidal glass or strong gel. It shows a plateau value for the elastic contribution, which is the signature of a

physical network and a minimum in the viscous contribution, which could be, attributed to caged situation of interacting mucin proteins. This is the evidence, which makes this hagfish mucins being very challenging: a very weak hydrogel with slow terminal flow.

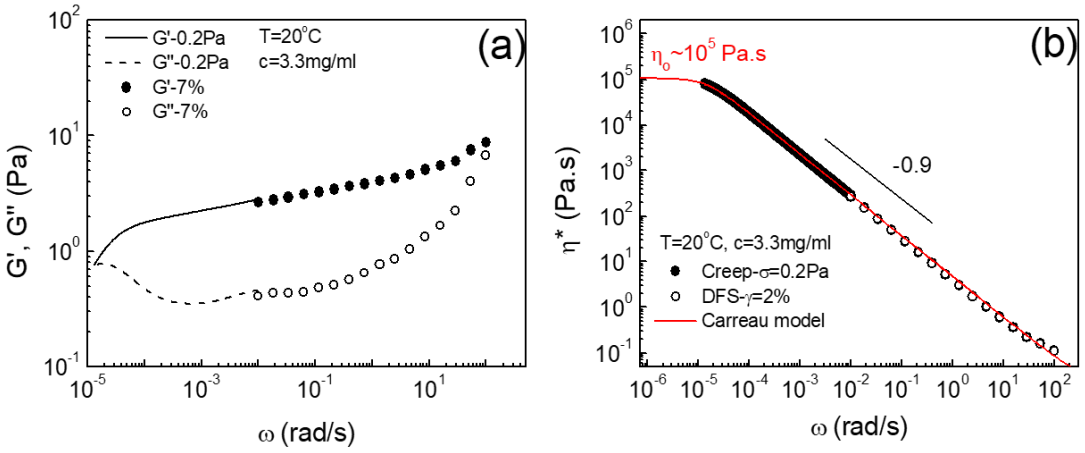

Figure 7.22. Creep experiment in the linear regime at 20°C for a high concentration of 3.3mg/ml: (a) G' and G'' against frequency; (b) complex viscosity against frequency. Full symbols: G', empty symbols: G'', line: G' from creep, dashed line: G'' from creep and red line: Carreau empirical fitting of the data.

The complex viscosity in figure 7.22b was obtained from:

$$|\eta^*| = \sqrt{\left(\frac{G''}{\omega}\right)^2 + \left(\frac{G'}{\omega}\right)^2} \qquad \text{Eq. 7.3}$$

in order to extract the zero shear viscosity value, we used the empirical fitting of Carreau [97]:

$$\eta^* = \eta_\infty + \frac{\eta_o - \eta_\infty}{[1 + (\lambda_c \omega)^2]^N} \qquad \text{Eq. 7.4}$$

where η^* is the complex viscosity, η_∞ is the infinite viscosity, η_o is the zero shear viscosity, λ_c shows the time constants related to the polymer relaxation times and N is a dimensionless exponent. By using this model, we determined the zero-shear viscosity (10^5Pa.s).

ii) Creep-recovery test

Two different constant stresses were applied, σ=0.2Pa and σ=0.5Pa (both in the linear regime) for 300s. The stress was then removed and the recovered strain was

measured for 300s. Figure 7.23 depicts a typical example of an intermediate concentration of mucin, 1.5mg/ml. The resulting strain of mucus was increased once the stress applied was higher. It seems that the recovery is fast and within the range of 300s the sample approaches to reach a constant strain.

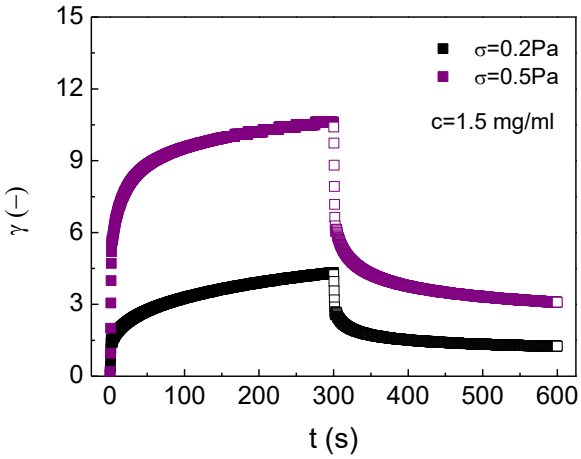

Figure 7.23. Strain (%) against time for two different stresses: σ=0.2Pa, σ=0.5Pa for an intermediate concentration of c=1.5mg/ml at T=20°C. Both creep and recovery is shown.

Based on figure 7.21, we estimated the recovered (γ_r) and unrecovered (γ_{un}) strains for an initially (t<0) applied stress of 0.2Pa at 20°C and results are shown in figure 7.24. The former is within error at 10%. The latter varies in a more pronounced way with concentration, starting from 1000% and reaching less than 1% (we do not consider the blue box which is artificial seawater environment). The very large unrecovered strain (1000%) at low concentration identifies the predominantly liquid-like behavior. When the concentration increases, the value of the unrecovered strain reduces to ~1% due to the increase in modulus (more elastic).

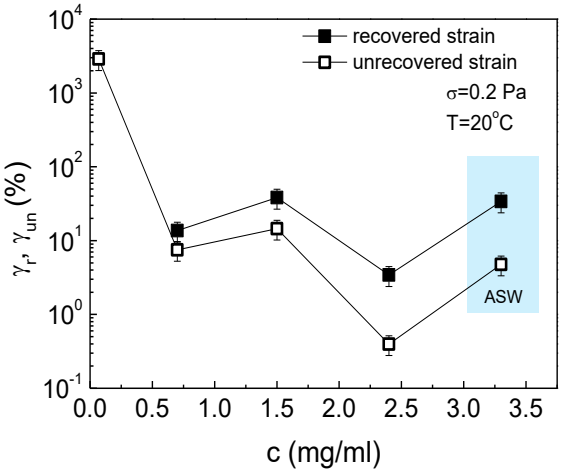

Figure 7.24. Recovered and unrecovered strain against mucin concentration for stress of 0.2Pa (at time t<0) and T=20°C.

7.2.4. Impact of concentration

Many parameters affect the viscoelasticity of polyelectrolytes such as charges, chain conformation and concentration. We are particularly interested in mucin concentration effects. In figure 7.25 both extensional and shear data are plotted against mucus concentration. The red circles represent the extensional apparent modulus (extracted from eq. 3.12) while the black squares the elastic modulus measured at ω=0.1rad/s. The line is a power-law fit ($G=a.c^k$) with an exponent k=0.5. The two dashed lines highlight two important concentrations: i) c=0.2mg/ml which is the critical concentration (c*) estimated from DLS and ii) c=2.4mg/ml where the modulus deviates from linearity and rapidly increases. The point included in the blue box is the measured modulus in saline artificial seawater environment.

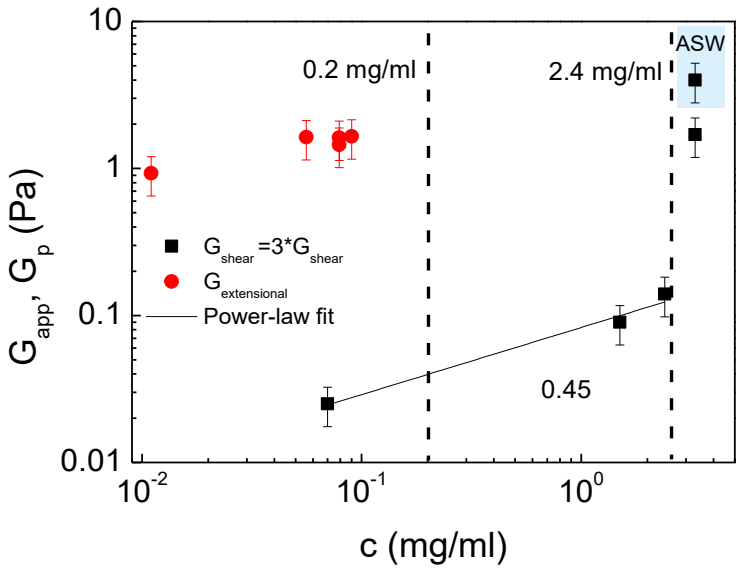

Figure 7.25. Apparent (in extension) and elastic (in shear) plateau modulus as function of mucin concentration. Circles represent the extensional data and squares the shear rheological data. The point in the blue box reflects the artificial seawater environment. The power-law fit gives an exponent of 0.45

The range of the measured moduli from both techniques is 0.01<G<10 Pa which is expected for such biomaterials (table 7.2). They have different values and we attribute this variation due to the following points:

i) The sample preparation was not the same, extensional data originate from protocol A and shear data originate from protocol B. This means that in the first case a few counterions were present due to the buffer solution, whereas in the latter case there was absence of ions.

ii) The two techniques have different origin with respect to the type of flow. In CABER, chains are stretched (nonlinear flow) for a certain amount of time in the vertical direction (coil to stretch transition) and in shear chains are deformed at different strains and at various frequencies in the linear regime, i.e., they remain in equilibrium. The latter experiments gives the elastic plateau modulus. The former determines the thinning of diameter and the respective time is analyzed with a Maxwell-type of model, by invoking an apparent modulus which should relate to the elastic plateau modulus.

Further, we show in figure 7.26 the loss angle, tanδ=G''/G' as function of frequency for the various concentrations. The point at which this curve exhibits a minimum was used to define the elastic plateau modulus G' (0.1rad/s, vertical arrow).

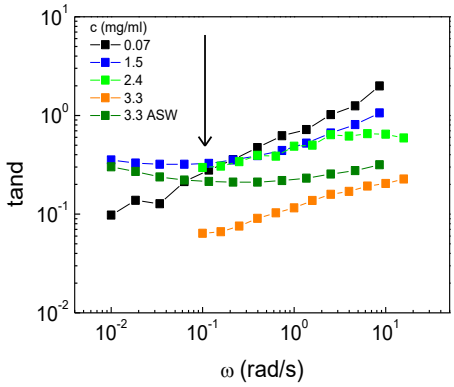

Figure 7.26. Tanδ against frequency ω for different mucin concentrations. The vertical arrow indicates the 0.1rad/s frequency at the minimum tanδ value, used to extract the plateau modulus.

Equivalently, the plateau modulus can be extracted graphically when data allow, as shown in figure 7.27a. In figure 7.27b we present the data extracted in this way. The data follow the trend which is represented in figure 7.25 where the moduli was extracted from the minimum of tand (ω=0.1rad/s).

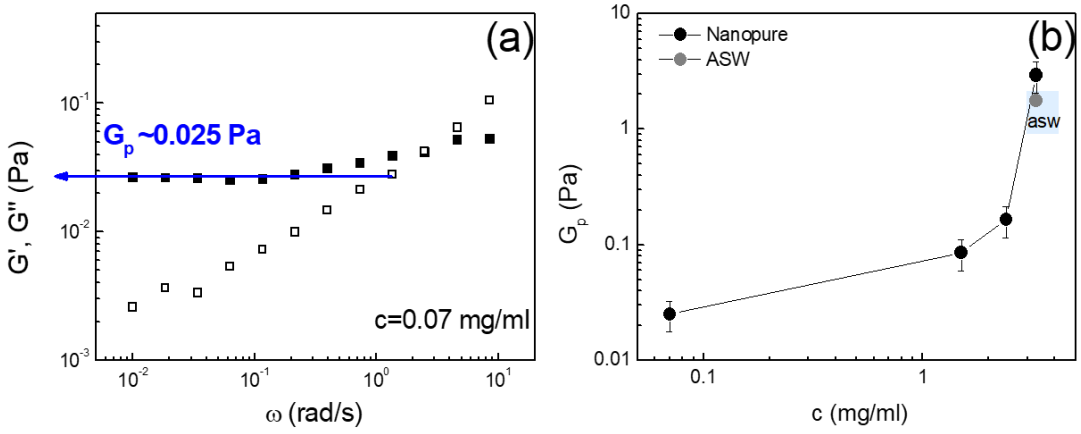

Figure 7.27. (a) Elastic and viscous moduli against angular frequency for a low concentration of 0.07mg/ml. The horizontal arrow indicates the estimated plateau value, G_p=0.025Pa; (b) G_p against mucin concentration in salt free environment and in the blue box we represent the saline artificial seawater measured point.

7.3. Discussion and summary

The strong increase of the elastic modulus at high concentrations of mucus suggests that the gel is resistant to shear deformation. Above the critical concentration of c=2.4mg/ml (second dashed line in figure 7.25) we have a signature of a transition. For this transition to be well-established, more concentrations need to be measured in the future. The change in slope could be connected to some extend with the regime deeply within mucin entanglements, and certainly reflects the mucin network properties. Based on our DLS measurements, above a concentration of c_e=0.2mg/ml we are deeply into the semidilute regime and mucins are interacting topologically (entanglement region).

A challenging point is that of understanding the reason why, based on the extracted values of the apparent modulus, mucins below c_e=0.2mg/ml appear to create a stronger network in extension in comparison to linear shear rheology (figure 7.25). Besides the two points listed above, another explanation calls for the role of charges. As already mentioned, the samples used in extensional measurements contain some charges due to the buffer solution. These charges are mainly sulfonate groups of mucins (SO^{3-}) which play the role of counterions. We conjecture that mucins are better associated in this way (in comparison to a totally salt-free environment in the case of DFS tests) and this results in the difference in moduli.

At this point, a number of open questions exists. Many parameters, functionalities and properties are unknown on such hagfish mucins. The ways by which mucins associate and relate the microscopic properties (investigated via DLS) and bulk properties (extensional and shear rheology) remain unresolved. However, the effects of charges (due to the difference in the sample preparation protocols) in the macroscopic view seem to have a strong influence on mucus. This is in contrast to the microscopic structure discussed in chapter 6. Our finding based on diffusion data suggest that internal chain configurations are not appreciably affected by the presence of a heavily saline environment.

In the case of extension, the presence of buffer ions seems to lead to larger modulus even at lower concentration, in comparison to salt-free environment in shear. Instead, in the case of shear the presence of buffer ions seems to collapse the

structure to the degree that we are not able to detect viscoelasticity. The structure becomes like water within seconds-minutes. When mucins appear in ASW, both the extensional and shear rheology provide the same modulus, G~2Pa. For all systems, the electrostatic screening effects take place but the strength of the interactions differs.

The different origin of ions affects the attraction strength (e.g. role of Ca^{2+} discussed for ability to create physical better associations in comparison to Mg^{2+}), they have different functionalities which are discussed extensively in [43]. In order to facilitate the key findings from the above discussion, we built a summary table 7.3., where we list the parameters affecting the mucus properties: sample preparation protocol which translated to ions in solution, origin of ions and mucins concentration.

Table 7.3. Summary of shear, extension and DLS findings: roles of ions, modulus and mucin concentration.

Ions	Shear	Extension	DLS
Buffer (protocol A)	Torque issues (structure collapses)	G_{app}~1Pa (below c*=0.2mg/ml)	Ergodic
Artificial seawater	G'~2Pa (highest concentration, 3.3mg/ml)	G'~2Pa (at 100% ASW) and decreases with ASW concentration	Ergodic (same diffusion as in presence only of buffer ions)
Salt free (protocol B)	G'~0.025Pa (lowest concentration 0.07mg/ml) G'~4Pa (highest concentration, 3.3mg/ml)	Did not tested (future work)	Non-ergodic

Chapter 8: Conclusions and Outlook

In this chapter, we try to provide general picture emerging from this thesis with some perspectives. The three main techniques utilized are listed in figure 8.1, where we summarized the major observables and findings. Light scattering provides microscopic details such as the diffusion dynamics and the structure of the measured object (here both PNIPAM colloidal microgels and mucins glycoproteins in water).Shear and extensional rheology reveal the bulk properties. Under shear flow both colloids and biopolymers were measured in linear and nonlinear regime at different concentrations. Under extensional flow only the biological hydrogel was investigated, in order to test the thinning of the filament under various concentrations and salts.

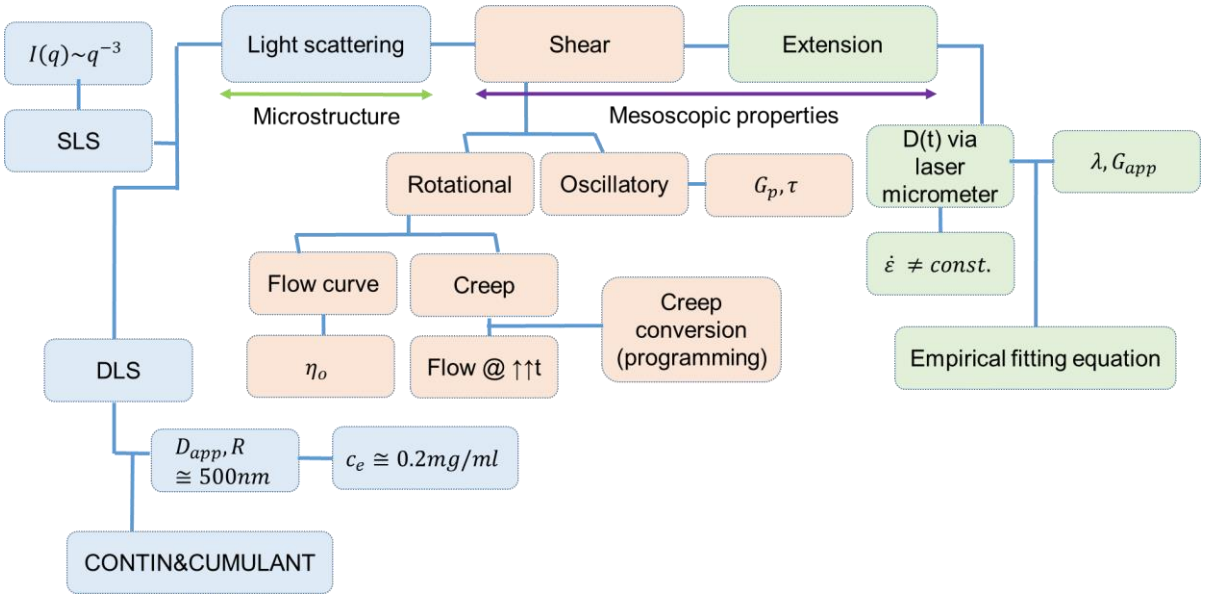

Figure 8.1. Summary illustration diagram about light scattering (blue boxes), shear rheology (red boxes) and extension (green boxes).

We extensively discussed and explained the phenomena observed. Here, we summarize our interpretations and briefly describe the work in progress and possible future directions.

Colloidal microgel particles: We tried to understand if we can control the rheology of the same material at the same volume fraction achieved by independent variation of concentration and temperature. This could be helpful practically for instance in terms of economy; less material at lower temperature but same properties. Moreover, it may provide insights into the understanding of glass and jamming transitions in soft

particles. At very large concentrations, the concentration-temperature equivalence (in terms of reaching the same volume fraction) becomes complicated and invalid because the shrinkage of the particles dominates. As discussed in chapter 5 in scientific terms, in the glassy regime, properties are the same at the same volume fraction reached by two different paths while in the jammed regime this is not the case. Two things are important to note here: i) the need of a new parameter, for example a shrinkage parameter that will provide much help in order to reach same properties even at very large concentrations by using a proper scaling; ii) the need for more experiments over a wider range of concentrations in the jamming regime in order to gain information for the jamming regime. The first (i) can be materialized via measurements of particle elasticity and the latter (ii) one with rheometry.

Biological mucus hydrogel: Mucus systems are biological systems with different functionalities by means of their structural characteristics. The two major characteristics are the i) protection and lubrication in human organs and ii) the defense mechanism in hagfishes. Here, we focused on the latter (ii) and by using the one of the two components of hagfish slime we tried to understand its crucial role in slime functionality. Mucin glycoproteins being the second component, provide a very challenging system under investigation, because of their unknown properties and the need to comprehension the mechanisms provided by the Mother Nature.

Figure 8.2 illustrates the hagfish slime which becomes secreted upon hagfish attack from a predator. The cartoon shows the simplified network structure, the microscope image which provides details about the size and the shape of the initial structure of slime and the last picture shows how the slime is in the reality.

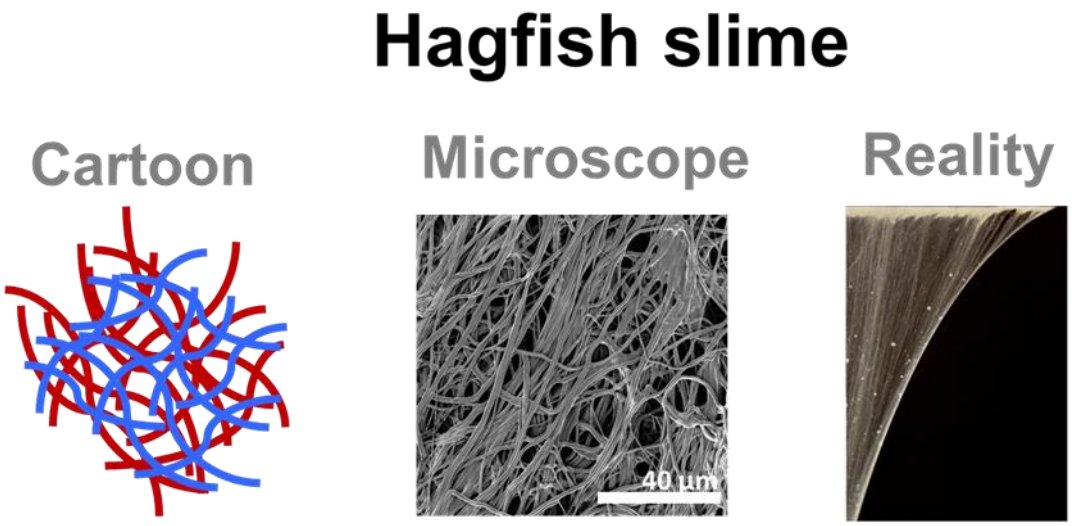

Figure 8.2. Hagfish slime: i) cartoon representation; ii) microscope image and iii) true slime.

In figure 8.3, we show the two components separately, in order to briefly summarize the hagfish slime behavior. The dynamics of mucin glycoproteins were investigated and based on the results we provide a hypothesis for the biological implications on the action of such bioinspired materials.

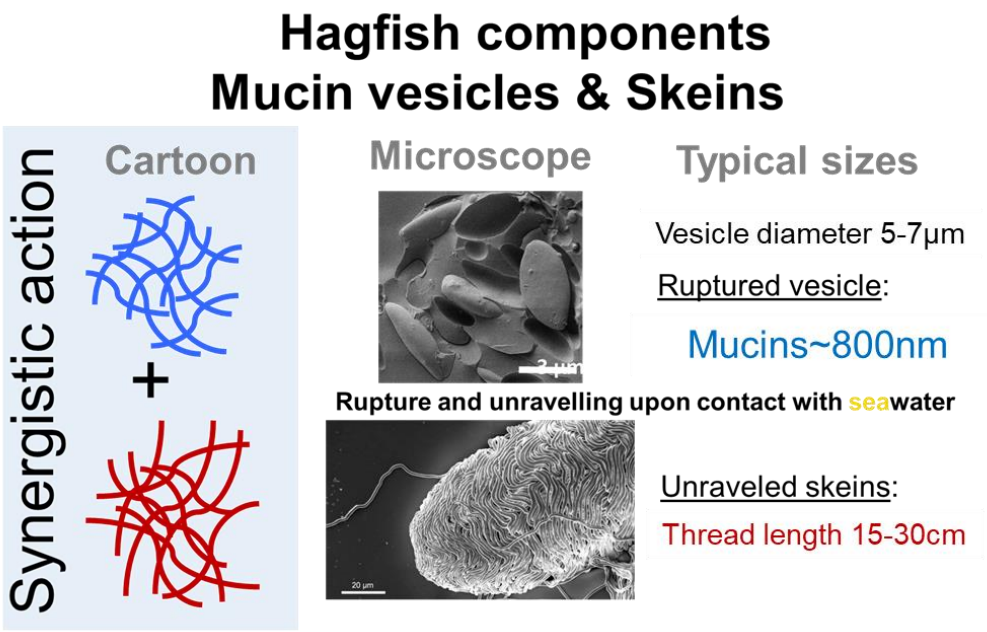

Figure 8.3. Hagfish slime components: mucin vesicles and skeins; cartoon representation, microscope images and typical sizes. Microscope images provided by L. Böni.

Hagfish slime is a cohesive and stiff network with very weak viscoelastic properties (modulus of about 0.01Pa). The cohesiveness is provided by threads made of

intermediate filaments[98] which constitute a flexible network whereas the viscoelasticity originates from mucin proteins. The natural concentration in seawater which makes this network functional (for the defense mechanism) is about 0.02mg/ml as shown in the table in figure 8.4a (the light red row) [13].

The diffusion dynamics suggests an entanglement concentration of mucin: $c_e \approx 0.2$mg/ml. The special properties of slime (in the presence of threads) in natural conditions are due to mucins at 0.02mg/ml, whereas in the absence of threads the network exhibits these properties at much higher concentration $c_e = 0.2$mg/ml (figure 8.4b). The biological implication is that of a super economic material. The fiber network enables functional properties at much lower concentrations, below the entanglement concentration of mucin alone.

Source	[Mucin] (mg ml^{-1})	Reference
Hagfish slime	0.02	This study
Gastric mucus	47	Sellers and Allen, 1989
Duodenal mucus	38	Sellers and Allen, 1989
Colon mucus	20	Sellers and Allen, 1989
Slug pedal mucus	1–32	Denny, 1979
Human salivary mucus	14	Veerman et al., 1989
Human gastric mucus	30	Pain, 1980

(a) NATURE

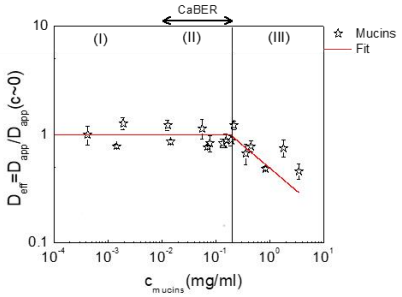

(b) "MIMIC" NATURE

Figure 8.4. (a) Table with concentration of mucins for various origin secretion, taken from [13]; (b) Apparent diffusion coefficient normalized with the apparent diffusion coefficient when c→0 against mucin concentration.

Another important point which has to be highlighted concerns the sample preparation and the influence on its dynamic properties. In paragraph 7.2.1 we showed and compared the two ways of sample preparation, protocols A and B. Dialyzed samples (protocol B) were measured by means of shear rheology and non-dialyzed samples (protocol A) by means of light scattering and extensional rheology. The dynamic structure of dialyzed samples by DLS is summarized in the graphs shown below (figure 8.5).

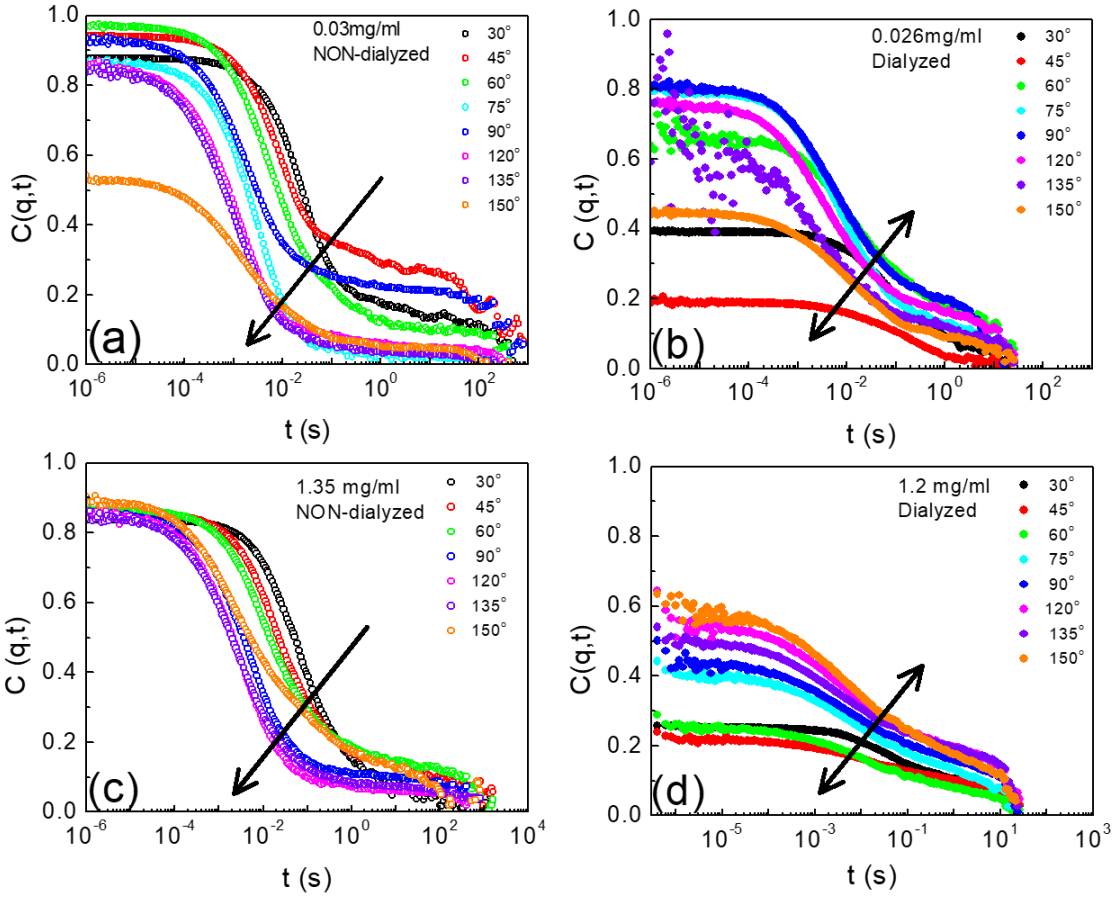

Figure 8.5. Intermediate scattering functions at different concentrations measured with two protocols (non-dialyzed: protocol A and dialyzed: protocol B; (a,b) concentrations in the beginning of the entanglement regime; (c,d) concentrations deeply into the entanglement regime. The arrows show the increase of the scattering angle and the double arrow indicates the absence of consistent trend with scattering angle variation.

It is crucial to note that more measurements and different concentrations have to be performed in order to establish or not the observed trends, listed below:

-dialyzed/protocol B= no counterions present= strong repulsive network=seems to be non-ergodic

-non-dialyzed/protocol A=counterions present= “smooth” dynamics (largest C(q,t) at short times, trend with scattering angle) due to the counter balance of the interactions=screening=seems to be ergodic

-a small amount of buffer added to the non-dialyzed seems to “smoothen” the C(q,t) and the dynamics-this phenomenon is shown in figure 8.6. Starting from protocol B

we tried to mimic protocol A by adding small amounts of salts. The reduction of the non-ergodicity seems linked to buffer ions

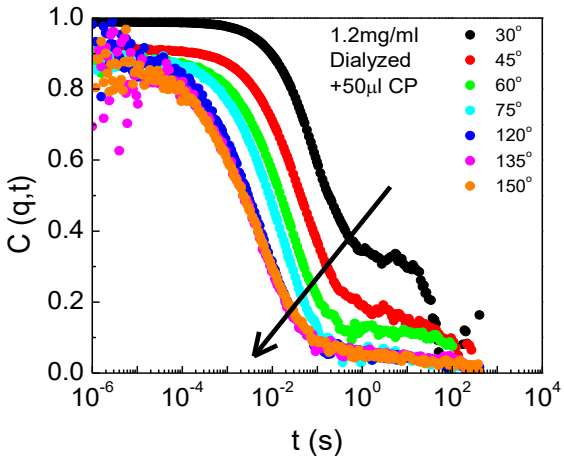

Figure 8.6. Intermediate scattering function at a concentration of 1.2mg/ml where the sample is dialyzed and small amount of buffer (50μl) was added to reduce non-ergodicity. The arrow indicates the decrease of the fast dynamics.

To complement to above discussion, techniques such as fluorescence microscopy, cryo-TEM, cryo-SEM, AFM could provide further insights. For instance, images of samples prepared with the two different protocols or images of the dialyzed samples (e.g. sample in figure 8.5) before and after the addition of buffer solution (figure 8.6). Concerning figures 8.5 and 8.6, the multi-speckle dynamic light scattering (MSDLS) is the most reliable approach for measuring non-ergodic systems; density fluctuations are frozen and the dynamics are slow. In such a case modification of the standard DLS setup by replacing the photomultiplier tube by a charge-coupled device (CCD) camera is necessary. A systematic work on the slow mode could provide information about mucin dynamics.

Microrheology also could provide an additional tool for studying the rheological response of mucus. A comparison with oscillatory shear rheological data would be important. A very recent work of Chaudhary et al. [15] discusses the modulus (G') dependence concentration for various biomaterials. Especially, for hagfish slime the power law dependence for the linear viscoelasticity is $\mathbf{G'\sim c^{1.12}}$.In our case (figure 7.25) the moduli has a power law dependence of 0.5 with concentration, $\mathbf{G'\sim c^{0.5}}$. We have to highlight here that in the case of hagfish slime (table 8.1) there is the presence of threads plus mucins whereas in our investigation there is only the

presence of mucins. This could be a possible explanation for the k power-law exponent (with concentration) difference shown between the hagfish slime and the isolated mucin proteins.

Table 8.1. Biomaterials and the concentration dependence of modulus $G' \sim c^k$. Taken from [15].

Material	k
Semiflexible networks [33,34]	2–2.5
Methylcellulose [35]	2.27
Hagfish gel	**1.1**
Desmin [36]	0.71
Vimentin [36]	0.48
Human Keratin K8/K18 [37]	0.53

A more general and fundamental question stemming from this work is how do the remarkable properties of the present biomaterials (structure as well as bulk dynamics) fit into the complex landscape of polyelectrolytes? How can the available models which explain polyelectrolyte dynamics provide a way to understand the complex behavior of mucins (from different origin and ill-defined) which leads to interesting properties? Novel applications can emerge from mucus systems and especially from hagfish slime (very economic as referred above) in order to improve the efficiency and to make the final product cheaper. Hence, there is lots of excitement in this field of research.

As a final perspective of this thesis, we wish to share a very interesting and attractive work from the Naval Surface Warfare Center Panama City Division (NSWC PCD). They succeeded in reforming the hagfish slime for military purposes. More details about this impressive discovery presented in an article which is available in:

https://www.ibtimes.co.in/us-navy-creates-hagfish-inspired-military-grade-slime-trap-enemy-boats-water-778206

Appendix I: PNIPAM microgel particles

Effective volume fraction determination

The volume fraction of PNIPAM colloidal microgels is similar based on the simplistic calculation shown in chapter 5. The whole results discussed in respect to mass concentration because the exact volume fraction did not determined. A way to estimate the volume fraction is illustrated below and we briefly explain the procedure. We need more concentrations to be measured for the calculation of the effective volume fraction, φ_{eff}, in the following figure 1, we show the Batchelor fitting which provides the information.

$$\frac{\eta}{\eta_o} = 2.5\varphi_{eff} + 5.9\varphi_{eff}^2 \qquad \text{Eq. 1}$$

Where η is the viscosity of the system, η_o is the viscosity of the solvent and $\varphi_{eff}=kc$ where k is a proportionality constant and c is the solution concentration.

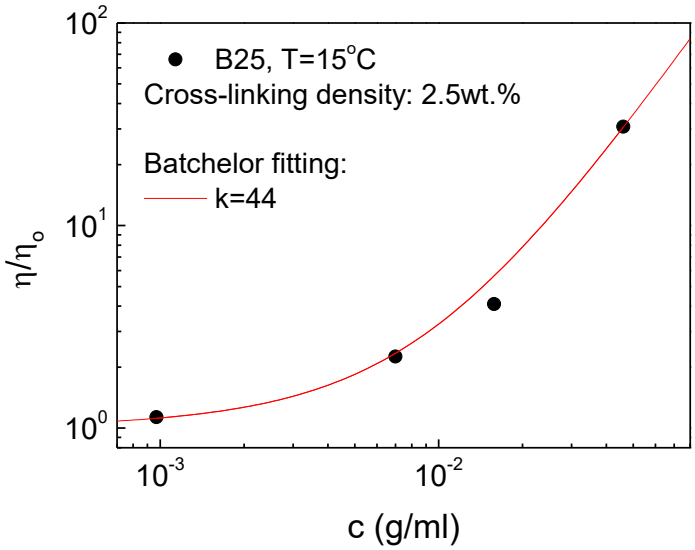

Figure 1. Apparent viscosity against PNIPAM solution concentration, data fitted with Bachelor equation.

In the table below, we present the values of φ_{eff} for T=15°C for k=44.

Table 1. Concentration of PNIPAM solution with the corresponding volume fraction for k=44 (Batchelor fitting).

Concentration (g/ml)	Volume Fraction (-)
$9.78*10^{-4}$	0.043
0.00696	0.3
0.0158	0.7
0.046	2

By using k value for the apparent and qualitative estimation (due to the little amount of concentrations measured in the viscometer) we show another table with the volume fractions at T=15ºC. More measurements and also at different temperatures are required for a well-establish φ_{eff} value.

Table 2. Concentrations (measured in rheology) and the corresponding volume fraction for k=44 at T=15ºC. The bold values correspond to the comparison in figures 5.9 and 5.10.

Concentration (wt. %)	Volume Fraction (-)
6	2.64
6.8	**3.08**
8.2	**3.52**
9	3.96
10	**4.4**
12.3	**5.41**
17	7.48

Since particles are electrostatically stabilized, they have charged on their surface.

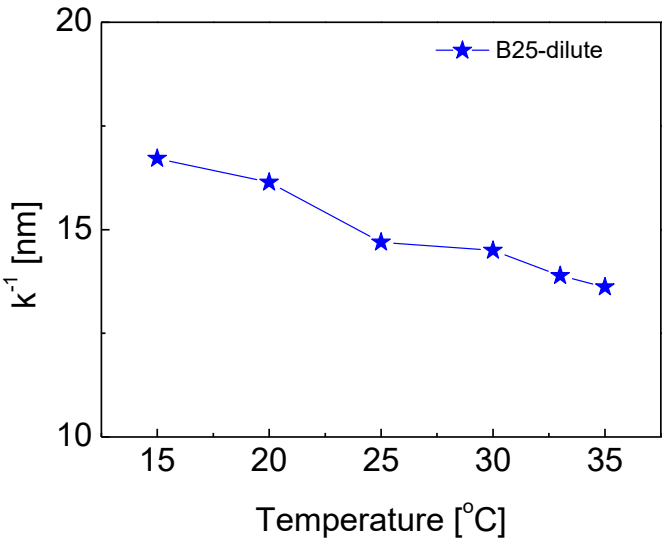

Figure 2. Debye length k^{-1} of PNIPAM microgel particles against different temperatures.

Appendix II: Hagfish mucins

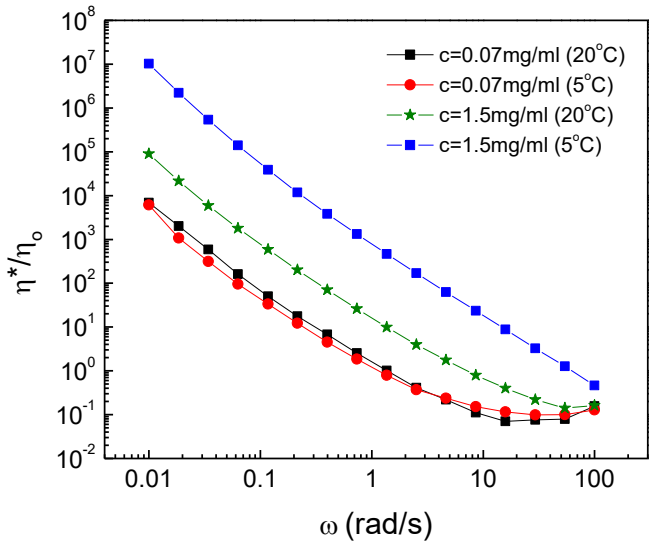

Figure 3. Apparent viscosity (η^* is the complex viscosity and η_o is the solvent viscosity) against frequency for two temperatures, 5°C and 20°C for two concentrations (low: 0.07mg/ml and intermediate: 1.5mg/ml)

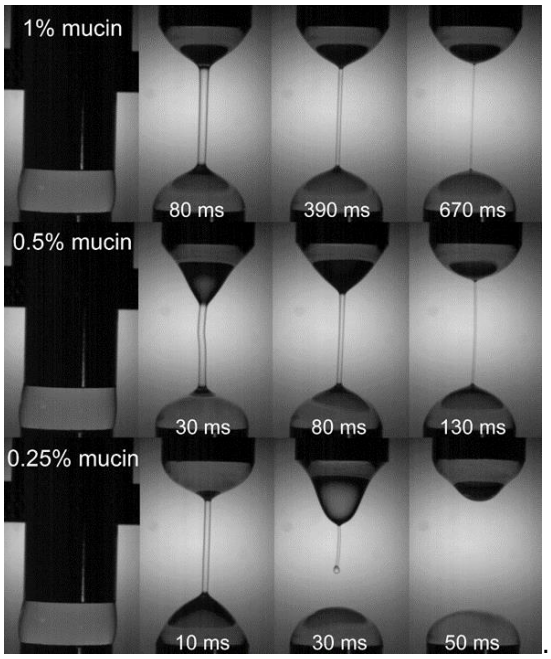

Figure 4. Hagfish mucins in CABER at different concentrations (0.25%, 0.5% and 1%).

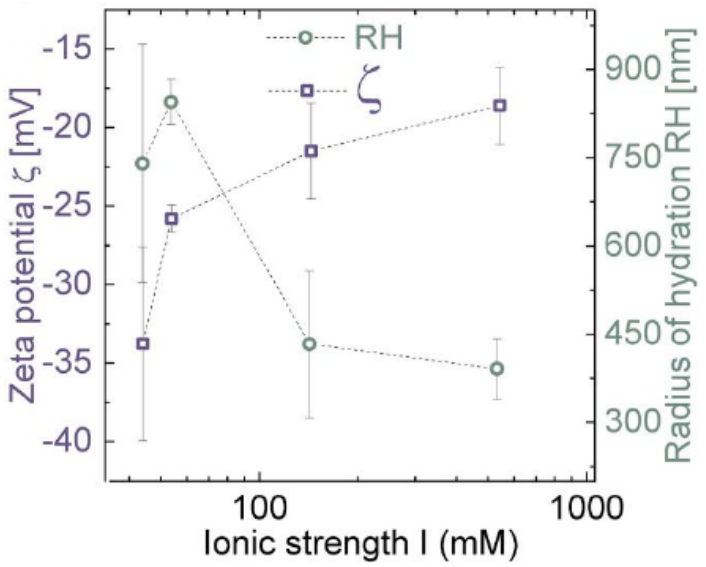

Figure 5. Zeta potential and hydrodynamic radius of hagfish mucins as the ionic strength increases. Measurements performed from L. Böni.

The following figures show DLS data based on NLCA analysis (eq. 6.6).

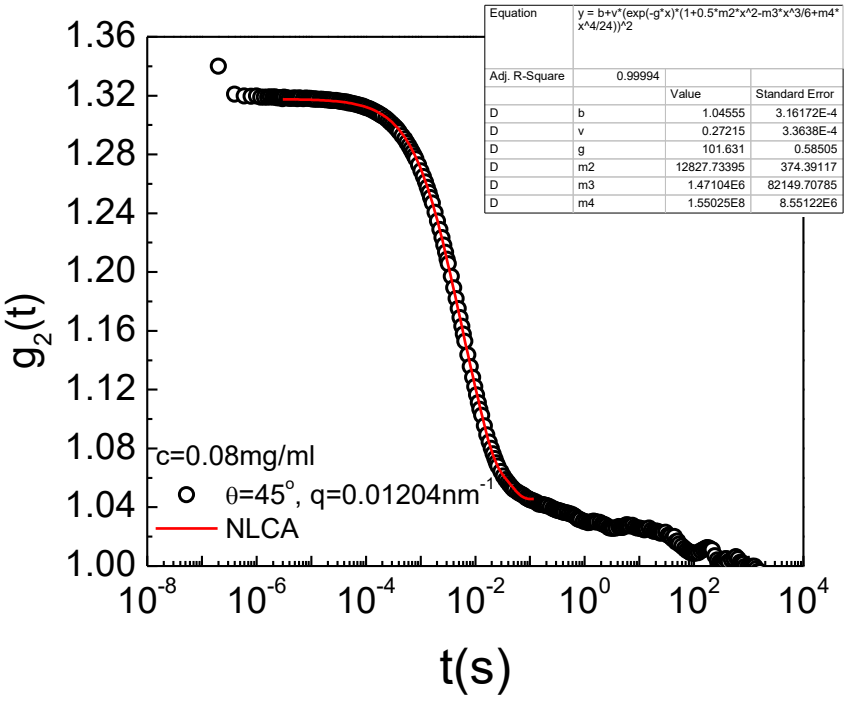

Figure 6. Typical example of a correlation function analyzed with NLCA. The red curve indicates the fitting of the data and in the table we show all the fitting details.

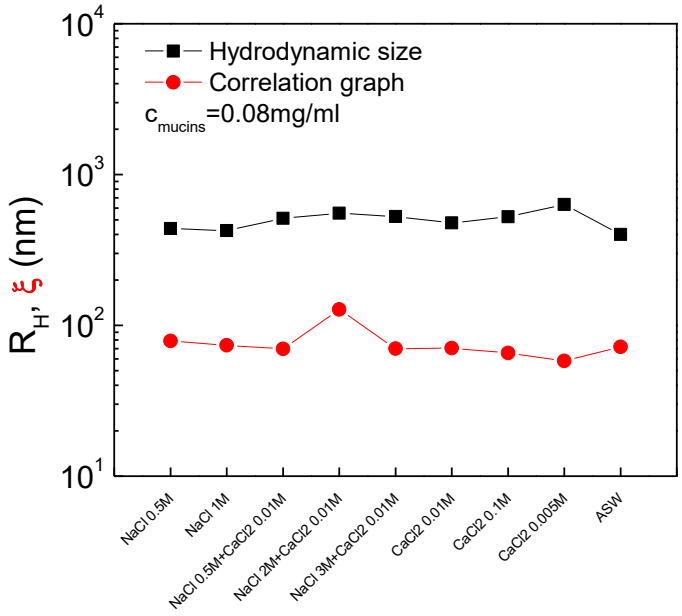

Figure 7. Dynamic and static apparent sizes of mucin molecules plotted for various salt concentrations for a reference concentration of c=0.08mg/ml. We note that the variability of salts and their ionic strength do not affect the present sizes at 0.2mg/ml

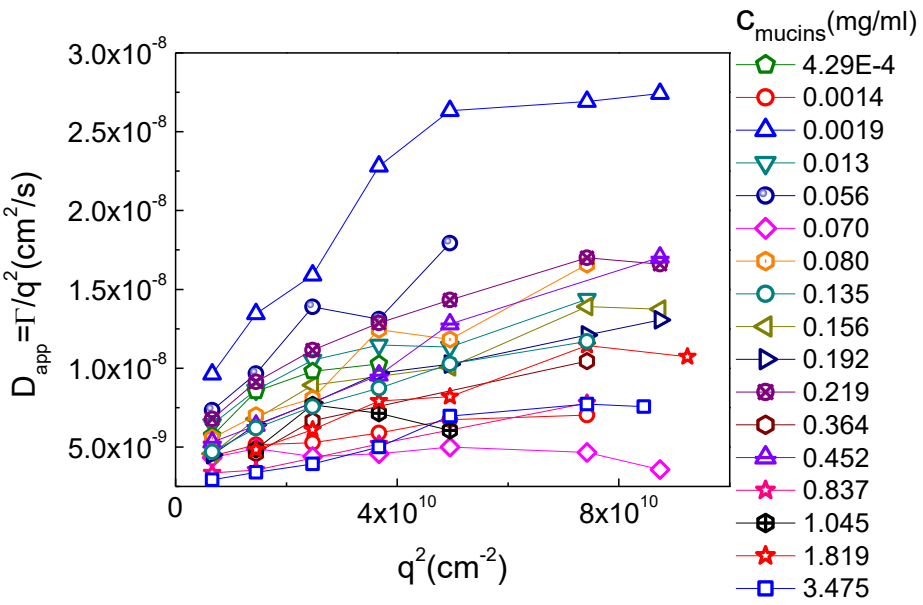

Figure 8. Apparent diffusion coefficient (Γ/q^2) against q^2 for all measured mucin concentrations. All data exhibit a dependence of q^2, conforming to large sizes and possible aggregates

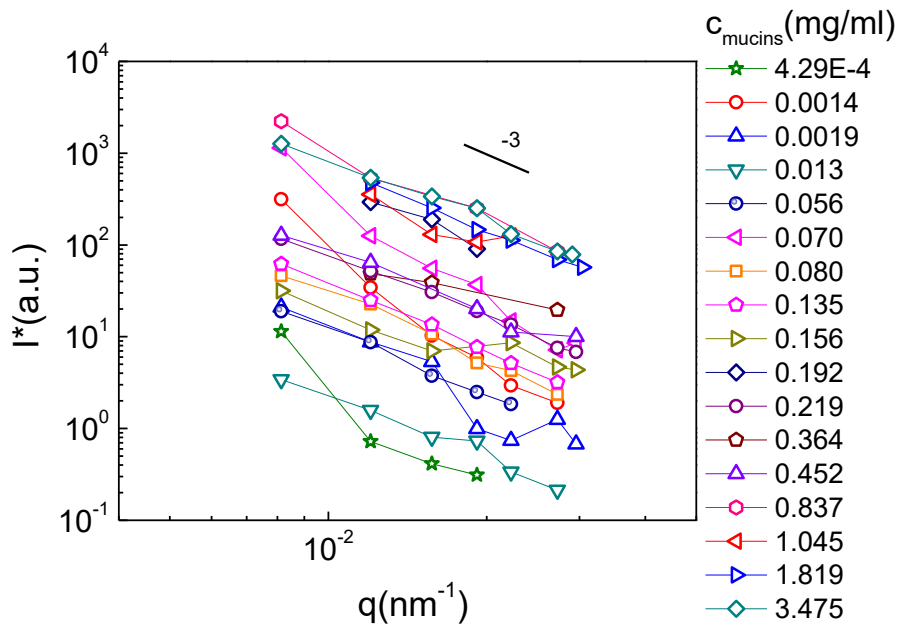

Figure 9. Total scattering dynamic intensity (I) against scattering wavevector (q) for all measured mucin concentrations. The slope of -3 indicates the topology (fractal dimension) of the measured object*

Literature

[1] D. Vlassopoulos and G. Fytas, “From Polymers to Colloids: Engineering the Dynamic Properties of Hairy Particles,” in *High Solid Dispersions*, vol. 236, M. Cloitre, Ed. Berlin, Heidelberg: Springer Berlin Heidelberg, 2009, pp. 1–54.

[2] J. Mewis and N. J. Wagner, *Colloidal suspension rheology*. Cambridge ; New York: Cambridge University Press, 2012.

[3] D. Vlassopoulos and M. Cloitre, “Tunable rheology of dense soft deformable colloids,” *Current Opinion in Colloid and Interface Science*, vol. 19, no. 6, pp. 561–574, 2014.

[4] N. Koumakis, A. Pamvouxoglou, A. S. Poulos, and G. Petekidis, “Direct comparison of the rheology of model hard and soft particle glasses,” *Soft Matter*, vol. 8, no. 15, p. 4271, 2012.

[5] L. A. Lyon and A. Fernandez-Nieves, “The Polymer/Colloid Duality of Microgel Suspensions,” *Annual Review of Physical Chemistry*, vol. 63, no. 1, pp. 25–43, 2012.

[6] H. Senff and W. Richtering, “Temperature sensitive microgel suspensions: Colloidal phase behavior and rheology of soft spheres,” *Journal of Chemical Physics*, vol. 111, no. 4, pp. 1705–1711, 1999.

[7] H. M. Shewan and J. R. Stokes, “Viscosity of soft spherical micro-hydrogel suspensions,” *Journal of Colloid and Interface Science*, vol. 442, pp. 75–81, 2015.

[8] V. Carrier and G. Petekidis, “Nonlinear rheology of colloidal glasses of soft thermosensitive microgel particles,” *Journal of Rheology*, vol. 53, no. 2, pp. 245–273, 2009.

[9] C. Pellet and M. Cloitre, “The glass and jamming transitions of soft polyelectrolyte microgel suspensions,” *Soft Matter*, vol. 12, no. 16, pp. 3710–3720, 2016.

[10] B. Demouveaux, V. Gouyer, F. Gottrand, T. Narita, and J.-L. Desseyn, “Gel-forming mucin interactome drives mucus viscoelasticity,” *Advances in Colloid and Interface Science*, vol. 252, pp. 69–82, Feb. 2018.

[11] L. Böni, P. Fischer, L. Böcker, S. Kuster, and P. A. Rühs, “Hagfish slime and mucin flow properties and their implications for defense,” *Scientific Reports*, vol. 6, no. 1, Sep. 2016.

[12] L. J. Böni *et al.*, “Effect of ionic strength and seawater cations on hagfish slime formation,” *Scientific Reports*, vol. 8, no. 1, Dec. 2018.

[13] D. S. Fudge, “Composition, morphology and mechanics of hagfish slime,” *Journal of Experimental Biology*, vol. 208, no. 24, pp. 4613–4625, Dec. 2005.

[14] A.-M. Philippe, L. Cipelletti, and D. Larobina, “Mucus as an Arrested Phase Separation Gel,” *Macromolecules*, vol. 50, no. 20, pp. 8221–8230, Oct. 2017.

[15] G. Chaudhary, D. S. Fudge, B. Macias-Rodriguez, and R. H. Ewoldt, “Concentration-independent mechanics and structure of hagfish slime,” *Acta Biomaterialia*, vol. 79, pp. 123–134, Oct. 2018.

[16] D. Vlassopoulos and M. Cloitre, “Tunable rheology of dense soft deformable colloids,” *Current Opinion in Colloid & Interface Science*, vol. 19, no. 6, pp. 561–574, Dec. 2014.

[17] M. Antonietti, “Microgels-Polymers with a Special Molecular Architecture,” *Angewandte Chemie International Edition in English*, vol. 27, no. 12, pp. 1743–1747, Dec. 1988.

[18] M. Cloitre, R. Borrega, F. Monti, and L. Leibler, “Structure and flow of polyelectrolyte microgels: from suspensions to glasses,” *Comptes Rendus Physique*, vol. 4, no. 2, pp. 221–230, Mar. 2003.

[19] L. Mohan, R. T. Bonnecaze, and M. Cloitre, “Microscopic Origin of Internal Stresses in Jammed Soft Particle Suspensions,” *Physical Review Letters*, vol. 111, no. 26, Dec. 2013.

[20] A. Fernández-Nieves, A. Fernández-Barbero, B. Vincent, and F. J. de las Nieves, “Charge Controlled Swelling of Microgel Particles,” *Macromolecules*, vol. 33, no. 6, pp. 2114–2118, Mar. 2000.

[21] C. Pellet and M. Cloitre, “The glass and jamming transitions of soft polyelectrolyte microgel suspensions,” *Soft Matter*, vol. 12, no. 16, pp. 3710–3720, 2016.

[22] E. Di Cola, A. Moussaïd, M. Sztucki, T. Narayanan, and E. Zaccarelli, “Correlation between structure and rheology of a model colloidal glass,” *The Journal of Chemical Physics*, vol. 131, no. 14, p. 144903, Oct. 2009.

[23] E. Zaccarelli and W. C. K. Poon, “Colloidal glasses and gels: The interplay of bonding and caging,” *Proceedings of the National Academy of Sciences*, vol. 106, no. 36, pp. 15203–15208, Sep. 2009.

[24] C. Christopoulou, G. Petekidis, B. Erwin, M. Cloitre, and D. Vlassopoulos, “Ageing and yield behaviour in model soft colloidal glasses,” *Philosophical Transactions of the Royal Society A: Mathematical, Physical and Engineering Sciences*, vol. 367, no. 1909, pp. 5051–5071, Dec. 2009.

[25] L. A. Lyon and A. Fernandez-Nieves, “The Polymer/Colloid Duality of Microgel Suspensions,” *Annual Review of Physical Chemistry*, vol. 63, no. 1, pp. 25–43, May 2012.

[26] A. Gandhi, A. Paul, S. O. Sen, and K. K. Sen, “Studies on thermoresponsive polymers: Phase behaviour, drug delivery and biomedical applications,” *Asian Journal of Pharmaceutical Sciences*, vol. 10, no. 2, pp. 99–107, Apr. 2015.

[27] H. Senff and W. Richtering, “Temperature sensitive microgel suspensions: Colloidal phase behavior and rheology of soft spheres,” *The Journal of Chemical Physics*, vol. 111, no. 4, pp. 1705–1711, Jul. 1999.

[28] Z. Dai and T. Ngai, “Microgel particles: The structure-property relationships and their biomedical applications,” *Journal of Polymer Science Part A: Polymer Chemistry*, vol. 51, no. 14, pp. 2995–3003, Jul. 2013.

[29] R. H. Colby, “Structure and linear viscoelasticity of flexible polymer solutions: comparison of polyelectrolyte and neutral polymer solutions,” *Rheologica Acta*, vol. 49, no. 5, pp. 425–442, May 2010.

[30] M. Muthukumar, “50th Anniversary Perspective : A Perspective on Polyelectrolyte Solutions,” *Macromolecules*, vol. 50, no. 24, pp. 9528–9560, Dec. 2017.

[31] A. V. Dobrynin, R. H. Colby, and M. Rubinstein, “Scaling Theory of Polyelectrolyte Solutions,” *Macromolecules*, vol. 28, no. 6, pp. 1859–1871, Nov. 1995.

[32] M. Sedlák and E. J. Amis, “Concentration and molecular weight regime diagram of salt-free polyelectrolyte solutions as studied by light scattering,” *The Journal of Chemical Physics*, vol. 96, no. 1, pp. 826–834, Jan. 1992.

[33] A. Dobrynin and M. Rubinstein, “Theory of polyelectrolytes in solutions and at surfaces,” *Progress in Polymer Science*, vol. 30, no. 11, pp. 1049–1118, Nov. 2005.

[34] P. M. Visakh, “Polyelectrolyte: Thermodynamics and Rheology,” in *Polyelectrolytes*, V. P. M., O. Bayraktar, and G. A. Picó, Eds. Cham: Springer International Publishing, 2014, pp. 1–17.

[35] S. K. Lai, Y.-Y. Wang, D. Wirtz, and J. Hanes, “Micro- and macrorheology of mucus,” *Advanced Drug Delivery Reviews*, vol. 61, no. 2, pp. 86–100, Feb. 2009.

[36] X. Wang, H. Su, W. Lv, M. Du, Y. Song, and Q. Zheng, “Complex rheological behaviors of loach (*Misgurnus anguillicaudatus*) skin mucus,” *Journal of Rheology*, vol. 59, no. 1, pp. 51–62, Jan. 2015.

[37] R. H. Ewoldt, C. Clasen, A. E. Hosoi, and G. H. McKinley, “Rheological fingerprinting of gastropod pedal mucus and synthetic complex fluids for biomimicking adhesive locomotion,” *Soft Matter*, vol. 3, no. 5, p. 634, 2007.

[38] J. P. Celli *et al.*, “Rheology of Gastric Mucin Exhibits a pH-Dependent Sol−Gel Transition,” *Biomacromolecules*, vol. 8, no. 5, pp. 1580–1586, May 2007.

[39] C. E. Wagner, B. S. Turner, M. Rubinstein, G. H. McKinley, and K. Ribbeck, “A Rheological Study of the Association and Dynamics of MUC5AC Gels,” *Biomacromolecules*, vol. 18, no. 11, pp. 3654–3664, Nov. 2017.

[40] T. A. Waigh *et al.*, “Entanglement Coupling in Porcine Stomach Mucin,” *Langmuir*, vol. 18, no. 19, pp. 7188–7195, Sep. 2002.

[41] E. S. Vasquez, J. Bowser, C. Swiderski, K. B. Walters, and S. Kundu, “Rheological characterization of mammalian lung mucus,” *RSC Adv.*, vol. 4, no. 66, pp. 34780–34783, 2014.

[42] V. Zintzen, C. D. Roberts, M. J. Anderson, A. L. Stewart, C. D. Struthers, and E. S. Harvey, “Hagfish predatory behaviour and slime defence mechanism,” *Scientific Reports*, vol. 1, no. 1, Dec. 2011.

[43] J. E. Herr, A. M. Clifford, G. G. Goss, and D. S. Fudge, “Defensive slime formation in Pacific hagfish requires Ca2+- and aquaporin-mediated swelling of released mucin vesicles,” *Journal of Experimental Biology*, vol. 217, no. 13, pp. 2288–2296, Jul. 2014.

[44] D. S. Fudge, “The biomechanics of intermediate filament-based materials:insights from hagfish slime threads,” 2002.

[45] R. H. Ewoldt, T. M. Winegard, and D. S. Fudge, “Non-linear viscoelasticity of hagfish slime,” *International Journal of Non-Linear Mechanics*, vol. 46, no. 4, pp. 627–636, May 2011.

[46] W. Brown, Ed., *Dynamic light scattering: the method and some applications*. Oxford [England] : New York: Clarendon Press ; Oxford University Press, 1993.

[47] B. J. Berne and R. Pecora, *Dynamic light scattering: with applications to chemistry, biology, and physics*, Dover ed. Mineola, N.Y: Dover Publications, 2000.

[48] J. Stetefeld, S. A. McKenna, and T. R. Patel, “Dynamic light scattering: a practical guide and applications in biomedical sciences,” *Biophysical Reviews*, vol. 8, no. 4, pp. 409–427, Dec. 2016.

[49] K. Fischer and M. Schmidt, “Pitfalls and novel applications of particle sizing by dynamic light scattering,” *Biomaterials*, vol. 98, pp. 79–91, Aug. 2016.

[50] *Light Scattering from Polymer Solutions and Nanoparticle Dispersions*. Berlin, Heidelberg: Springer Berlin Heidelberg, 2007.

[51] M. Rubinstein and R. H. Colby, *Polymer physics*. Oxford ; New York: Oxford University Press, 2003.

[52] B. Chu, *Laser Light Scattering 2e: Basic Principles and Practice.* Oxford: Elsevier Science, 1991.

[53] H. A. Barnes, J. F. Hutton, and K. Walters, *An introduction to rheology*. Amsterdam ; New York: Elsevier : Distributors for the U.S. and Canada, Elsevier Science Pub. Co, 1989.

[54] “Kinexus rheometer and rSpace software, user manual.” 2009.

[55] S. Costanzo, G. Ianniruberto, G. Marrucci, and D. Vlassopoulos, “Measuring and assessing first and second normal stress differences of polymeric fluids with a modular cone-partitioned plate geometry,” *Rheologica Acta*, vol. 57, no. 5, pp. 363–376, May 2018.

[56] C. W. Macosko, *Rheology: principles, measurements, and applications*. New York: VCH, 1994.

[57] G. H. McKinley and T. Sridhar, “Filament-stretching rheometry of complex fluids,” *Annual Review of Fluid Mechanics*, vol. 34, no. 1, pp. 375–415, Jan. 2002.

[58] L. E. Rodd, T. P. Scott, J. J. Cooper-White, and G. H. McKinley, “Capillary Break-up Rheometry of Low-Viscosity Elastic Fluids,” vol. 15, no. 1, p. 16, 2004.

[59] E. Miller, C. Clasen, and J. P. Rothstein, “The effect of step-stretch parameters on capillary breakup extensional rheology (CaBER) measurements,” *Rheologica Acta*, vol. 48, no. 6, pp. 625–639, Jul. 2009.

[60] O. Arnolds, H. Buggisch, D. Sachsenheimer, and N. Willenbacher, “Capillary breakup extensional rheometry (CaBER) on semi-dilute and concentrated polyethyleneoxide (PEO) solutions,” *Rheologica Acta*, vol. 49, no. 11–12, pp. 1207–1217, Dec. 2010.

[61] C. Clasen, J. Eggers, M. A. Fontelos, J. Li, and G. H. McKINLEY, “The beads-on-string structure of viscoelastic threads,” *Journal of Fluid Mechanics*, vol. 556, p. 283, Jun. 2006.

[62] P. C. Sousa, E. J. Vega, R. G. Sousa, J. M. Montanero, and M. A. Alves, “Measurement of relaxation times in extensional flow of weakly viscoelastic polymer solutions,” *Rheologica Acta*, vol. 56, no. 1, pp. 11–20, Jan. 2017.

[63] M. S. N. Oliveira and G. H. McKinley, “Iterated stretching and multiple beads-on-a-string phenomena in dilute solutions of highly extensible flexible polymers,” *Physics of Fluids*, vol. 17, no. 7, p. 071704, Jul. 2005.

[64] T. Owen, “Principles and applications of UV-visible spectroscopy,” *Fundamentals of UV-visible spectroscopy*, p. 18, 1996.

[65] E. A. G. Zagatto, C. C. Oliveira, A. Townshend, and P. J. Worsfold, “Interaction of Radiation with the Flowing Sample,” in *Flow Analysis with Spectrophotometric and Luminometric Detection*, Elsevier, 2012, pp. 95–146.

[66] H. G. Schild, “Poly(N-isopropylacrylamide): experiment, theory and application,” *Progress in Polymer Science*, vol. 17, no. 2, pp. 163–249, Jan. 1992.

[67] M. Shibayama and T. Tanaka, “Volume phase transition and related phenomena of polymer gels,” in *Responsive Gels: Volume Transitions I*, vol. 109, K. Dušek, Ed. Berlin, Heidelberg: Springer Berlin Heidelberg, 1993, pp. 1–62.

[68] S. Kamble, “Probing Structure and Dynamics of Soft Colloidal Glasses using Rheology and Light Scattering,” p. 142, 2013.

[69] R. Zurflüh, “Isolation and characterization of hagfish mucin,” 2015.

[70] J. M. Jørgensen, J. P. Lomholt, R. E. Weber, and H. Malte, *The Biology of Hagfishes*. Dordrecht: Springer Netherlands, 1998.

[71] R. H. Spitzer and E. A. Koch, “Hagfish Skin and Slime Glands,” in *The Biology of Hagfishes*, Dordrecht: Springer Netherlands, 1998, pp. 109–132.

[72] S. W. Downing, W. L. Salo, R. H. Spitzer, and E. A. Koch, “The hagfish slime gland: a model system for studying the biology of mucus,” *Science*, vol. 214, no. 4525, pp. 1143–1145, Dec. 1981.

[73] J. E. Herr, T. M. Winegard, M. J. O'Donnell, P. H. Yancey, and D. S. Fudge, "Stabilization and swelling of hagfish slime mucin vesicles," *Journal of Experimental Biology*, vol. 213, no. 7, pp. 1092–1099, Apr. 2010.

[74] W. L. Salo, S. W. Downing, W. A. Lidinsky, W. H. Gallagher, R. H. Spitzer, and E. A. Koch, "Fractionation of Hagfish Slime Gland Secretions: Partial Characterization of the Mucous Vesicle Fraction," *Preparative Biochemistry*, vol. 13, no. 2, pp. 103–135, Jul. 1983.

[75] R. Bansil, E. Stanley, and J. T. Lamont, "Mucin Biophysics," *Annual Review of Physiology*, vol. 57, no. 1, pp. 635–657, Oct. 1995.

[76] G. J. Strous and J. Dekker, "Mucin-Type Glycoproteins," *Critical Reviews in Biochemistry and Molecular Biology*, vol. 27, no. 1–2, pp. 57–92, Jan. 1992.

[77] R. Bansil and B. S. Turner, "Mucin structure, aggregation, physiological functions and biomedical applications," *Current Opinion in Colloid & Interface Science*, vol. 11, no. 2–3, pp. 164–170, Jun. 2006.

[78] R. Bansil, J. P. Celli, J. M. Hardcastle, and B. S. Turner, "The Influence of Mucus Microstructure and Rheology in Helicobacter pylori Infection," *Frontiers in Immunology*, vol. 4, 2013.

[79] L. J. Böni *et al.*, "Hagfish slime exudate stabilization and its effect on slime formation and functionality," *Biology Open*, vol. 6, no. 7, pp. 1115–1122, Jul. 2017.

[80] L. Böcker, P. A. Rühs, L. Böni, P. Fischer, and S. Kuster, "Fiber-Enforced Hydrogels: Hagfish Slime Stabilized with Biopolymers including κ-Carrageenan," *ACS Biomaterials Science & Engineering*, vol. 2, no. 1, pp. 90–95, Jan. 2016.

[81] L. Böni, P. A. Rühs, E. J. Windhab, P. Fischer, and S. Kuster, "Gelation of Soy Milk with Hagfish Exudate Creates a Flocculated and Fibrous Emulsion- and Particle Gel," *PLOS ONE*, vol. 11, no. 1, p. e0147022, Jan. 2016.

[82] P. N. Pusey and W. van Megen, "Phase behaviour of concentrated suspensions of nearly hard colloidal spheres," *Nature*, vol. 320, p. 340, Mar. 1986.

[83] G. Petekidis, D. Vlassopoulos, and P. N. Pusey, "Yielding and flow of sheared colloidal glasses," *Journal of Physics: Condensed Matter*, vol. 16, no. 38, pp. S3955–S3963, Sep. 2004.

[84] A. Ikeda, L. Berthier, and P. Sollich, "Disentangling glass and jamming physics in the rheology of soft materials," *Soft Matter*, vol. 9, no. 32, p. 7669, 2013.

[85] K. N. Nordstrom *et al.*, "Microfluidic Rheology of Soft Colloids above and below Jamming," *Physical Review Letters*, vol. 105, no. 17, Oct. 2010.

[86] S. W. Provencher, "A constrained regularization method for inverting data represented by linear algebraic or integral equations," *Computer Physics Communications*, vol. 27, no. 3, pp. 213–227, Sep. 1982.

[87] D. E. Koppel, "Analysis of Macromolecular Polydispersity in Intensity Correlation Spectroscopy: The Method of Cumulants," *The Journal of Chemical Physics*, vol. 57, no. 11, pp. 4814–4820, Dec. 1972.

[88] A. G. Mailer, P. S. Clegg, and P. N. Pusey, “Particle sizing by dynamic light scattering: non-linear cumulant analysis,” *Journal of Physics: Condensed Matter*, vol. 27, no. 14, p. 145102, Apr. 2015.

[89] A. Scotti *et al.*, “The CONTIN algorithm and its application to determine the size distribution of microgel suspensions,” *The Journal of Chemical Physics*, vol. 142, no. 23, p. 234905, Jun. 2015.

[90] L. Cipelletti and L. Ramos, “Slow dynamics in glassy soft matter,” *Journal of Physics: Condensed Matter*, vol. 17, no. 6, pp. R253–R285, Feb. 2005.

[91] P. Debye, H. R. Anderson, and H. Brumberger, “Scattering by an Inhomogeneous Solid. II. The Correlation Function and Its Application,” *Journal of Applied Physics*, vol. 28, no. 6, pp. 679–683, Jun. 1957.

[92] D. R. Kester, I. W. Duedall, D. N. Connors, and R. M. Pytkowicz, “Preparation of artificial seawater,” *Limnology and Oceanography*, vol. 12, no. 1, pp. 176–179, Apr. 1967.

[93] “Instruction Manual, HAAKE CaBER 1.” Thermo Scientific.

[94] M. Rubinstein, R. H. Colby, A. V. Dobrynin, and J.-F. Joanny, “Elastic Modulus and Equilibrium Swelling of Polyelectrolyte Gels,” *Macromolecules*, vol. 29, no. 1, pp. 398–406, Jan. 1996.

[95] F. R. Schwarzl, “The numerical calculation of storage and loss compliance from creep data for linear viscoelastic materials,” *Rheologica Acta*, vol. 8, no. 1, pp. 6–17, Mar. 1969.

[96] J. Weese, “A regularization method for nonlinear ill-posed problems,” *Computer Physics Communications*, vol. 77, no. 3, pp. 429–440, Nov. 1993.

[97] M. A. Rao, “Flow and Functional Models for Rheological Properties of Fluid Foods,” in *Rheology of Fluid, Semisolid, and Solid Foods*, Boston, MA: Springer US, 2014, pp. 27–61.

[98] D. S. Fudge, T. Winegard, R. H. Ewoldt, D. Beriault, L. Szewciw, and G. H. McKinley, “From ultra-soft slime to hard -keratins: The many lives of intermediate filaments,” *Integrative and Comparative Biology*, vol. 49, no. 1, pp. 32–39, Jul. 2009.